ENHANCED ELECTROCHEMICAL CHARACTERISTICS OF LITHIUM MANGANESE OXIDE THIN FILM CATHODES FOR LI-ION RECHARGEABLE MICROBATTERIES

By

WON-SEOK KIM

A DISSERTATION PRESENTED TO THE GRADUATE SCHOOL
OF THE UNIVERSITY OF FLORIDA IN PARTIAL FULFILLMENT
OF THE REQUIREMENTS FOR THE DEGREE OF
DOCTOR OF PHILOSOPHY

UNIVERSITY OF FLORIDA

2004

Copyright 2004

by

WON-SEOK KIM

This dissertation is dedicated to my family especially my parents and wife.

ACKNOWLEDGMENTS

I would like to thank my advisor, Dr. Rajiv K. Singh, for his countless advice and support for the last five years. I also wish to thank Dr. Cammy Abernathy, Dr. David Norton, Dr. Stephen Pearton, and Dr. Dinesh Shah for serving as the members of my supervisory committee as well as for their warm guidance through discussion of this work.

I specially want to thank Dr. Deepika Singh for her help with the electrochemical measurement and discussion. I also thank staff members at MAIC and ERC for allowing me to use their facilities for my work. I specially want to thank Margaret for taking care of me like her son.

My thanks are extended to my friends and coworkers : Kyo-Gong, Kyo-Se, Jaeyoung, Wonseop, Seung-Mahn, Joodong, Hyucksoo, Hanho, Sanghyun, Su-Ho, Junyoung, Jinho, Jeong-Min, Seungwoo, Yiyeon, Sangyup, Jeenki, Cheolhang, Kilseok, Mike, Babil, Josh, Frank, Chad, Srini, Jeremiah, Vishal, Kathick, and others who gave me warm friendship and support.

TABLE OF CONTENTS

Page

ACKNOWLEDGMENTS iv

LIST OF TABLES viii

LIST OF FIGURES ix

ABSTRACT xv

CHAPTER

1 INTRODUCTION 1

2 LITERATURE REVIEW 4

- Electrochemical Cell (Battery) 4
  - Fundamentals of Batteries 4
  - Li-ion Batteries 9
  - Lithium Manganese Oxide ($LiMn_2O_4$) 12
    - Capacity Fade and Rate Capability 13
    - Thin-film Lithium Manganese Oxide ($LiMn_2O_4$) 21
    - Oxygen-rich Spinel ($Li_{1-\delta}Mn_{2-2\delta}O_4$) 24
    - Aluminum-doped Spinel ($LiAl_xMn_{2-x}O_4$) 27
- Synthesis and Characterization of Thin Film Cathode 29
  - Pulsed Laser Deposition (PLD) 29
    - Principle of excimer lasers 29
    - Basics of PLD 30
    - Ultraviolet-assisted PLD (UVPLD) 32
  - Electrochemical Characterizations 33
    - Cyclic voltammetry (CV) 33
    - Chronopotentiometry 35
    - Alternative current impedance (ACI) 36

3 EXPERIMENTAL PROCEDURE 52

- Synthesis of Thin Film Cathodes 52
  - Target Preparation 52
  - Thin Film Deposition Process 53
- Characterizations of Thin Film Cathodes 54

X-ray Diffraction (XRD) 54
Scanning Electron Microscopy (SEM) 54
X-ray Photoelectron Spectroscopy (XPS) 54
Transmission Electron Microscopy (TEM) 55
Electrochemical Measurements 55

4 EFFECT OF TEMPERATURE ON THE ELECTROCHEMICAL CHARACTERISTICS OF LITHIUM MANGANESE OXIDE THIN FILM CATHODES 60

Introduction 60
Experimental 60
Results and Discussion 62
    Structural Characterizations 62
    Electrochemical Characteristics 65
        Cyclic voltammetry of 2.5 ~ 3.5 V region 65
        Discharge capacity of 2.5 ~ 3.5 V region 69
        Cycling behavior of 2.5 ~ 3.5 V region 71
        AC impedance of 2.5 ~ 3.5 V region 75
        Rate capability of 2.5 ~ 3.5 V region 77
        Cyclic voltammetry of 2.5 ~ 4.5 V region 79
        Cycling behavior of 2.5 ~ 4.5 V region 79
Summary 80

5 EFFECT OF ALUMINUM DOPING ON THE ELECTROCHEMICAL CHARACTERISTICS OF LITHIUM MANGANESE OXIDE THIN FILM CATHODES 101

Introduction 101
Experimental 102
Results and Discussions 102
    Structural Characterizations 102
    Electrochemical Characteristics 105
        Cyclic voltammetry of 2.5 ~ 3.5 V region 105
        Discharge capacity of 2.5 ~ 3.5 V region 105
        Cycling behavior of 2.5 ~ 3.5 V region 106
        AC impedance of 2.5 ~ 3.5 V region 108
        Rate capability of 2.5 ~ 3.5 V region 110
        Cyclic voltammetry of 2.5 ~ 4.5 V region 111
        Discharge capacity and cycling behavior of 2.5 ~ 4.5 V region 112
Summary 115

6 EFFECT OF ULTAR-VIOLET RADIATION ON THE ELECTROCHEMICAL CHARACTERISTICS OF LITHIUM MANGANESE OXIDE THIN FILM CATHODES 133

Introduction 133
Experimental 135
Results and Discussions 135
  Structural Characterizations 135
  Electrochemical Characteristics 138
    Electrochemical behavior of oxygen-rich spinel cathode of 2.5 ~ 3.5 V region 138
    Cyclic voltammetry and discharge capacity of 2.5 ~ 3.5 V region 141
    Cycling behavior of 2.5 ~ 3.5 V region 142
    AC impedance of 2.5 ~ 3.5 V region 144
    Rate capability of 2.5 ~ 3.5 V region 147
    Cyclic voltammetry of 2.5 ~ 4.5 V region 149
    Discharge capacity and cycling behavior of 2.5 ~ 4.5 V region 149
Summary 152

7 CONCLUSIONS 172

APPENDIX FITTING OF THE AC IMPEDANCE 176

LIST OF REFERENCES 189

BIOGRAPHICAL SKETCH 197

LIST OF TABLES

Table page

2-1. Cost, reserves, and environmental limit of transition metals. 12

2-2. Primary reaction channels for KrF excimer. An asterisk(*) represents an electronically excited state of the species. 30

4-1. Parameters measured from the cyclic voltammograms. 69

4-2. Parameters calculated from the AC impedance spectra. 77

5-1. Parameters calculated from the AC impedance spectra of $LiAl_xMn_{2-x}O_4$ thin films grown by PLD. 109

6-1. Parameters calculated from the AC impedance spectra of $LiAl_xMn_{2-x}O_{4+\delta}$ thin films grown by UVPLD. 145

LIST OF FIGURES

Figure page

2-1. Electrochemical operation of a cell: (a) Discharge and (b) Charge. 38

2-2. Schematic of the electrochemical process in a Li-ion battery. 39

2-3. Schematic of a unit cell structure of the spinel $LiMn_2O_4$. 40

2-4. Variation of voltage as a function of x in $Li_{1+x}Mn_2O_4$ and $Li_{1-x}Mn_2O_4$ in $Li/LiMn_2O_4$ cell. 41

2-5. Jahn-Teller distortion of the d^4 electron configuration for $LiMn_2O_4$. 42

2-6. Schematic cross section of a thin film Li-ion battery. 43

2-7. Li-Mn-O spinel phase diagram. 44

2-8. Three-dimensional diagram of capacity-rechargeability-chemical composition for each compound on the $LiMn_2O_4$-$Li_4Mn_5O_{12}$-$Li_2Mn_4O_9$ plane................................45

2-9. Electronic states in excimer emission. 46

2-10. XPS high resolution of O 1s region acquired from Y_2O_3 thin film: (a) UVPLD and (b) PLD at different temperature. 47

2-11. Cyclic voltammograms of (a) reversible process, (b) irreversible process, and (c) quasi-reversible process. 48

2-12. Constant current chronopotentiometry. 49

2-13. Equivalent electrical circuit of an electrochemical cell for a simple electrode process. 50

2-14. A typical Nyquist plot of a simple electrochemical process. 51

3-1. Schematic of UVPLD system. 58

3-2. Schematic of the electrochemical cell used. 59

4-1. XRD of $LiMn_2O_4$ thin films grown in 500 mtorr of O_2 at (a) 700˚C, (b) 500˚C, and (c) 300˚C. 83

4-2. Lattice constant (left) and FWHM of (111) peak (right) of $LiMn_2O_4$ thin films grown in 500 mtorr of O_2 as a function of substrate temperature. 83

4-3. SEM micrographs of $LiMn_2O_4$ thin films grown in 500 mtorr of O_2 at (a) 400°C, (b) 500°C, and (c) 700°C. 84

4-4. TEM of $LiMn_2O_4$ thin films grown in 500 mtorr of O_2 at 500°C: (a) Bright field image with selected area electron diffraction (SAD) and (b) Energy dispersive X-ray spectroscopy (EDX). 85

4-5. XPS survey scan of $LiMn_2O_4$ thin film grown in 500 mtorr of O_2 at 300°C. 86

4-6. High resolution XPS of Mn $2p_{3/2}$ of $LiMn_2O_4$ thin films grown in 500 mtorr of O_2 at (a) 300°C, (b) 500°C, and (c) 700°C. 87

4-7. Cyclic voltammograms in the range of 2.5 ~ 3.5 V of a $LiMn_2O_4$ thin film grown at 300°C: (a) Normal cyclic voltammograms and (b) Psudocapacitances at different sweep rates. 88

4-8. Cyclic voltammograms in the range of 2.5 ~ 3.5 V of $LiMn_2O_4$ thin films grown at 300°C, 400°C, 500°C, 600°C, and 700°C. Sweep rate : 0.1 mV/s. 89

4-9. Diffusion coefficients of Li^+ in the $LiMn_2O_4$ thin film as a function of substrate temperature. 90

4-10. The first discharge curves in the range of 2.5 ~ 3.5 V of $LiMn_2O_4$ thin films grown at 300°C, 400°C, 500°C, 600°C, and 700°C. Discharge rate: 1 C rate. 91

4-11. Discharge curves in the range of 2.5 ~ 3.5 V of $LiMn_2O_4$ thin films grown at (a) 300°C, (b) 400°C and (c) 500°C. 92

4-11. Discharge curves in the range of 2.5 ~ 3.5 V of a $LiMn_2O_4$ thin film grown at (d) 600°C and (e) 700°C. 93

4-12. Discharge capacity as a function of cycle number in the range of 2.5 ~ 3.5 V of $LiMn_2O_4$ thin films grown at different temperatures: (a) Specific discharge capacity and (b) Relative discharge capacity. 94

4-13. AC impedance spectroscopy of $LiMn_2O_4$ thin films: (a) As-received $LiMn_2O_4$ thin films grown at different temperatures and (b) $LiMn_2O_4$ thin film grown at 300°C after cycling. 95

4-14. Equivalent circuit used for the fitting of the Nyquist plots. 96

4-15. Double layer capacitance and charge transfer resistance of $LiMn_2O_4$ thin films grown at different temperatures. 96

4-16. Discharge curves at different current densities of $LiMn_2O_4$ thin films grown at (a) 300°C, (b) 400°C, (c) 500, (d) 600°C, and (e) 700°C. 97

4-17. Discharge rate capability in the range of 2.5 ~ 3.5 V of $LiMn_2O_4$ thin films grown at different temperatures....98

4-18. Cyclic voltammograms in the range of 2.5 ~ 4.5 V of $LiMn_2O_4$ thin films grown at (a) 300°C and (b) 500°C. Sweep rate: 0.1 mV/s....99

4-19. Discharge curves in the range of 2.5 ~ 4.5 V of $LiMn_2O_4$ thin films grown (a) 300° C and (b) 500°C. Discharge rate : 60 μA/cm^2. 100

5-1. XRD of $LiAl_xMn_{2-x}O_4$ targets: (a) x = 0.1, (b) x = 0.2, and (c) x = 0.3. 117

5-2. XRD of $LiAl_xMn_{2-x}O_4$ thin films grown in 500 mtorr of O_2 at 500°C: (a) x = 0.1, (b) x = 0.2, and (c) x = 0.3. 118

5-3. Lattice constants of $LiAlxMn_{2-x}O_4$ targets and thin films grown in 500 mtorr of O_2 at 500°C. 118

5-4. SEM micrographs of (a) $LiAl_{0.1}Mn_{1.9}O_4$ and (b) $LiAl_{0.2}Mn_{1.8}O_4$ thin films grown in 500 mtorr of O_2 at 500°C....119

5-5. XPS survey scan of $LiAl_{0.3}Mn_{1.7}O_4$ thin film grown in 500 mtorr of O_2 at 500°C. .120

5-6. O 1s spectra of $LiAl_xMn_{2-x}O_4$ thin film grown in 500 mtorr of O_2 at 500°C: (a) x = 0.1, (b) x = 0.2, and (c) x = 0.3....121

5-7. Cyclic voltammograms in the range of 2.5 ~ 3.5 V of $LiAl_xMn_{2-x}O_4$ thin films grown in 500 mtorr of O_2 at 500°C....122

5-8. The first discharge curves in the range of 2.5 ~ 3.5 V of $LiAl_xMn_{2-x}O_4$ thin films grown in 500 mtorr of O_2 at 500°C. 123

5-9. Discharge curves in the range of 2.5 ~ 3.5 V of (a) $LiAl_{0.1}Mn_{1.9}O_4$, (b) $LiAl_{0.2}Mn_{1.8}O_4$, and (C) $LiAl_{0.3}Mn_{1.7}O_4$ thin films grown in 500 mtorr of O_2 at 500° C. 124

5-10. Discharge capacity in the range of 2.5 ~ 3.5 V of $LiAl_xMn_{2-x}O_4$ thin films grown in 500 mtorr of O_2 at 500°C: (a) Specific discharge capacity and (b) Relative discharge capacity. 125

5-11. AC impedance spectroscopies of $LiAl_xMn_{2-x}O_4$ thin films grown in 500 mtorr of O_2 at 500°C. 126

5-12. Discharge curves at different current densities of (a) $LiAl_{0.1}Mn_{1.9}O_4$, (b) $LiAl_{0.2}Mn_{1.8}O_4$, and (c) $LiAl_{0.3}Mn_{1.7}O_4$ thin films grown in 500 mtorr of O_2 at 500° C. 127

5-13. Discharge rate capability in the range of 2.5 ~ 3.5 V of $LiAl_xMn_{2-x}O_4$ thin films grown in 500 mtorr of O_2 at 500°C. 128

5-14. Cyclic voltammograms in the range of 2.5 ~ 4.5 V of $LiAl_xMn_{2-x}O_4$ thin films grown in 500 mtorr of O_2 at 500°C: (a) $x = 0.1$, (b) $x = 0.2$, and (c) $x = 0.3$. 129

5-15. The first discharge curves in the range of 2.5 ~ 4.5 V of $LiAl_xMn_{2-x}O_4$ thin films grown in 500 mtorr of O_2 at 500°C. Discharged at 1 C rate. 130

5-16. Discharge curves in the range of 2.5 ~ 4.5 V of (a) $LiAl_{0.1}Mn_{1.9}O_4$, (b) $LiAl_{0.2}Mn_{1.8}O_4$, and (C) $LiAl_{0.3}Mn_{1.7}O_4$ thin films grown in 500 mtorr of O_2 at 500° C. Discharged at 1 C rate. 131

5-17. Discharge capacity in the range of 2.5 ~ 4.5 V of $LiAl_xMn_{2-x}O_4$ thin films grown in 500 mtorr of O_2 at 500°C: (a) Specific discharge capacity and (b) Relative discharge capacity. 132

6-1. XRD of $LiMn_2O_4$ thin films grown in 500 mtorr of O_2 at 500°C by (a) UVPLD and (b) PLD. 154

6-2. XRD of $LiAl_{0.2}Mn_{1.8}O_4$ thin films grown in 500 mtorr of O_2 at 500°C by (a) UVPLD and (b) PLD. 155

6-3. Lattice constants of $LiAl_xMn_{2-x}O_4$ thin films grown in 500 mtorr of O_2 at 500°C by PLD and UVPLD. 155

6-4. SEM micrographs of (a) $LiMn_2O_4$, (b) $LiAl_{0.1}Mn_{1.9}O_4$ and (c) $LiAl_{0.3}Mn_{1.7}O_4$ thin films grown by UVPLD in 500 mtorr of O_2 at 500°C. 156

6-5. High resolution XPS of Mn $2p_{3/2}$ of thin films grown in 500 mtorr of O_2 at 500°C by UVPLD: (a) $LiMn_2O_4$, (b) $LiAl_{0.1}Mn_{1.9}O_4$, and (c) $LiAl_{0.3}Mn_{1.7}O_4$. 157

6-6. Cyclic voltammograms in the range of 2.5 ~ 3.5 V of $LiMn_2O_{4+\delta}$ thin film grown by UVPLD in 500 mtorr of O_2 at 400°C. 158

6-7. Discharge curves in the range of 2.5 ~ 3.5 V of $LiMn_2O_{4+\delta}$ thin film grown by UVPLD in 500 mtorr of O_2 at 400°C. 158

6-8. An isothermal cross section of the Li-Mn-O phase diagram at 20°C; Area I and II represent regions of defect spinel and defect rock salt phases, respectively. 159

6-9. Discharge curves at different current densities of $LiMn_2O_{4+\delta}$ thin films grown by UVPLD in 500 mtorr of O_2 at 400°C. 159

6-10. Cyclic voltammograms in the range of 2.5 ~ 3.5 V of $LiAl_xMn_{2-x}O_{4+\delta}$ (x = 0, 0.1, 0.2, 0.3) thin films grown by UVPLD in 500 mtorr of O_2 at 500°C. 160

6-11. The first discharge curves in the range of 2.5 ~ 3.5 V of $LiAl_xMn_{2-x}O_{4+\delta}$ thin films grown by UVPLD in 500 mtorr of O_2 at 500°C. 161

6-12. Discharge curves in the range of 2.5 ~ 3.5 V of $LiAl_xMn_{2-x}O_{4+\delta}$ thin films grown by UVPLD in 500 mtorr of O2 at 500°C: (a) x = 0, (b) x = 0.1, (c) x = 0.2, and (d) x = 0.3. 162

6-13. Discharge capacity in the range of 2.5 ~ 3.5 V of $LiAl_xMn_{2-x}O_{4+\delta}$ thin films grown by UVPLD in 500 mtorr of O_2 at 500°C: (a) Specific discharge capacity and (b) Relative discharge capacity. 163

6-14. AC impedance spectroscopies of $LiAl_xMn_{2-x}O_{4+\delta}$ thin films grown by UVPLD in 500 mtorr of O_2 at 500°C. 164

6-15. Diffusion coefficients of Li on discharge (left) and charge transfer resistances (right) as a function of x in $LiAl_xMn_{2-x}O_{4+\delta}$ thin films grown by UVPLD in 500 mtorr of O_2 at 500°C. 165

6-16. Discharge curves at different current densities of $LiAl_xMn_{2-x}O_{4+\delta}$ thin films grown by UVPLD in 500 mtorr of O_2 at 500°C: (a) x = 0, (b) x = 0.1, (c) x = 0.2, and (d) x = 0.3. 166

6-17. Discharge rate capability in the range of 2.5 ~ 3.5 V of $LiAl_xMn_{2-x}O_{4+\delta}$ thin films grown by UVPLD in 500 mtorr of O_2 at 500°C. 167

6-18. Cyclic voltammograms in the range of 2.5 ~ 4.5 V of $LiAl_xMn_{2-x}O_{4+\delta}$ thin films grown by UVPLD in 500 mtorr of O_2 at 500°C: (a) x = 0, (b) x = 0.2, and (c) x = 0.3. 168

6-19. The first discharge curves in the range of 2.5 ~ 4.5 V of $LiAl_xMn_{2-x}O_{4+\delta}$ thin films grown by UVPLD in 500 mtorr of O_2 at 500°C. 169

6-20. Discharge curves in the range of 2.5 ~ 4.5 V of (a) $LiMn_2O_{4+\delta}$, (b) $LiAl_{0.1}Mn_{1.9}O_{4+\delta}$, (c) $LiAl_{0.2}Mn_{1.8}O_{4+\delta}$, and (d) $LiAl_{0.3}Mn_{1.7}O_{4+\delta}$ thin films grown by UVPLD in 500 mtorr of O_2 at 500°C. Discharged at 1 C rate. 170

6-21. Discharge capacity in the range of 2.5 ~ 4.5 V of $LiAl_xMn_{2-x}O_{4+\delta}$ thin films grown by UVPLD in 500 mtorr of O_2 at 500°C: (a) Specific discharge capacity and (b) Relative discharge capacity. 171

A-1. Fitting of AC Impedance of $LiMn_2O_4$ thin film grown at 300°C in the oxygen 500 mtorr. 177

A-2. Fitting of AC Impedance of $LiMn_2O_4$ thin film grown at 400°C in the oxygen 500 mtorr. 178

A-3. Fitting of AC Impedance of $LiMn_2O_4$ thin film grown at 500°C in the oxygen 500 mtorr. 179

A-4. Fitting of AC Impedance of $LiMn_2O_4$ thin film grown at 600°C in the oxygen 500 mtorr. 180

A-5. Fitting of AC Impedance of $LiMn_2O_4$ thin film grown at 700°C in the oxygen 500 mtorr. 181

A-6. Fitting of AC Impedance of $LiAl_{0.1}Mn_{1.9}O_4$ thin film grown at 500°C in the oxygen 500 mtorr. 182

A-7. Fitting of AC Impedance of $LiAl_{0.2}Mn_{1.8}O_4$ thin film grown at 500°C in the oxygen 500 mtorr. 183

A-8. Fitting of AC Impedance of $LiAl_{0.3}Mn_{1.7}O_4$ thin film grown at 500°C in the oxygen 500 mtorr. 184

A-9. Fitting of AC Impedance of $LiMn_2O_{4+\delta}$ thin film grown by UVPLD at 500°C in the oxygen 500 mtorr. 185

A-10. Fitting of AC Impedance of $LiAl_{0.1}Mn_{1.9}O_{4+\delta}$ thin film grown by UVPLD at 500°C in the oxygen 500 mtorr. 186

A-11. Fitting of AC Impedance of $LiAl_{0.2}Mn_{1.8}O_{4+\delta}$ thin film grown by UVPLD at 500°C in the oxygen 500 mtorr. 187

A-12. Fitting of AC Impedance of $LiAl_{0.3}Mn_{1.7}O_{4+\delta}$ thin film grown by UVPLD at 500°C in the oxygen 500 mtorr. 188

Abstract of Dissertation Presented to the Graduate School
of the University of Florida in Partial Fulfillment of the
Requirements for the Degree of Doctor of Philosophy

ENHANCED ELECTROCHEMICAL CHARACTERISTICS OF LITHIUM MANGANESE OXIDE THIN FILM CATHODE FOR LI-ION RECHARGEABLE MICROBATTERIES

By

Won-Seok Kim

August 2004

Chair: Rajiv K. Singh
Major Department: Materials Science and Engineering

Spinel $LiMn_2O_4$ (average oxidation state of Mn = 3.5) thin film has been introduced for a promising cathode of thin film lithium-ion microbatteries because of its advantages over other cathodes. Thus, many research groups have been investigating the thin film lithium manganese oxide cathode using several different techniques but only a few of them achieved acceptable electrochemical properties required for a thin film cathode for 4 V region. However, for 3 V application the wide applications of $LiMn_2O_4$ film as a cathode in rechargeable microbatteries have been restricted by electrochemically unfavorable facts such as capacity fade on cycling and poor rate capability at high rates. In this study, we examined the mechanisms responsible for capacity fade on cycling and rate capability of $LiMn_2O_4$ thin film cathodes with the help of pulsed laser deposition (PLD) technique.

In an attempt to address these issues, a three-part experimental procedure has been designed to look at the effect of structure and compositions of the thin film cathodes on their electrochemical characteristics. First, the effect of growth temperature of the thin film cathodes has been investigated. Next, $LiMn_2O_4$ thin film cathodes doped with aluminum, which replaces Mn^{3+} in the spinel structure, have been synthesized and characterized as a function of the amount of aluminum substituted. Finally, ultraviolet radiation was added to a PLD system for *in situ* ultraviolet-assisted PLD (UVPLD) growth of cathode films. Through the addition of ultraviolet radiation, highly reactive oxygen species are generated which alter the oxygenation conditions and dynamically alter the films properties such as crystallinity and composition.

A variety of characterization techniques indicate that $LiMn_2O_4$ thin film cathodes grown at 400 ~ 500°C exhibit the optimized electrochemical characteristics in terms of capacity, capacity retention, and rate capability. Al-doped $LiMn_2O_4$ thin films show a more stable structure, leading to higher capacity retention with some sacrifice of discharge capacity and rate capability. Oxygen-rich spinel ($LiMn_2O_{4+\delta}$, $\delta>0$) thin film cathodes produced by UVPLD result in very high capacity and better rechargeability but lower rate capability.

CHAPTER 1
INTRODUCTION

The Li-ion battery market has grown in a decade and its value was estimated to be \$1.86 billion in 2000. Due to the expectation of growth to over 1.1 billion units with value of over \$4 billion by 2005, market interest in this cost-effective, high performance and safe technology has driven spectacular development [Ehr02]. This technology has rapidly become the standard power source in a broad array of markets, and battery performance continues to improve as Li-ion batteries are applied to an increasingly diverse range of applications. The capability of miniaturization and the reduction in scale and power requirements of electronic devices prompted work on developing all solid-state thin film microbatteries for microelectronic applications such as stand-by power sources on CMOS memory chip, microsensors and microactuators [Zha97a, Zha97b].

In Li-ion batteries, the cathode is typically lithium transition metal oxide such as $LiCoO_2$, $LiNiO_2$ and $LiMn_2O_4$ that are all possible to incorporate lithium ions in a reversible intercalation/deintercalation process. Lithium manganese oxide has attracted attention for the cathode in the Li-ion battery industry due to the merits over the others. Manganese is abundant, cheap and environmentally benign compared with cobalt and nickel [Arp88, Sit85].

However, $LiMn_2O_4$ has some critical issues to be overcome before it is widely used: capacity fade upon cycling and/or storage at 3 ~ 4 V regions and poor discharge rate capability at high current density. Mechanisms responsible for capacity fade have been introduced by several research groups: (1) Jahn-Teller distortion due to the anisotropic expansion/contraction during cycling, (2) dissolution of manganese through the disproportionation of Mn^{3+} in the electrolyte, and (3) instability of $LiMn_2O_4$ with two-phase structure [Cho99, Tha95, Sun00, Xia98]. The capacity fade on cycling is strongly dependent on the stability of the host structure to the repeated insertion/extraction of lithium ions during the discharge/charge. The rate capability is another limitation factor of $LiMn_2O_4$. It has been reported that the high discharge rate performance of the Li/$LiMn_2O_4$ cell is limited by the chemical diffusivity of lithium ions [Lin95, Jan00]. Therefore, the rate capability of $LiMn_2O_4$ is significantly dependent upon crystallinity and microstructure of the spinel such as particle or grain size, uniformity of grains, and specific surface area.

The purpose of this study is to understand the fundamental relation between structure and electrochemical characteristics of $LiMn_2O_4$ thin film cathodes and to pursue optimum properties such as higher capacity retention and rate capability using the pulsed laser deposition (PLD) technique.

In chapter 2, an overview of the literature on related subjects to this research is presented. This consists of the reviews of Li ion batteries, $LiMn_2O_4$ and related structure, thin film synthesis techniques including PLD and ultraviolet-assisted PLD, and electrochemical measurement methods. Chapter 3 discusses the experimental procedures and characterization techniques for investigating the properties of thin film cathodes grown in this study. Three factors that affect the structure and properties of $LiMn_2O_4$ thin film cathodes have been studied in chapters 4, 5, and 6. Firstly, we examined the effect of growth temperature of thin film cathodes on the electrochemical properties. Different crystallinity, grain shape and size, and compositions of the cathodes as a function of temperature have been correlated to their performances as a cathode in a Li-ion rechargeable battery. Secondly, aluminum-doped $LiMn_2O_4$ thin film cathodes have been examined to improve the structural stability, leading to better electrochemical performance. The study of the effect of UV radiation during the growth of the thin film cathodes on the electrochemical characteristics of thin film cathode is followed. Finally, all conclusions of the experiment are summarized in chapter 7.

CHAPTER 2
LITERATURE REVIEW

Electrochemical Cell (Battery)

Fundamentals of Batteries

A battery is a device that converts the chemical energy of its active materials into electric energy by an electrochemical oxidation-reduction (redox) reaction. This reaction involves the transfer of electrons from one material to another through an electric circuit. While the term battery is often used, the basic electrochemical unit being referred to is the cell. A battery is composed of one or more of these cells connected in series or parallel depending on the desired voltage and capacity. The cell consists of three main components: The negative electrode (anode) gives up electrons to the external circuit and is oxidized during the electrochemical reaction. The positive electrode (cathode) accepts electrons from the external circuit and is reduced during the electrochemical reaction. The electrolyte provides the medium for transfer of charge as ions inside the cell between the anode and cathode. In a practical system, the anode must be an efficient reducing agent producing high coulombic output with stability and be fabricated with ease and low cost. The cathode must be an efficient oxidizing agent with stability to the electrolyte and have a useful working voltage. The electrolyte must have a good ionic conductivity but not be electronically conductive, which would cause internal short-circuiting. In addition, important properties required for the electrolyte are non-reactivity with the electrode materials, little change in properties in temperature, safety, and low cost. In a practical battery, a separator material is used to separate the anode and cathode electrodes mechanically to prevent internal short-circuiting. However, the separator is permeable to the electrolyte in order to maintain the desired ionic conductivity.

Electrochemical cells and batteries are classified as primary (non-rechargeable) and secondary (rechargeable) in terms of their capability of being electrically recharged. Primary batteries are not capable of being charged and thus are discharged once and discarded. These batteries are usually inexpensive and lightweight power sources for portable electronic and electric devices, lighting, camera, and other applications. The advantages of the primary batteries are good shelf life, high energy density at low and moderate discharge rate, and ease of use. Secondary batteries can be electrically recharged to their original condition by passing current in the opposite direction to that of the discharge current. The secondary batteries are used or discharged as a primary battery, but recharged after use rather than being discarded. Not only can secondary batteries be charged but also have high power density, high discharge rate, and good low temperature performance. Secondary batteries are being used in portable consumer electronics, power tools, and electric vehicles for saving cost since they can be recharged rather than replaced.

The operation of a cell during discharge and charge is shown in Figure 2-1 (a) and (b) [Lin02]. In the discharge process electrons flow from the anode, which is oxidized, through the external load to the cathode, where the electrons are accepted and the cathode material is reduced. Within the cell, working ions flow from the anode to the cathode to convert chemical energy into electrical energy, which is used as a power source. The electric circuit is completed in the electrolyte by the flow of anions and cations to the anode and cathode, respectively. In the charge process electrons flow is reversed and oxidation takes place at the positive electrode and reduction at the negative electrode. By definition, the positive electrode is now the anode and the negative the cathode. Within cell, working ions flow from the positive electrode (anode) into negative electrode (anode) to convert electrical energy, back into chemical energy. The electrical current delivered by the cell to the external load is matched by the ionic current within the cell in both discharge and charge.

Reactions take place at the electrode interfaces in a cell. The reaction at one electrode (reduction in forward direction) can be described by

$$aA + ne^- \leftrightarrow cC \tag{2.1}$$

where a molecule of A accept n electrons e^- to form c molecules of C. At the other electrode (oxidation in forward direction) can be represented by

$$bB \leftrightarrow dD + ne^- \tag{2.2}$$

The overall reaction in the cell is given by addition of these half-cell reactions.

$$aA + bB \leftrightarrow cC + dD \tag{2.3}$$

When a reaction occurs, there is a decrease in the free energy of the system, which is expressed by

$$\Delta G^\circ = -\, nFE^\circ \tag{2.4}$$

where F is a Faraday constant (96487 coulombs) and E° standard potential (standard electromotive force). The change in the standard free energy ΔG° of a cell reaction is the driving force that enables a battery to deliver electrical energy to an external circuit. The maximum electric energy delivered by the chemicals that are supplied to or stored within the electrode in the cell is dependent upon the change in free energy of electrochemical couple as shown in the above equation.

For a condition other than the standard state, the voltage E of a cell can be expressed by the Nernst equation as below

$$E = E^{\circ} - \frac{RT}{nF} \ln \frac{a_C^c a_D^d}{a_A^a a_B^b} \quad (2.5)$$

where a_i is an activity of relevant species, R is a gas constant, and T is an absolute temperature [Bar01].

The theoretical specific capacity of a cell is determined by the total quantity of electricity participated in the electrochemical reaction in the cell and is defined as coulombs or ampere-hours. Theoretically, 1 gram-equivalent weight of material will deliver 96487 C or 26.8 Ah. The theoretical specific capacity (Ah/kg) of an electrochemical cell is calculated from the equivalent weight of the reactants that is participitated in the electrochemical reaction. For example, the theoretical specific capacity of the primary Li/MnO_2 battery is 0.286 mAh/kg, that is,

$$\begin{array}{ccccc} \text{Li} & + & \text{Mn(IV)O}_2 & \rightarrow & \text{LiMn(III)O}_2 \\ (3.86\ \text{Ah/kg}) & & (0.308\ \text{Ah/g}) & & \\ 0.359\ \text{g/Ah} & + & 3.24\ \text{g/Ah} & = & 3.499\ \text{g/Ah or } 0.286\ \text{mAh/kg} \end{array} \quad (2.6)$$

The capacity density (Ah/L) can be also given by dividing the total quantity of electricity by the volume of active materials in the cell.

The theoretical energy of a cell based on watt·hour is determined by taking both the voltage and the quantity of electricity into consideration. This theoretical energy is the maximum value that can be delivered by a specific electrochemical system.

$$\text{Energy (Wh)} = \text{Voltage (V)} \times \text{Quantity of Electricity (Ah)} \quad (2.7)$$

The theoretical specific energy (Wh/kg) and energy density (Wh/L) are obtained by dividing the energy of a cell (Wh) by the weight and volume of the active materials involved in the electrochemical reaction in the cell, respectively.

The theoretical power of a cell is determined by the product of the electric current delivered by the cell and the voltage between the anode and cathode.

$$\text{Power (W)} = \text{Voltage (V)} \times \text{Current (A)} \tag{2.8}$$

The theoretical specific power (W/kg) and power density (W/L) are obtained by dividing the power of a cell (W) by the weight and volume of the active materials involved in the electrochemical reaction in the cell, respectively.

From the Equation (2.8), the maximum power of a battery can be obtained by both the maximum voltage and electric current.

$$W_{max} = V_{max} \times I_{max} \tag{2.9}$$

However, the potential is decreased from its open circuit value ($I = 0$) by the voltage drop due to the internal resistance R_b of the battery, which can be expressed as below

$$V = V_{ocv} - IR_b \tag{2.10}$$

The magnitude of the open circuit voltage is constrained not only by the attainable difference in electrochemical potentials of the anode and cathode, but also by the energy gap E_g between the highest occupied molecular orbital (HOMO) and the lowest unoccupied molecular orbital (LUMO) of a liquid electrolyte.

$$E_{ocv} = \frac{\mu_A - \mu_C}{-nF} \tag{2.11}$$

where μ_A and μ_C are the electrochemical potentials of the anode and cathode, respectively.

In order to maximize V_{ocv} with a thermodynamic stability the difference in the electrochemical potential $\mu_A - \mu_C$ should be less than the energy gap E_g of electrolyte.

Thus, the matching of the window E_g of electrolyte to the electrochemical potential difference between μ_A and μ_C is of an important factor.

In addition to as high E_{ocv} as possible, a low internal resistance R_b of the battery is required.

$$R_b = R_{el} + R_{in}(A) + R_{in}(C) + R_c(A) + R_c(C) \tag{2.12}$$

The electrolyte resistance R_{el} to the ionic current is increased with increasing the effective thickness but decreased with increasing the area filled with electrolyte. Thus, the usage of a separator with a large geometrical area and small thickness is favorable to reduce the R_{el}. The electrolyte-electrode interface resistance R_{in} to the transport of the working ions is increased with increasing the geometrical area at the electrodes but decreased with increasing the interfacial area. A high electrode capacity can be achieved and retained by the utilization of a high fraction of the electrode material provided a good electronic contact between particles is obtained and maintained without significant fracture of particles over the repeated charge/discharge cycles. Finally, current from the large area electrodes must be collected to the anode and cathode, and a clever geometrical design is needed to assemble the cell into a small package that minimizes the current collector resistance R_c of each electrode.

Li-ion Batteries

Lithium is a theoretically attractive material for negative electrodes of electrochemical cells because of its least noble nature and low specific gravity. Primary cells with metallic lithium negative electrodes and non-aqueous electrolytes came into existence in the early 1960s and they were successfully introduced into the market. Their outstanding features in comparison with conventional batteries with aqueous electrolytes are [Bro99a] higher voltage, higher energy density and specific energy, lower self-discharge rate, and wider temperature range of operation.

Thus, rechargeable batteries with metallic lithium negative electrodes have attracted much attention as a candidate for the battery with high energy density, and much effort has been made in developing rechargeable lithium batteries. However, many practical problems have been encountered in development of rechargeable lithium batteries. Among them are poor cycle performance, need for long charging time, and poor safety characteristics. Most of these issues are due to the dendritic lithium formation during cycling. Dendrites are apt to penetrate into the separator and to cause an internal short circuit between positive and negative electrodes, which creates problems such as poor cycle performances and undesirable safety characteristics. Thus, another type of rechargeable battery using a lithiated carbon or other intercalation materials for the negative electrode in place of lithium has been introduced. It has been confirmed that a lithium–graphite intercalation compound (Li–GIC) is an excellent material for a negative electrode, which inherits advantages of metallic lithium without the issue of lithium dendritic formation [Ros90]. It is possible to synthesize lithium/carbon alloys by the direct chemical reaction of lithium and carbon, but they do not admit a mass production. The usual feature is that pure carbon is used in a negative electrode in place of an alloy and a lithium-containing compound like $LiCoO_2$ is applied to a positive electrode. Lithium ions are extracted (deintercalation) electrochemically from $LiCoO_2$ during the charge of a cell in aprotic electrolytes and are inserted (intercalation) into a carbon negative electrode to form a lithium/carbon alloy. During discharge, lithium ions are extracted from the alloy and inserted back into $LiCoO_2$.

Graphite has a layered structure and it is electrochemically reduced in an aprotic organic electrolyte containing lithium salts, and lithium is intercalated between the layers of graphite to form Li–GIC. Li–GIC is able to be charged and discharged as a rechargeable negative electrode for nonaqueous electrolyte cells according to the following reaction:

$$Li_aC \rightarrow Li_{a-x}C + x\,Li^+ + e^- \qquad (2.13)$$

When a negative electrode is discharged, lithium is deintercalated from lithiated graphite and lithium ions dissolve into the electrolyte. The lithium content in the $LiCoO_2$ electrode reversibly changes during charge and discharge as indicated in the following equation:

$$LiCoO_2 \rightarrow Li_{1-x}CoO_2 + xLi^+ + e^- \qquad (2.14)$$

In the $LiCoO_2$/graphite cell system, the overall cell reaction is as follows:

$$LiCoO_2 + Li_{a-x}C \rightarrow Li_{1-x}CoO_2 + Li_aC \qquad (2.15)$$

This equation indicates that the cell reaction is simple migration of lithium ions between positive and negative electrodes and no metallic lithium is present in the system. To make a distinction from conventional lithium batteries, this battery system has been called ‘‘lithium ion secondary battery’’ because a particular ionic bond compound ($LiCoO_2$) is used as a positive electrode and only lithium of an ionic state is found in a negative electrode. The first Li-ion battery was commercialized in 1990 by SONY Co [Nag90]. A schematic of the electrochemical process in a Li-ion battery is shown in Figure 2-2 in which $LiMO_2$ represents the metal oxide positive materials, such as $LiCoO_2$, and C the carbonaceous negative material, such as graphite [Ehr02].

Li-ion battery has outstanding properties as follows [Nis01]:

1. High voltage,

2. High volumetric and gravimetric energy density,
3. Low self-discharge rate,
4. No memory effect,
5. Quick charge acceptance,
6. Excellent cycle life, and
7. Wide temperature range of operation.

In a practical Li-ion battery system, the positive electrode (cathode) is typically metal oxide with a layered ($LiCoO_2$, $LiNiO_2$) or tunneled structure ($LiMn_2O_4$), which is of interest in this research and will be discussed in the next section.

Lithium Manganese Oxide ($LiMn_2O_4$)

Positive electrode in Li-ion batteries uses a lithiated transition metal oxide as an active material. It has been known that $LiCoO_2$, $LiNiO_2$, and $LiMn_2O_4$ showed the practical discharge capacity over 4 V (vs. Li/ Li^+) through the reversible intercalation/deintercalation of Li^+ during cycling [Miz80, Tha84, Tho85]. Among them, $LiMn_2O_4$ has attracted much attention as a positive electrode in Li-ion battery due to its advantages over others; Mn is abundant and much cheaper than Co and Ni, and has a friendlier impact on the environment as shown in Table 2-1. Additionally, $LiMn_2O_4$ has a highest thermal stability range especially when overcharged and a higher discharge voltage [Bro99b, Nis01].

Table 2-1. Cost, reserves, and environmental limit of transition metals [Arp88, Sit85].

	Mn	Ni	Co
Cost (\$/kg)	0.5	13	25
Reserves (ppm)	950	75	25
Exhaust limit (mg/m^3)	5	1	0.1
Drainage limit (mg/l^3)	200	13.4	0.7

However, in order for $LiMn_2O_4$ to be extensively used, critical issues that need to be addressed are the capacity fade upon cycling and the rate capability at high charge/discharge rate. Capacity fade of the Li-ion cells with $LiMn_2O_4$ is the result of multiple processes, which are related solely to the positive electrode and/or to the interaction of it with the electrolyte and negative electrode [Ant98]. Several possible mechanisms have been proposed as origins of the capacity fade: (1) the onset of Jahn-Teller distortion [Tha95, Guo96, Sun00], (2) dissolution of Mn into the electrolyte [Bly98, Cho99, Kan96, Rob97, Xia98], (3) structural instability of $LiMn_2O_4$ [Xia96a, Xia97a, Xia98], and (4) decomposition (oxidation) of the electrolyte [Jan96, Xia97a].

The discharge rate capability is another limitation factor of $LiMn_2O_4$. It has been found that the high rate performance of the Li/ $LiMn_2O_4$ cell was mainly limited by the rate of chemical diffusivity of lithium ions. Thus, rate capability of $LiMn_2O_4$ is significantly dependent on the crystallinity and microstructure of the spinel (particle or grain size, surface area, size distribution of the particle, agglomeration, etc.) [Jai96, Jan00, Nag00].

Capacity Fade and Rate Capability

The structure of spinel $LiMn_2O_4$ is composed of a cubic close-packed array in which the lithium ions are located at the 8a tetrahedral sites, one-eight of the total tetrahedral sites with empty 8b and 64f sites. The manganese ions occupy the 16d octahedral sites while the 16c octahedral sites remain empty. The oxygen ions are located at the 32e sites of space group $Fd\bar{3}m$ [Tha83, Yam95]. The schematic unit cell structure of the spinel $LiMn_2O_4$ is shown in Figure 2-3 [Goo98]. The Mn_2O_4 framework is an attractive host structure for lithium insertion/extraction reactions because MnO_6 octahedra are edge-shared and provide a stable three-dimensional network for lithium ion diffusion. Lithium ions diffuse in and out of the structure via the open framework of linked 8a tetrahedral sites and 16c octahedral sites [Amm97].

A stoichiometric spinel Li/$LiMn_2O_4$ cell exhibits two voltage plateaus at 4 V with two sub-plateaus and 3 V vs. Li/Li^+. Figure 2-4 represents the variation of voltage versus x in $Li_{1+x}Mn_2O_4$ and $Li_{1-x}Mn_2O_4$ in Li/$LiMn_2O_4$ cell [Goo02]. The voltage plateau at 4 V is associated with the electrochemical insertion/extraction of lithium ions in spinel $LiMn_2O_4$ as in the following reversible reaction:

$$LiMn_2O_4 \leftrightarrow Li_{1-x}Mn_2O_4 + xe^- + xLi^+ \qquad (2.16)$$

The $Li_{1-x}Mn_2O_4$ spinel phase exhibits two distinct voltage plateaus, at 4.2 V in the range of $0.5<x<1$ and at 4.0 V in the range of $0<x<0.5$, generally assigned to some order-disorder transition in the cubic spinel caused by lithium ion insertion/extraction.

The voltage plateau at 3 V is due to Li^+ insertion into cubic $LiMn_2O_4$ to from tetragonal $Li_2Mn_2O_4$.

$$LiMn_2O_4 + xe^- + xLi^+ \leftrightarrow Li_{1+x}Mn_2O_4 \qquad (2.17)$$

When lithium is inserted into the spinel $LiMn_2O_4$ to form $Li_2Mn_2O_4$, a Jahn-Teller distortion known as a cooperative local distortion occurs. The insertion of lithium into $LiMn_2O_4$ is accompanied by a reduction in the average oxidation state of manganese from 3.5 to 3; the Mn^{4+} of $d^3(t_{2g}{}^3)$ configuration is reduced to the Mn^{3+} of $d^4(t_{2g}{}^3e_g{}^1)$ configuration with an extra electron on the e_g orbital. The $e_g(d_{x^2-y^2})$ and $e_g(d_{z^2})$ orbitals have the same energy and are orbitally degenerated. The complex will then distort to remove the degeneracy and achieve a lower energy. Most common the electron occupies the $e_g(d_{z^2})$ orbital, resulting in an elongation of two axial bonds and compression of the four bonds in a plane. The Jahn-Teller distortion of the d^4 electron configuration is illustrated in Figure 2-5 [Bjö02]. The presence of more than 50% of Jahn-Teller ions (Mn^{3+}) in the host structure introduces a cubic to tetragonal distortion (from $c/a = 1$ to $c/a = 1.16$, $\Delta V/V = 6\%$) [Bar93, Koe95, Mac91, Tha92]. When insertion of lithium into $Li_{1+x}Mn_2O_4$ occurs at 3 V for ($0<x<1$), it causes a first order transition to a rock salt phase $Li_2Mn_2O_4$ during which the tetrahedrally coordinated lithium ions are cooperatively displaced into the octahedral sites (16c). The increase in Mn^{3+} concentration within the spinel framework reduces the symmetry of the structure from cubic in $LiMn_2O_4$ to tetragonal in $Li_2Mn_4O_4$. The large anisotropic expansion of the unit cell that is reflected by the 16% increase in the *c* parameter is too severe for the cubic and tetragonal phases to remain as one intergrown structure. The incompatibility between the oxygen arrays of the cubic and tetragonal phase causes the electrode to fracture at the particle surface. This effect destroys structural integrity and particle-to-particle contact, which are essential for maintaining the electronic conductivity of the electrode. This large anisotropic (Jahn-Teller) distortion ($c/a = 1.16$) is generally believed to be largely responsible for poor cycling behavior of the spinel electrode at 3 V [Gum94, Tha98, Yam95]. A rapid capacity fade on cycling in the 3 V region has limited application of lithium manganese oxide spinel to the 4 V region [Kan01].

Although capacity fade due to the Jahn-Teller distortion is predominant at 3 V range, the Jahn-Teller effect has been also observed at 4 V range on cycling. Eriksson *et al.* reported that Mn^{3+} rich surface was detected by XPS study from the $LiMn_2O_4$ cycled over 3.5 ~ 4.5 V for 50 cycles [Eri02]. They attributed the Mn^{3+} rich surface to the fact that the surfaces of some particles with residual lithium after charge could reach a

$Li_{1+x}Mn_2O_4$ composition, in which the average oxidation state of manganese decreased below 3.5. Gummow *et al.* postulated that some capacity fade could also be attributed to the formation of $Li_2Mn_2O_4$ at the spinel surface at the end of discharge of 4 V Li/$Li_xMn_2O_4$ cells, particularly under high rate, non-equilibrium conditions [Gum94]. It was subsequently shown by Liu *et al.* that, after 80 continuous cycles of 4 V Li /$Li_xMn_2O_4$ cells when charged and discharged at a high rate between 4.5 and 3.5 V, there was evidence of tetragonal $Li_2Mn_2O_4$ in the electrode at 3.5 V, even though this phase is thermodynamically unstable above 3 V: its existence was attributed to kinetic limitations at the electrode surface during fast intercalation [Liu96]. The presence of tetragonal $Li_2Mn_2O_4$ on the surface of discharged $LiMn_2O_4$ electrodes was verified more recently by transmission electron microscope (TEM) imaging and electron diffraction data even after a few cycles at high rate [Tha98].

Capacity fade on cycling of the Li-ion cells has been ascribed to the dissolution of manganese from $LiMn_2O_4$ into the electrolyte solution by Gummow *et al.* [Gum94]. As an evidence of the dissolution of manganese, Tarascon *et al.* reported the presence of Mn on the surface of negative electrode by RBS [Tar94]. The Mn on the anode surface was deposited by reduction of the dissolved Mn. In a study of $Li_xMn_2O_4$ electrodes by Fourier transform infrared spectroscopy (FTIR), Wen *et al.* concluded that capacity fade upon cycling in the higher voltage region was attributed to the dissolution of Mn in the electrolyte and the formation of defect spinel phase with Mn^{4+} [Wen96]. Robertson *et al.* suggested that the capacity decline could be attributed to the disproportionation of the spinel electrode into as acid-soluble (Mn^{2+}) and compounds containing Mn^{4+} such as Li_2MnO_3 [Rob97]. In a study of Li-Mn-O spinel electrodes that had been stored at 55°C in a 1 M $LiPF_6$ ethylene carbonate (EC)/ dimethylne carbonate (DMC) electrolyte, Blyr *et al.* reported that manganese dissolution changed the spinel composition with the concomitant formation of rock salt Li_2MnO_3 at the particle surface [Bly98].

Structural changes can occur at the spinel electrode because of the instability of the lithiated and delithiated Li-Mn-O phase in acidic nonaqueous electrolyte. For example, the acidity of electrolytes containing a $LiPF_6$ salt can produce hydrofluoric acid that is formed by the reaction of $LiPF_6$ with residual water in the organic solvent, as proposed by Aurbach and Gofer [Aur91] and Aurbach *et al.* [Aur95].

$$LiPF_6 + H_2O \rightarrow LiF + POF_3 + 2HF \tag{2.18}$$

Hunter reported that acid treatment of $LiMn_2O_4$ resulted in the defect spinel product λ-MnO_2 [Hun81]. The chemical reaction

$$2LiMn_2O_4 \rightarrow 3\lambda\text{-}MnO_2\ (\text{solid}) + MnO\ (\text{solution}) + Li_2O\ (\text{solution}) \tag{2.19}$$

differs from the electrochemical reaction

$$LiMn_2O_4 \rightarrow \lambda\text{-}MnO_2 + Li^+ + e^- \tag{2.20}$$

because in the chemical reaction lithium and manganese are dissolved from the structure as Li_2O and MnO, respectively. The spinel dissolves because the Mn^{3+} ion is unstable in acid; the Mn^{3+} ion disproportionate according to the reaction

$$2Mn^{3+} \rightarrow Mn^{4+} + Mn^{2+} \tag{2.21}$$

The dissolution of manganese, as MnO, is responsible for the change in oxidation state of the manganese ions in defect spinel framework (λ-MnO_2). The disproportionation reaction of $LiMn_2O_4$ in acid is dictated by the relative dissolution of MnO and Li_2O.

The presence of Li_2MnO_3 is attributed to the dissolution of MnO from $Li_2Mn_2O_4$ that is generated as an over-discharged product at the surface of the $LiMn_2O_4$ spinel electrode [Cho99].

$$Li_2Mn_2O_4 \rightarrow Li_2MnO_3 + MnO \tag{2.22}$$

The direct transformation of $Li_2Mn_2O_4$ to Li_2MnO_3 can be attributed to several factors: (1) the dissolution of Mn from $Li_2Mn_2O_4$ leaves the exact Li:Mn ratio required to form Li_2MnO_3, (2) Li_2MnO_3 has a rock salt structure which is fully oxidized and contains insoluble Mn^{4+} ions, and (3) Li_2MnO_3 is thermodynamically more stable than defect spinel, such as λ-MnO_2.

Xia *et al.* reported that capacity fade during cycling of the spinel electrode at room temperature occurred only in the high voltage region (4.15 ~ 4.5 V in the charge curve) and it was caused mainly by an unstable two-phase structure coexisting in this region for lithium ion insertion/extraction [Xia96a, Xia96b, Xia97a]. They proposed that the one-phase structure of spinel in the low voltage region (3.0 ~ 4.15 V) was stable for lithium ion insertion/extraction but two-phase structure in the high voltage region was not stable [Xia97a]. It was observed that an unstable two-phase transformed to stable one-phase structure at elevated temperature. Thus, they also proposed that major factor in capacity fade at elevated temperature was attributed to the change in the unstable two-phase accompanied by loss of MnO and spinel electrode could directly lose Mn_2O_3 at a high temperature, which would further cause the capacity loss [Xia98]. In addition, Blyr *et al.* showed the poor capacity retention after storage of Li-ion cell (Li/$LiMn_2O_4$) in the discharge state at 55°C owing to the instability of spinel $LiMn_2O_4$ with respect to Mn dissolution [Bly98]. They concluded that Mn dissolution by long storage at 55°C induced a deterioration of the spinel into a defect spinel phase in the composition triangle $LiMn_2O_4$- $Li_2Mn_4O_9$- $Li_4Mn_5O_{12}$. It is worth noting that despite the substantial decrease initial capacity due to the self-discharge of $LiMn_2O_4$ Li-ion cells in their discharge state at 55°C, these cells exhibited good capacity retention upon cycling.

Capacity fade upon cycling is also attributed to instability of the electrolyte. Decomposition of the electrolyte includes reaction of the solvent at electrode surface to yield a passive layer (Solid Electrolyte Interphase or SEI), resulting in an increase in electrode resistance [Jan96, Mor97, Xia97a]. The increase in electrode resistance will cause a high cell polarization, leading to incomplete charging and therefore apparent capacity losses. It is advantageous to synthesize electrode material with a small surface area to reduce the decomposition of electrolyte.

Gao *et al.* suggested that self discharge in an open-circuit $LiMn_2O_4$ /C cell in the charged state (4.7 V) be attributed to electrolyte oxidation at the $LiMn_2O_4$ surface [Gao96, Gum94]. Lithium intercalation into the spinel was proposed to accompany the electrolyte oxidation to balance the charge. Electrolyte oxidation is very likely to take place at the surface of highly delithiated spinel, which is very electron acceptive as it is positively charged. Basically, the electrolyte molecule acts as an electron donor to the partially delithiated spinel and induces the oxygen loss. The oxygen loss from the sample during cycling not only causes possible structural damage to the spinel, but also oxidizes the electrolyte and shortens the cell life.

Another limiting factor of $LiMn_2O_4$ used in Li-ion batteries is relatively poor performance at high charge/discharge rate. The transport and diffusion of lithium ions through the electrolyte, at the surface and inside electrode are thought to be the rate limiting process. First, solvated lithium ions are transported through the electrolyte whose ionic conductivity plays a major role in this process. Li^+ can transport rapidly in the electrolyte with high ionic conductivity. The next step is the desolvation of Li^+ at the electrode surface. This step is dependent on availability of active surface area contacted with the electrolyte. Interfacial resistance between the surface of the electrode and the electrolyte may restrict the transport of Li^+. As the surface area increases the lithium ion kinetics increases. Finally, the diffusion of lithium ions in the host structure occurs along the surface to the intercalated sites. Diffusion of lithium ions depends on the number of sites available, the diffusivity of Li^+, and conductivity [Lin95].

Several routes have been used to synthesize the spinel $LiMn_2O_4$. In spite of the very different characteristics of methods and starting materials used, the heat treatment in the range of 700 ~ 900°C have been performed to obtain the highly crystalline spinel $LiMn_2O_4$.

Even though the lithium manganese oxides produced at the lower temperature were found to include other undesirable phases such as Mn_2O_3, they showed significantly higher rate capabilities than those for materials treated at high temperature [Man95, Tar95, Zho95]. This higher rate capability was attributed to relatively small particle size and large specific surface area, which reduce the diffusion length of Li ions during the intercalation/deintercalation and increase the active area in contact with the electrolyte.

Naghash *et al.* reported that the small particle size of lithium manganese oxide produced by co-precipitation method showed higher rates of lithium insertion/extraction from the oxide host [Nag00]. Also Jang *et al.* showed that Li-ion batteries with $LiMn_2O_4$ composed of particles in the form of small, uniformly sized and unagglomerated exhibited good capability over a wide range of rates [Jan00]. This result can be correlated with an increase in lithium surface reaction sites as inferred by small grain size and large surface area.

Since the radius of lithium ion and the tetrahedral site size are 0.67 Å and 0.38 Å, respectively, lithium ions should move through a narrow diffusion path so that much stress could be imposed in the surrounding during the intercalation/deintercalation [Pyu97]. From that fact Myung *et al.* proposed that lithium manganese oxide with relatively poor crystallinity made at lower temperature might be able to relax the strain during intercalation/deintercalation, resulting in improvement of rate capability due to the increase in diffusivity of lithium ions [Myu00]. However, Xia *et al.* speculated that a large surface area would prompt Li/$LiMn_2O_4$ cell to lose capacity at the elevated temperature because of an increase in the amount of manganese dissolution into the electrolyte. Therefore, the spinel $LiMn_2O_4$ with a small surface area is recommended for use as a cathode for Li-ion batteries at elevated temperature [Xia00]. The most critical issue for wide use of lithium manganese oxide with respect with the rate capability would be to optimize the microstructure (particle size, surface area, crystallinity) without significant loss of the capacity on cycling and storage in the practical temperatures (-20 ~ 90°C).

Thin-film Lithium Manganese Oxide ($LiMn_2O_4$)

Among several advantages of the solid-state devices, the most important feature is the miniaturization of the systems. Progress in the miniaturization of the electronic devices has reduced the current and power requirements to extremely low levels, making possible solid-state thin-film microbatteries for microelectronics applications such as stand-by power sources on complementary metal oxide semiconductors (CMOS) memory chips [Bat93]. Moreover, the high capacity and/or voltages, depending on the ways of stacking of the cells (parallel or series), might be obtained by multi-cell thin-film batteries. A schematic cross section of a thin film Li-ion battery is shown in Figure 2-6 [TFB01]. Another possible application of the thin-film batteries is to couple them with microsensors and microactuators [Zha97a, Zha97b].

In addition to practical applications, the fundamental study of the intercalation of lithium in oxides is necessary to better understand physical, chemical, and electrochemical phenomena observed. However, since most studies of lithium manganese oxide performed from the porous bulk material with polymer as a binder and carbon as a conductivity enhancer, which may affect the properties observed, the fundamental studies about intrinsic properties of lithium manganese oxide were probably interfered. Thus, thin-film $LiMn_2O_4$ representing a geometry that overcomes many uncertainties caused by additives is of great interest in a fundamental point of view.

Thin-films of lithium manganese oxide have been synthesized by various methods such as reactive electron beam evaporation [Sho91], radio frequency magnetron sputtering [Dud99, Hwa95, Par99], chemical vapor deposition (CVD) [Liu99], pulsed laser deposition (PLD) [Str96], and spin coating [Mat01, Par00a, Par00b]. Shokoohi *et al.* reported that $Li_xMn_2O_4$ ($x \leq 1$) film annealed at 800°C was cycled about 70 times before the capacity dropped to 50% of initial capacity in the range of 3.5 ~ 4.5 V. They concluded the decrease in capacity on cycling was attributed to solvent oxidation in the electrolyte at potential higher than 4 V. They detected small amounts of nickel impurities in the film on the nickel substrate due to the diffusion of nickel into the thin-film spinel at elevated temperature (800°C) [Sho91]. Dudney *et al.* synthesized $Li_xMn_{2-y}O_4$ ($1.2 < x < 2.2$, $y = \sim 0.3$) films by using RF magnetron sputtering at relatively low temperatures (60 ~ 200°C), resulting in nanocrystalline (~50 Å) with Mn deficiency leading to the high cyclability over 1000 cycles in the range of 2.5 ~ 4.5 V. However, the maximum discharge rate was limited to low values in the range of 50 $\mu A/cm^2$, corresponding to about 0.5 C rate. Also the films had a wide range of Li/Mn ratio, which might be problematic for the practical synthesis [Dud99]. Thin-film of $LiMn_2O_4$ deposited by RF magnetron sputtering followed by rapid thermal anneal (RTA) at 750°C for 60 seconds had significantly small grains in size about 0.05 μm resulting in enhanced cycling performance [Hwa95]. But it needed the buffer layer as a barrier between $LiMn_2O_4$ film and substrate at high temperature. Additionally, for the optimum films, there were very complicate and uncertain variables such as total gas pressure of mixture of Ar/O_2, the ratio of Ar to O_2, annealing temperature, annealing time, annealing atmosphere, and so on. Thus, there must be no unambiguous condition for the film, which exhibits excellent electrochemical properties. Striebel *et al.* reported that PLD grown $LiMn_2O_4$ yielded good initial capacity with moderate capacity fade but poor discharge rate capability. For 1 μm film, the discharge capacity dropped to about 50% of the initial value as the current density increased 10 times [Str96].

In addition to vapor-phase based coatings, spin coating has been widely used to produce the thin-film lithium manganese oxide. In spin coating method, the effects of drying of the solution coated on the substrate on film properties are critical. If the temperature is too low, organic materials will remain even after annealing causing many defects, which affect the film properties [Par00a, Par00b]. Park *et al.* reported that the discharge capacity of the annealed films increased with the drying temperature. It can be inferred that as the dry temperature increases, the perfection of the spinel framework is increased leading to better ability for intercalation/deintercalation of Li ions per unit volume. However, the rechargeability of the films dried at higher temperatures was inferior to that of the films dried at lower temperature. They proposed that small defects such as microvoids and vacancies in the film dried at lower temperature might offer vacant room for a small flexible shift in the lattice during the cycle resulting in suppression of stresses generated by intercalation/deintercalation.

It is worth noting that thin-film $LiMn_2O_4$ grown by various techniques is subjected to high temperature during either deposition or annealing to gain high crystallinity with low stress giving rise to a stable spinel phase. However, processing at high temperatures may exert the harmful effects. Due to the grain growth at high temperature, the surface area of the cathode contacted with the electrolyte is reduced, inducing the higher cell resistance. The amount of lithium in films is decreased at high temperature because of its high vapor pressure. The electrochemical properties of lithium manganese oxide significantly depends on the lithium, thereby, the deficiency of lithium affects the properties of the Li-ion batteries. Diffusion of active species between the film and substrate at high temperature could give rise to alternation of the characteristics of the film and substrates. It is impossible for substrates, which cannot withstand given heat, to be used at high temperature.

Oxygen-rich Spinel ($Li_{1-\delta}Mn_{2-2\delta}O_4$)

For the spinel $LiMn_2O_4$ ($Li_{8a}[Mn_2]_{16d}O_4$) electrochemical extraction of one lithium ion from the tetrahedral (8a) sites occurs in two steps at approximately 4 V vs. Li/Li^+

($LiMn_2O_4 \rightarrow Mn_2O_4$ (λ-MnO_2)) whereas the insertion of one lithium ion into the octahedral (16c) site occurs at approximately 3 V vs. Li/Li^+ ($LiMn_2O_4 \rightarrow Li_2Mn_2O_4(LiMnO_2)$). Although the cubic symmetry of the spinel structure is maintained in the 4 V region, a cubic-tetragonal transition (Jahn-Teller distortion) occurs in the 3 V region as the average oxidation state of Mn drops below 3.5 accompanied by 16% increase in *c*/*a* ratio and 6% increase in volume. This anisotropical expansion/contraction on cycling is too severe for the electrode to maintain structural integrity leading to the electrical isolation on the electrode, consequently, it results in the capacity fade upon electrochemical cycling. Thus, the Jahn-Teller distortion has limited the use of spinel $LiMn_2O_4$ to only 4 V region. However, in the 4 V region the tetragonal grains formed on the surface of the electrodes under non-equilibrium condition are also believed to be one of the reasons for the observed capacity fade on cycling.

Several strategies have been pursued over the years to overcome the difficulties of the spinel $LiMn_2O_4$ cathodes. One important strategy is to develop spinel manganese oxides with an oxidation state of 4+ for manganese. The high oxidation state of manganese can suppress or delay the occurrence of Jahn-Teller distortion upon intercalation/deintercalation. With this perspective, the Li-Mn-O system has been investigated by several research group trying to synthesize the defect (oxygen-rich) spinel lithium manganese oxide, which can be represented as $Li_{1-\delta}Mn_{2-2\delta}O_4$ ($0 \leq \delta \leq 0.11$). Kock *et al.* reported the defect spinel $Li_2Mn_4O_9$ ($\delta = 0.11$) was synthesized at 400°C with lithium and manganese carbonates and confirmed by neutron diffraction as a notation $[Li_{0.89}\square_{0.11}]_{8a}[Mn_{1.78}\square_{0.11}]_{16d}O_4$ where $\square$ represent vacancies [Koc90]. The additional oxygen concentration which created defects on the 8a (tetragonal) and 16d (octahedral) sites gave

($LiMn_2O_4 \rightarrow Mn_2O_4$ (λ-MnO_2)) whereas the insertion of one lithium ion into the octahedral (16c) site occurs at approximately 3 V vs. Li/Li^+ ($LiMn_2O_4 \rightarrow Li_2Mn_2O_4$($LiMnO_2$)). Although the cubic symmetry of the spinel structure is maintained in the 4 V region, a cubic-tetragonal transition (Jahn-Teller distortion) occurs in the 3 V region as the average oxidation state of Mn drops below 3.5 accompanied by 16% increase in *c*/*a* ratio and 6% increase in volume. This anisotropical expansion/contraction on cycling is too severe for the electrode to maintain structural integrity leading to the electrical isolation on the electrode, consequently, it results in the capacity fade upon electrochemical cycling. Thus, the Jahn-Teller distortion has limited the use of spinel $LiMn_2O_4$ to only 4 V region. However, in the 4 V region the tetragonal grains formed on the surface of the electrodes under non-equilibrium condition are also believed to be one of the reasons for the observed capacity fade on cycling.

Several strategies have been pursued over the years to overcome the difficulties of the spinel $LiMn_2O_4$ cathodes. One important strategy is to develop spinel manganese oxides with an oxidation state of 4+ for manganese. The high oxidation state of manganese can suppress or delay the occurrence of Jahn-Teller distortion upon intercalation/deintercalation. With this perspective, the Li-Mn-O system has been investigated by several research group trying to synthesize the defect (oxygen-rich) spinel lithium manganese oxide, which can be represented as $Li_{1-\delta}Mn_{2-2\delta}O_4$ ($0 \leq \delta \leq 0.11$). Kock *et al.* reported the defect spinel $Li_2Mn_4O_9$ ($\delta = 0.11$) was synthesized at 400°C with lithium and manganese carbonates and confirmed by neutron diffraction as a notation $[Li_{0.89}\square_{0.11}]_{8a}[Mn_{1.78}\square_{0.11}]_{16d}O_4$ where $\square$ represent vacancies [Koc90]. The additional oxygen concentration which created defects on the 8a (tetragonal) and 16d (octahedral) sites gave

$Li_2Mn_4O_9$ a significantly great theoretical electrode capacity (213 mAh/g) as discharged to the rock salt composition $Li_5Mn_4O_9$ (3 Li^+ per unit formula) at 3 V region. However, extensively lithiated $Li_{2+x}Mn_4O_9$ sample for x>2 (deeply discharged) of which an average oxidation state of Mn is below 3.5 showed a second phase as similar process for $Li_{1+x}Mn_2O_4$ ($0.08<x<1.0$) inducing a Jahn-Teller distortion. Defect spinel ($Li_2Mn_4O_{9-\delta}$) containing lithium and manganese vacancies showed much better cyclability (less capacity fade) than that of spinel electrode at 3 V region due to the increase in the average oxidation state of Mn, resulting in the suppression of the Jahn-Teller distortion [Mas96]. Also $Li_2Mn_4O_{9-\delta}$ with $0.36<\delta<0.46$ showed a reversible capacity of about 130 mAh/g in the range of 2 ~ 3.8 V with excellent cyclability [Cho00].

In addition to 3 V region, Xia *et al.* reported that the optimized defect spinels could be reversibly cycled with excellent rechargeability relatively to the spinel $LiMn_2O_4$ at 4 V region at the expense of slight loss of capacity [Xia96c, Xia97b]. The semi-quantitative Li-O-Mn phase diagram is shown in Figure 2-7 [Xia97b]. The line between $LiMn_2O_4$ and $Li_4Mn_5O_{12}$ represents the Li-rich spinel ($Li_{1+\delta}Mn_{2-\delta}O_4$) in which excess lithium replace manganese in the octahedral sites (16d) while the line between $LiMn_2O_4$ and $Li_2Mn_4O_9$ for the oxygen-rich spinel ($Li_{1-\delta}Mn_{2-2\delta}O_4$). The dotted-lines parallel along the *xz* line represent the Li/Mn ratio in the range of 0.5 ~ 0.8 and those parallel along the *yz* line represent the average oxidation state of Mn in the range of 3.5 ~ 4.0. The lattice parameter decreases with an increase in lithium and/or vacancy contents because the Mn ions are replaced by small Li^+ in Li-rich spinel and displaced in oxygen-rich spinel. Since the amount of Mn^{3+} decreases with increase in Li/Mn ratio and/or vacant rate, the capacity decreases while the rechargeability improves. They interpreted that the improvement of cyclability in Li-rich and oxygen-rich spinel was attributed to the small unit cell in which a homogenous insertion/extraction could proceed over the entire region. They proposed the optimized Li-Mn-O compositions of spinel to obtain both reasonable capacity and improved rechargeability in the 4 V region as shown the shade area (ABCD) in Figure 2-8 [Xia97b].

Aluminum-doped Spinel ($LiAl_xMn_{2-x}O_4$)

As mentioned earlier, the wide use of spinel $LiMn_2O_4$ as a cathode for the Li-ion batteries has been restricted by its poor rechargeability caused from several possible reasons; (1) dissolution of Mn into the electrolyte [Cho99, Bly98, Kan96, Rob97, Xia98], (2) the onset of Jahn-Teller distortion [Guo96, Sun00, Tha95], (3) decomposition (oxidation) of the electrolyte [Jan96, Xia97a], and (4) structural instability of $LiMn_2O_4$ [Xia96a, Xia97a, Xia98]. Numerous attempts have been employed to improve its cycle stability. Among them partial substitution of Mn with other metallic elements such as Co, Ni, and Al has shown to be a very effective way for improving the cycle performance of $LiMn_2O_4$ [Guo96, Tar91a, Woh97]. The lithium intercalation properties of $LiAl_xMn_{2-x}O_4$ have been reported by Le Cras *et al.* [LeC96]. Since aluminum is light in weight, abundant and relatively inexpensive, Al-substituted manganese spinel is expected to be a cathode material with higher specific energy, lower cost, and less toxicity.

By the neutron powder diffraction, Komaba *et al.* confirmed that Al was substituted selectively for Mn at the 16d sites in the $LiAl_{0.2}Mn_{1.8}O_4$ synthesized by the emulsion drying method [Kom02]. They also reported that $LiAl_xMn_{2-x}O_4$ exhibited excellent cyclability with showing relatively higher discharge capacity retention in the range of 3.4 ~ 4.3 V. It was thought that Al-doped cathode is more stable than an undoped cathode because the bonding of Al-O is much stronger than that of Mn-O, which is 512 kJ/mol for the former and 402 kJ/mol for the latter, respectively [Dea92]. This represents that expansion and/or contraction of the spinel structure with intercalation/deintercalation of lithium ions may be restricted by the Al substitution, suggesting that the lattice stabilization should be achieved in certain Al-doping range ($x = 0.2 \sim 0.3$). They concluded that the increased structural integrity and reduced strain during the repeated intercalation/deintercalation of lithium by Al doping resulted in excellent cyclability with relatively lower capacity fade at both room temperature and 45°C [Myu01]. Also, Hwang *et al.* reported that Al-doped $LiMn_2O_4$ cathode improved substantially the capacity retention of the spinel in the 4 V region. They explained that the enhanced cyclability was attributed to the two reasons. First, there may be a considerable decrease in the effect of Jahn–Teller distortion when substituting a small amount of Al for Mn in the spinel because the concentration of Mn^{3+} which induces Jahn–Teller distortion in the spinel is decreased. Second, there may be a reduction in spinel dissolution [Hwa01].

Yoshio and his co-workers reported that $LiAl_xMn_{2-x}O_4$ exhibited an excellent cyclability in the 4 V region but the rapid capacity fade at 3 V region. They ascribed the loss of capacity at 3 V region to the prevention of complete lithiation into the structure due to the increased cubic phase after first few cycles [Lee01].

Recently, the electrochemical study of Al-doped $LiMn_2O_4$ cathode films for microbatteries has been reported [Kim03]. $LiAl_xMn_{2-x}O_4$ cathode films synthesized by a novel process called Liquid Source Misted Chemical Deposition (LSMCD) exhibited more improved electrochemical rechargeability than spinel $LiMn_2O_4$film in the range of 3.5 ~ 4.3 V. They claimed that the substitution of Al^{3+} for Mn^{3+} increased Mn-O bonding strength in the spinel framework and suppressed the two–phase behavior of the unsubstitued spinel during the intercalation/deintercalation that is known as a main cause of the capacity fade in the 4 V.

Synthesis and Characterization of Thin Film Cathode

Pulsed Laser Deposition (PLD)

Pulsed Laser Deposition (PLD) has been known as one of the most convenient techniques to produce multicomponent and multilayered thin film since it provides conceptual and experimental simplicity. PLD has several advantages over other deposition techniques such as stoichiometric transfer of material, high deposition rate, non-equilibrium processing, reactive deposition, and simplicity for the growth of multilayered structures [Low96, Sin98]. These advantages have made the PLD to fabricate thin films for high-T_c superconductors [Sin98], dielectrics [Sri99], hard coating [Lee98], and luminescent applications [Cho98, Jon99].

Principle of excimer lasers

Excimer is an acronym for EXCIted diMER, a rare gas dimmer based on the rare gas halogen. Excimer lasers are high pressure and pulsed gas lasers that give rise to ultraviolet light with a wide range of wavelengths from 193 nm to 351 nm. Energy is pumped by avalanche electric discharge excitation in a gas mixture composing of a rare gas (Ar, Kr, Xe), a halogen gas (F, Cl), and a buffer gas (He, Ne). The pumping generates ionic and electrically excited species that react chemically and produce excimer molecules. Once excimer molecules are formed, they would decay rapidly emitting photons, which are the excimer lasers with wavelength in the UV range, during the transition from upper electronic state to lower ground state.

KrF is the most popular excimer laser in the laser research because it shows the highest gain among the electrically discharged pumped excimer lasers which are the gas lasers that emit powerful UV pulses lasting 10 to 50 nanoseconds [Low96]. The UV wavelengths have the highest absorption and lowest reflectivity for most materials. The primary reaction channels for KrF excimer laser are shown in Table 2-2.

Table 2-2. Primary reaction channels for KrF excimer [Ell95]. An asterisk(*) represents an electronically excited state of the species.

$F_2 + e^- \rightarrow F^- + F$	Electron Attachment
$Kr + e^- \rightarrow Kr^* + e^-$ $Kr^* + e^- \rightarrow Kr^+ + 2e^-$	2-step Ionization
$Kr^+ + F^- + Ne \rightarrow KrF^* + Ne$	3-body Excimer Formation Reaction
$KrF^* \rightarrow Kr + F + hv$ $KrF^* + hv \rightarrow Kr + F + 2hv$	Spontaneous Emission Stimulated Emission (Laser Action)
$F + F + Ne \rightarrow F_2 + Ne$	3-body Recombination (very slow)
$F_2 + hv \rightarrow 2F$ $F^- + hv \rightarrow F + e^-$	Photo Dissociation Photo Detachment

The reactions initiate from electron attachment to the fluorine molecule, followed by ionization of the krypton, excimer formation, and spontaneous and stimulated emission. The absorption reactions including photodissociation and photodetachment occur. Figure 2-9 shows the electronic states in the KrF excimer laser emission [Dul96].

Basics of PLD

A focused excimer laser beam is used as an energy source to induce the evaporation of a target material to grow. When the laser energy is absorbed by the target surface, it is converted to cause the evaporation, ablation, excitation, and plasma formation [Che94]. Evaporates form plasma (or plume) consisting of a mixture of ground- and excited-state neutral atoms, ions, molecules, and electrons. Since the collision mean free path inside the high-density plasma region (the Knudsen layer) near the target is very short, the plasma rapidly expands in a highly directional flow perpendicular to the target surface with initial velocities greater than 10^6 cm/s [Low98]. The substrate on which films are to be grown is mounted in the path of the plasma. Each laser pulse generates a new plume from the target and deposits new material on the film surface.

PLD shows several characteristics distinguished from other thin film deposition techniques. If appropriate laser density, beam spot size, and shape are selected, stoichiometric transfer of material from target to film can occur in a finite range of deposition angles. The stoichiometric (congruent) transfer can be achieved only if the laser energy density is high enough to form laser-generated plasma. This laser-generated plasma causes erosion of target material resulting in the stoichiometric transfer of all of the constituents of a complex and multielement material [Low98].

Since there is no electron beam or hot filaments in the deposition chamber, it is possible to deposit films through reactive deposition in ambient gases. Simple compound films can be obtained by reactive deposition if the proper ambient gas is introduced into the chamber. Also, collisions with ambient gas molecules can be used to control the ablation beam kinetic energy that affects the point defect concentration in the film.

Film growth by PLD is achieved within laser-generated plasma. A variety of species in the plume possesses kinetic and potential energies that can increase sticking coefficients, surface mobilities of adatoms, and nucleation due to the high energy chemical reactions. Thus, epitaxial growth of films can be obtained under the appropriate experimental conditions such as substrate temperature, laser energy density, and distance between target and substrate. Also, growth of multilayered epitaxial heterostructures or superlattices in which each layer can be a chemically complex material is possible provided several chemically complex targets with rapid target exchangers are introduced.

Ultraviolet-assisted PLD (UVPLD)

The use of ultraviolet radiation has been explored as a method of providing a more reactive environment thereby enabling lower temperature processing to be used. Kazor *et al.* reported that the radiation from a low pressure mercury lamp enhanced the low temperature oxidation of Si by up to a factor of 50 [Byo93, Kaz92]. They also proposed that the enhanced oxidation was attributed to the formation of oxygen atoms and ozone, which is known to be stronger oxidizing agent than molecular oxygen, by the photodissociation of UV light. By using this beneficial effect of UV radiation *in situ* ultraviolet-assisted pulsed laser deposition (UVPLD) has been used to grow oxide films such as ZnO and Y_2O_3 [Cra99a, Cra99b]. ZnO films grown using UVPLD showed high-quality epitaxial at moderate temperature and the characteristics of ZnO films by UVPLD at 550°C was similar to those for ZnO films by conventional PLD at 750°C [Cra99a]. UVPLD grown Y_2O_3 films were more crystalline than PLD grown films at the same substrate temperatures [Cra99b]. Also, the films by UVPLD showed a highly texturing along (111) orientation, which was appeared only at higher substrates temperature for PLD grown films. Figure 2-10 shows the XPS high resolution spectra of O 1s region from the Y_2O_3 films grown by UVPLD (a) and PLD (b) [Cra99b]. The O 1s peaks were deconvoluted into two sub-peaks at 529 eV and 531.3 eV, corresponding to oxygen atoms bound to yttrium atoms and physisorbed oxygen, respectively [Dur90, Ing96]. The amount of physisorbed oxygen in the films by UVPLD was less than that in the films by PLD. They concluded that Y_2O_3 films grown by UVPLD had a better overall stoichiometry containing less physisobed oxygen and were more stable. Finally, they claimed that the quality of the films by UVPLD was similar to that of films by PLD at substrate temperatures at least 200°C higher.

The UV radiation in the PLD system can dissociate molecular oxygen and form ozone and atomic oxygen, which serve as more reactive gaseous species. It is therefore expected that using in-situ UV source capable of dissociating oxygen molecules during the PLD process, an even more significant improvement in the quality of the grown layers, especially at low substrate temperatures, could be achieved. It is known that there is typically an oxygen deficiency in the films with respect to the targets even though PLD is an excellent technique for the stoichiometric transfer of the target material to the growing film. Thus, the effort for creating more reactive oxygen species using in-situ UV radiation would be more effective to reduce oxygen vacancies.

Electrochemical Characterizations

Cyclic voltammetry (CV)

Cyclic voltammetry is the most frequently used technique for acquiring qualitative information on electrochemical reactions. Essentially, the technique measures current resulting from a linearly changing voltage at given rate. The power of cyclic voltammetry results from its capability of providing considerable information on the thermodynamics of redox process, kinetics of heterogeneous electron transfer reaction, and coupled chemical reactions. Especially it offers a rapid location of redox potentials of the electroactive species and convenient evaluation of the effect of media upon the redox process.

For a reversible reduction (forward direction) of an oxidized species O,

$$O + ne^- \leftrightarrow R \tag{2.23}$$

As the applied voltage approaches to the reversible potential for the electrode process, a small cathodic current flows and increases rapidly but later becomes limited at a potential slightly beyond the standard potential by the subsequent depletion of reactants. As the rate of diffusive transport of reactants at the electrode surface is reduced, the observed current decrease. After traversing the potential region in which the reduction process takes place, the direction of the potential sweep is reversed. During the reverse scan, the reduced species R are reoxidized back to O and an anode peaks results.

The cyclic voltammetry is characterized by two current peaks (i_p) and two potential peaks (E_p). A reversible, diffusion-controlled reaction such as represented by Equation (2.24) exhibits an approximately symmetrical pair of current peaks, as shown in Figure 2-11 (a) [Bro02]. The current peak for a reversible process is given by the Randles-Sevcik equation [Ran48, Sev48]:

$$I_p = (2.69 \times 10^5)\, n^{3/2} A C D^{1/2}\, v^{1/2} \tag{2.24}$$

where n is the number of electrons transferred in the reaction, A is the area of the electrode in cm^2, C is the concentration in mol/cm^3, D is the diffusion coefficient in cm^2/s, and v is the sweep rate of the potential in V/s. The separation between the anodic and cathodic potential peaks is given by

$$\Delta E_p = \frac{2.3\,RT}{nF} \tag{2.25}$$

Thus, the peak separation can be used to determine the number of electrons transferred and as a criterion for a Nernstian behavior. Both the cathodic and anodic potential peaks are independent of the voltage sweep rate.

For irreversible processes in which the rate of transfer of electrons is very slow, a single peak is produced as shown in Figure 2-11 (b). The potential peak is shifted with the voltage sweep rate and in case of irreversible charge-transfer process for which the back reaction is negligible.

For quasi-reversible processes, the current is controlled by both the charge transfer and mass transport. The potential peak is dependent on the voltage sweep rate and the separation in potential peaks is much greater than that given by Equation (2.25). Overall, the voltammogram of a quasi-reversible process is more drawn out as shown in Figure 2-11 (c).

Chronopotentiometry

Chronopotentiometry is a study of voltage transients at an electrode upon which is imposed a constant current. In this technique, a constant current is applied to an electrode, and its voltage response represents the change in electrode processes occurring at the interface. For an electron transfer reaction (reduction) as represented by Equation (2.23), the concentration of oxidized species O at the electrode surface is the same in the bulk solution. Once the constant reducing current has been applied, O is reduced to reduced species R at the electrode surface in order to support the applied current, and the concentration of O in the vicinity of the electrode surface therefore begins to decrease. This sets up a concentration gradient for O between the bulk solution and the electrode surface, and the molecules of O diffuse down the concentration gradient to the electrode surface. The potential is close to the redox potential for $O + ne^- \leftrightarrow R$, and its precise value is dependent on the Nernst equation from which the potential is a function of the surface concentration of O and R. Since these concentrations vary with time, the potential also varies with time, which is reflected in slope of the potential vs. time plot as shown in Figure 2-12 [Bar01]. Once the surface concentration of O falls to zero, the applied current can no longer be supported by this electron transfer reaction, so the potential abruptly changes to the redox potential of another electron transfer reaction. The time required for the concentration of O at the electrode surface to reach to zero is called the transition time τ. The transition time for electroreduction of a species in the presence of excess supporting electrolyte was quantified by Sand [Sad01].

$$\tau^{1/2} = \frac{\pi^{1/2} nFACD^{1/2}}{2i} \tag{2.26}$$

where A is the electrode surface area, C is the bulk concentration of species O, and D is its diffusion coefficient. For a battery application, cyclic chronopotentiometry in which the current can be continuously reversed at each transition is widely used to determine the capacity of both charge and discharge reaction.

Alternative current impedance (ACI)

AC Impedance (ACI) spectroscopy has been widely used to determine several electrochemical parameters required to understand the electrochemical reactions at the interface between the electrode and electrolyte.

Any electrochemical cell can be represented in terms of an equivalent electrical circuit that comprises a combination of resistance and capacitance. This circuit contains at least three components, which are the electrical double layer capacitance (C_d), impedance of the faradic process (Z_f) and the electrolyte resistance (R_Ω). Equivalent electrical circuit of an electrochemical cell, called the Randles circuit, for a simple electrode process is shown in Figure 2-13 [Bre93]. The impedance (Z_f) can be subdivided into the charge transfer resistance (R_{ct}) and the Warburg impedance (Z_w), which measures the difficulty of mass transport of the electroactive species. In real electrochemical systems the experimental impedance includes contributions from C_d and R_Ω as well as Z_f. Since the measure total impedance of the cell (Z) contains the real (Z') and imaginary

(Z'') components, the complex plane plot known as a Nyquist plot has been effectively used to represents the impedance of a cell. A typical Nyquist plot for an electrochemical system is shown in Figure 2-14 in which regions of mass transfer and kinetic control are found at low and high frequencies, respectively [Bre93]. The low frequency (ω) limit is a straight line of unit slope corresponding to a reaction controlled by sole by diffusion and the impedance is the Warburg impedance. At high frequency limit, the control is purely kinetic and the Warburg impedance is negligible due to the very large R_{ct}. This region can be expressed in the equation of a circle radius $R_{ct}/2$ with intercepts on the Z' axis of R_Ω ($\omega \rightarrow \infty$) and of $R_\Omega + R_{ct}$ ($\omega \rightarrow \infty$).

$$\left(Z' - R_\Omega - \frac{R_{ct}}{2}\right)^2 + (Z'')^2 = \left(\frac{R_{ct}}{2}\right)^2 \tag{2.27}$$

Figure 2-14 shows the semi-circle, the straight line, and a transition region between the two. For different system, it can happen that only the semi-circle or only the straight line is observed because of the relative values of the components R_{ct}, Z_w, and C_d. When an electrode process involves several steps, sometimes a succession of semi-circle side by side is obtained, corresponding to RC parallel combination in series and different time constants, from which it is possible to deduce the corresponding parameters.

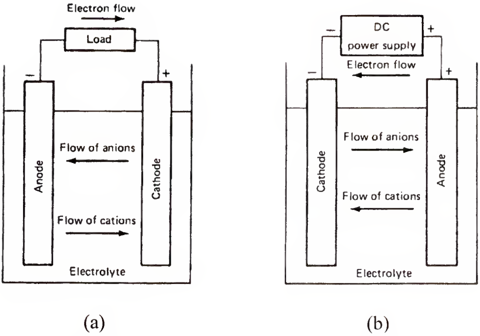

Figure 2-1. Electrochemical operation of a cell: (a) Discharge and (b) Charge [Lin02].

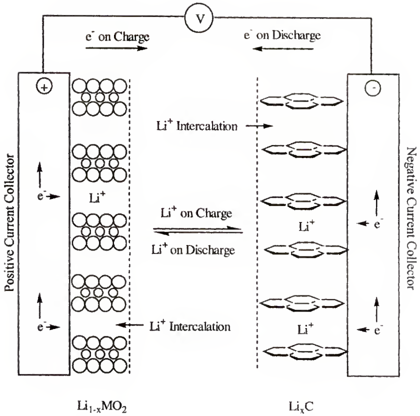

Figure2-2. Schematic of the electrochemical process in a Li-ion battery [Ehr02].

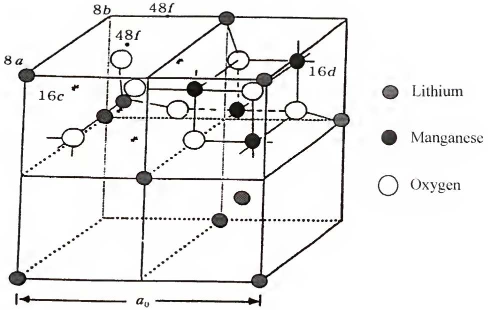

Figure 2-3. Schematic of a unit cell structure of the spinel $LiMn_2O_4$ [Goo98].

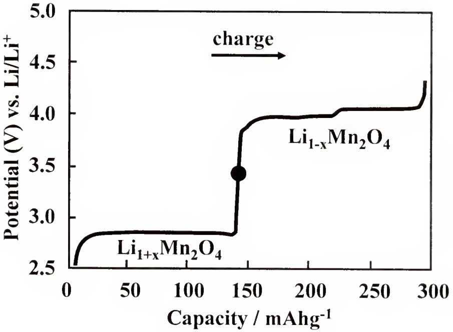

Figure 2-4. Variation of voltage as a function of x in $Li_{1+x}Mn_2O_4$ and $Li_{1-x}Mn_2O_4$ in $Li/LiMn_2O_4$ cell [Goo02].

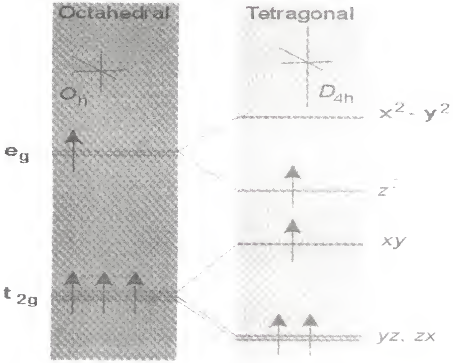

Figure 2-5. Jahn-Teller distortion of the d^4 electron configuration for $LiMn_2O_4$ [BjÖ02].

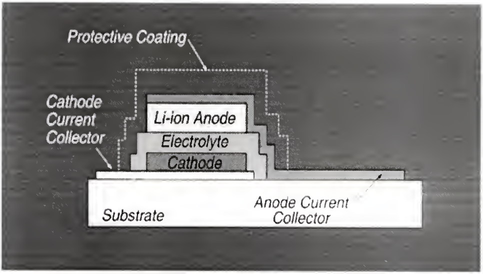

Figure 2-6. Schematic cross section of a thin film Li-ion battery [TFB01].

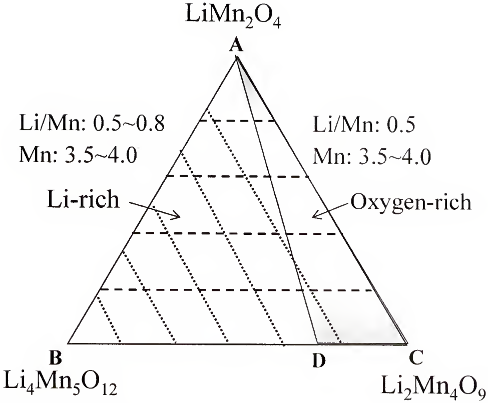

Figure 2-7. Li-Mn-O spinel phase diagram [Xia97b].

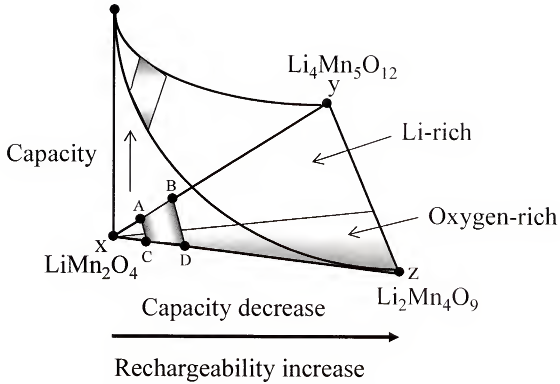

Figure 2-8. Three-dimensional diagram of capacity-rechargeability-chemical composition for each compound on the $LiMn_2O_4$-$Li_4Mn_5O_{12}$-$Li_2Mn_4O_9$ plane [Xia97b].

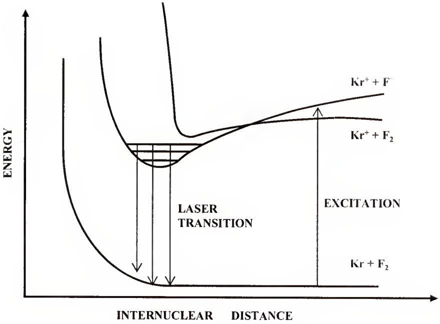

Figure 2-9. Electronic states in excimer emission [Dul96].

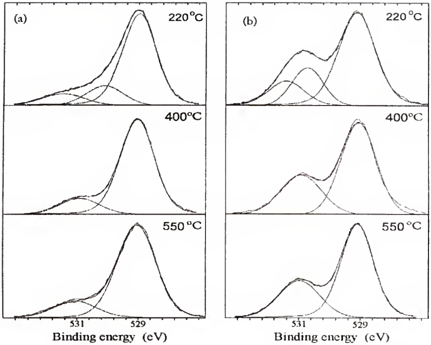

Figure 2-10. XPS high resolution of O 1s region acquired from Y_2O_3 thin film: (a) UVPLD and (b) PLD at different temperature [Cra99b].

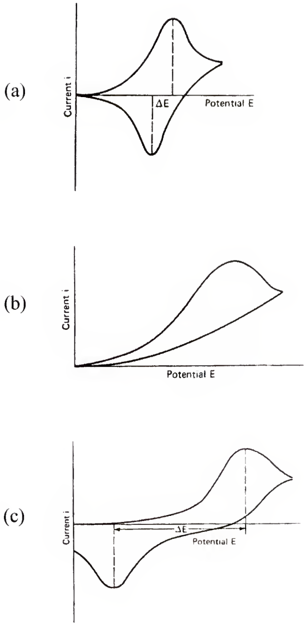

Figure 2-11. Cyclic voltammograms of (a) reversible process, (b) irreversible process, and (c) quasi-reversible process [Bro02].

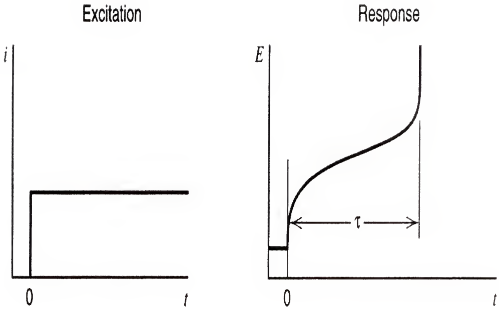

Figure 2-12. Constant current chronopotentiometry [Bar01].

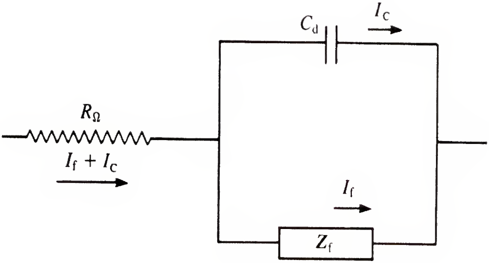

Figure 2-13. Equivalent electrical circuit of an electrochemical cell for a simple electrode process [Bre93].

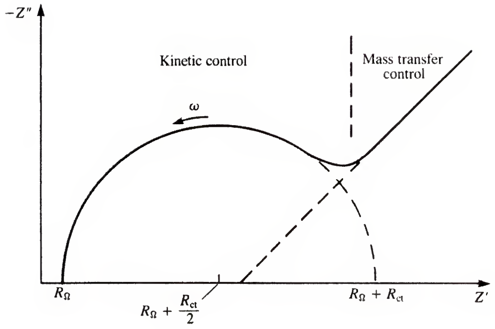

Figure 2-14. A typical Nyquist plot of a simple electrochemical process [Bre93].

CHAPTER 3
EXPERIMENTAL PROCEDURE

Synthesis of Thin Film Cathodes

Target Preparation

Spinel $LiMn_2O_4$ power was obtained by the solid-state reaction. A mixture of lithium carbonate (Li_2CO_3, Alfa Aesar, 99.999%) and manganese dioxide (MnO_2, Alfa Aesar, 99.9%) with a 1:4 molar ratio was immersed in acetone and ball-milled with zirconia media for 1 day. The suspension was dried at 80°C for 24 hours and sintered at 800°C for 12 hours in air. The heating and cooling rates were 10°C/min. The powder was grinded well in the mortar. The as-prepared $LiMn_2O_4$ powder of 10 g was first uniaxially pressed with a pressure of 5000 psi resulting in a disk with diameter of 1.25 inch and thickness of 0.25 inch. This fragile pellet was isostatically pressed with 150 MPa for 10 min. The pressed pellet was sintered at 800°C for 24 hours in air. The heating and cooling rates were 10°C/min.

$LiAl_xMn_{2-x}O_4$ (x= 0.1, 0.2, 0.3) powder was synthesized by the melt-impregnation method [Lee01]. A mixture of Li_2CO_3, MnO_2, and $Al(NO_3)_3 \cdot 9H_2O$ (Alfa Aesar, 99.999%) with appropriate ratios was immersed in acetone and ball-milled with zirconia media for 1 day. The suspension was dried at 80°C for 24 hours and calcinated at 540°C for 5 hours and sintered at 800°C for 12 hours in air. The heating and cooling rates were 10°C/min. The method of fabrication of targets was the same as that for the $LiMn_2O_4$ target.

Thin Film Deposition Process

A Lambda Physik LPX 305 i KrF excimer laser was used for all laser ablation portions of the experimentation. The pulsed 248 nm UV radiation generated by KrF excimer laser was directed through an aperture and a couple of lenses until it finally impinged on the target. The laser beam was first filtered by a 1 x 2 cm aperture and traversed a collimation lens in order to keep the radiation from diverging due to the scattering as it passed through the ambient air. Immediately after the collimating lens, the beam was focused by a focal lens with a focal length of 25 cm. Finally, the focused laser beam impinged a target inside vacuum chamber through the UV transmitted glass. All samples were grown in this laser and optical setup.

A base pressure of a vacuum chamber ranging from 4×10^{-6} to 1×10^{-5} torr was obtained with the help of a turbomolecular pump (Pfeiffer TMU 170). Once the pressure was reached at the base value the substrate was heated at a given ramp rate in the range of $5 \sim 8^{\circ}$C/min. The substrate temperature was varied from 300 to 700°C. The target was rotated at a rate of $10 \sim 15$ rpm to avoid damaging the target. The energy used was 500 mJ corresponding to the energy density of 1.5 J/cm^2 with the given beam size on the target. The pulse repetition rate was 5 Hz and the distance between substrate and target was constant at 4 cm. Stainless steel mesh (Spectrum Co, 30% open area) and silicon wafer were used as the substrates for electrochemical and other characterizations, respectively. Thin films were grown in the oxygen atmosphere of pressure of 500 mtorr. For an ultraviolet–assisted PLD (UVPLD) a couple of low pressure Hg lamps have been added to the conventional PLD setup to convert it into a UVPLD apparatus as shown in

Figure 3-1. The thickness of films grown in this experiment was measured using α-step profilometer.

Characterizations of Thin Film Cathodes

X-ray Diffraction (XRD)

X-ray diffractometer (Philips APD 3720) was used to analyze structural change and crystalline phases of thin film cathodes. The diffracted beams from the crystalline phases that satisfy the Bragg's law were measured as a function of the diffraction angle and the specimen's orientations. X-ray diffraction data were obtained at 40 kV and 20 mA using CuK_α ($\lambda = 1.54$ Å) radiation in $2\theta/\theta$ mode. X-ray continuous scan was performed in the range of 10° to 70° with a step size of 0.03° and 1 second integration time per step.

Scanning Electron Microscopy (SEM)

SEM (JOEL 6335F) was used to examine the surface morphology of the thin film cathodes. A conductive carbon coating was applied on the thin films to decrease the surface charging for better images. SEM was operated at 15 to 20 kV with working distance of 15 mm. A focused electron beam was scanned over the specimen and resulting secondary electrons were detected in terms of the contrast due to the dependence of the electron yield on the topography. The magnification of images obtained from thin films was about ×10000 through ×30000.

X-ray Photoelectron Spectroscopy (XPS)

XPS (Perkin-Elmer PHI 5100 ESCA) was used to obtain elemental compositional details from the surface of thin film cathodes. This technique is clearly one of the most broadly applicable general surface analysis techniques due to its high surface sensitivity and quantitative chemical state analysis capabilities. In the XPS process, high energy photons (X-ray) can ionize atoms to produce free electrons known as photoelectrons. The kinetic energy (*KE*) of the electron depends on the energy of the photon by Einstein's photoelectric law:

$$KE = h\upsilon - BE \tag{3-1}$$

where hυ is the energy of the incident photon and *BE* is the binding energy. In this equation, hυ is known, *KE* is measured, and *BE* is therefore the determined output.

X-ray source was monochromatized Mg K_α with energy of 1253.6 eV. Survey scans were performed with an analyzer pass energy 89.45 eV and binding energy range from 0 to 1000 eV. High resolution scans (multiplex) were conducted at each element such as C 1s, O 1s, and Mn 2p for $LiMn_2O_4$ films and Al 2p as well for Al doped films. All measurements were conducted before and after sputtering with Ag ion gun for 5 min. The binding energy was calibrated using a reference binding energy of C 1s peak at 284.6 eV. The relative atomic concentration of each element in the films was determined with sensitivity factors for integrated peak area.

Transmission Electron Microscopy (TEM)

TEM (JOEL 200CX) was used to study the crystal structure and orientation of the thin film cathodes. TEM was operated with voltage at 200 kV ($\lambda = 0.00251$ nm). Films grown on silicon wafer were prepared by mechanical grinding, polishing, and grinding followed by Ar ion milling using ion miller (Gatan 600).

Electrochemical Measurements

The electrochemical measurements were conducted inside glove box filled with argon as an inert gas. The oxygen and moisture inside box was thoroughly controlled to maintain the values below a few ppm. The electrochemical cell was composed of a working electrode (thin film cathode), a counter electrode, and a reference electrode, both of which were Li metals. The electrolyte consisted of 1 M $LiPF_6$ in the solution of mixture of ethylene carbonate and dimethyl carbonate (1:1 volume ratio). A schematic of the electrochemical cell used is shown in Figure 3-2. A thin film cathode was put in the bottom of the assembly and then a separator was inserted on the top of cathode. A few drops of electrolyte were added on the separator and Li anode was brought on it. Four screws were tightened to seal the whole assembly. Electrochemical workstation (CHI 600) was used to conduct the electrochemical measurements such as cyclic voltammetry, chronopotentiometry, and AC impedance.

Once a cell was assembled, the electrochemical measurement was initiated after 1 hr for the stabilization. At first the alternative current impedance (ACI) was measured at the open circuit voltage (OCV) with voltage amplitude of 5 mV in the frequency range of 1 to 10^5 Hz. Then the cyclic voltammetries (CVs) at various scan rates ranging of 0.1 ~ 1.6 mV/s were measured between 2.5 ~ 3.5 V for 3 V measurement (2.5 ~ 4.5 V for both 3 and 4 V measurements). The reversibility and capacity in the voltage range was determined from the CV date. In addition, the diffusion coefficients of lithium ions in both oxidation (charge) and reduction (discharge) were determined by the CV. The cycle measurement was performed with the chronopotentiometry in the rage of 2.5 ~ 3.5 V for 3 V (2.5 ~ 4.5 V for both 3 and 4 V) at the rate of 1 C for both charge and discharge. The 1 C rate was estimated by the thickness and area of the cathode films with the assumed capacity and density that were 120 mAh/g and 4.2 g/cm^3, respectively. The first cycle was initiated after the cell was discharged to the 2.5 V for 3 V measurement. ACI was measured after 50th cycle to compare it with the previous one. The resistance and capacitance related to the cell was determined from the ACI data through the corresponding equivalent circuits. After 50th cycle, the cell was cycled at different discharge rates corresponding to 3, 5, 7, and 10 C rates to determine the rate capability of the cell. Further cycling behaviors of the cells have measured for next 50 or 150 cycles.

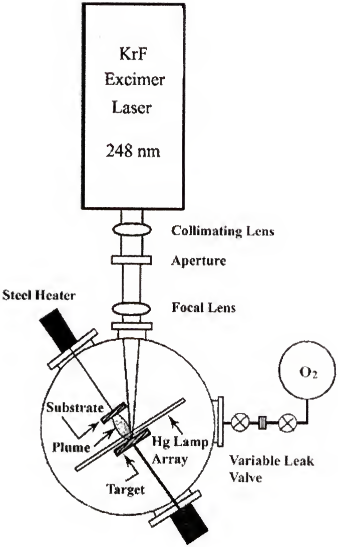

Figure 3-1. Schematic of UVPLD system.

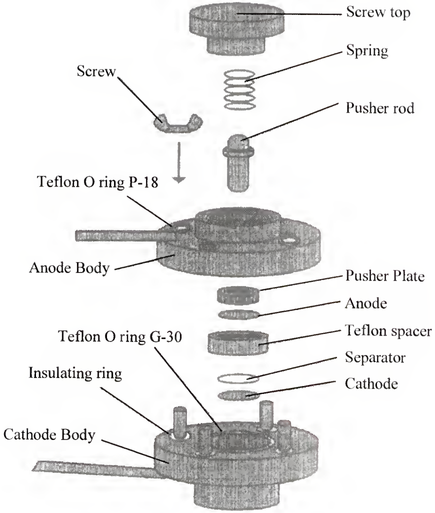

Figure 3-2. Schematic of the electrochemical cell used.

CHAPTER 4
EFFECT OF TEMPERATURE ON THE ELECTROCHEMICAL CHARACTERISTICS OF LITHIUM MANGANESE OXIDE THIN FILM CATHODES

Introduction

Crystallinity, microstructure, and composition of the lithium manganese oxide play a critical role in the electrochemical properties of the Li-ion battery systems. One of the factors that affect the crystallinity and microstructure of the thin-film is a temperature at which the thin-films are grown and/or annealed. In the viewpoint of capacity fade on cycling due to the dissolution of Mn, the surface area of the active electrode material contacted with the electrolyte should be minimized to reduce the amount of dissolved Mn. However, the larger surface area (small grain size) is preferred for the high capacity and fast rate capability related to the diffusion (and/or transport) of lithium ions in the electrolyte, at the surface, and in the electrode. In addition, crystallinity is of important effect on the diffusion of Li^+ and strains generated on cycling. Thus, in this chapter we examined the effect of temperature at which the thin films were grown on the electrochemical properties of lithium manganese oxide cathodes.

Experimental

Various substrate temperatures ranging from 300°C to 700°C were applied to grow $LiMn_2O_4$ thin films in order to determine an optimum growth temperature of the cathodes for the best electrochemical properties. The conventional PLD technique was utilized to grow $LiMn_2O_4$ thin films in the vacuum chamber filled with oxygen gas of 500 mtorr. There were two substrates used in this experiment; one was Si wafer with (100) for the thickness measurement and structural characterizations, and the other was stainless steel mesh (Spectrum Lab. Co.) with 30% of open area for the electrochemical measurements. Thickness of the films grown in this experiment was measured to be 5000 ~ 6000 Å in α-step surface profilometer. Structural characterization techniques such as XRD, SEM, XPS, and TEM were performed to analyze the characteristics of the thin film cathode.

In order to investigate the effect of substrate temperature of growing $LiMn_2O_4$ films on the electrochemical properties, the 3 V region in the range of 2.5 ~ 3.5 V and 3 and 4 V region in the range of 2.5 ~ 4.5 V have been used. After assembling the cell with Li metal as an anode and a reference electrode in Ar filled glove box, the cell was relaxed for 1 hour and stabilized to reach its equilibrium state. Firstly AC impedance was measured with an open-circuit voltage of the cell with given frequency range and amplitude. In this AC impedance measurement, 5 mV and $1 \sim 10^5$ Hz were used as the amplitude and frequency range, respectively. Cyclic voltammograms were measured at sweep rates of 0.1, 0.4, 0.9, and 1.6 mV/s for 3 V region with an initial cathodic scan and 3 and 4 V regions with an initial anodic scan. The charge/discharge process (chronopotentiometry) was followed in the range of 2.5 ~ 3.5 V and 2.5 ~ 4.5 V for 3 V and 3 and 4 V regions, respectively. Continuous charge/discharge cycling was conducted at current density of 1 C rate, which is different from one another for all cathode films in terms of the measured thickness. In 3 V region 50.4 $\mu Ah/cm^2 \cdot \mu m$ was used the 1 C rate based on the fact that 4.2 g/cm^3 (95% of reported value) and 120 mAh/g (81% of theoretical discharge capacity) were assumed as the density and discharge capacity of $LiMn_2O_4$ thin film. The doubled 1 C rate was used for the 3 and 4 V regions. Just after 50th cycle, various current densities have been applied to charge/discharge cell to study the rate capability of the thin film cathode. The current density of 3, 5, 7, and 10 C rates has been chosen to conduct for the rate capability study. After 50th and 100th cycle, AC impedance was again measured with an open-circuit voltage of the cell.

Results and Discussion

Structural Characterizations

Figure 4-1 shows the X-ray diffraction of $LiMn_2O_4$ films grown on stainless steel mesh at different substrate temperatures with oxygen atmosphere of 500 mtorr. Even though the diffraction peaks were very wide and exhibited low intensity for the films grown at low temperature, all reflections can be assigned to the Bragg positions for the $LiMn_2O_4$ spinel phase. Especially, the peaks from the films grown at higher than 600°C were clearly identified as the cubic spinel phase having a space group $Fd\bar{3}m$. The letter S in Figure 4-1 represents the stainless steel substrate used. The height and width of each peak became taller and narrower with increasing substrate temperature, indicating that the crystallinity and grain size of the films were increased with increasing temperature. For example, the full width half maximum (FWHM) of (111) peak from the film grown at 300°C was measured to be 0.72° while that of the same peak from the film grown at 700°C was measured to be 0.18°. The broadening of diffraction peaks at high scattering angles for the films grown at lower temperatures may be indicative of the residual strain in the structure caused by inhomogeneities, cation or anion non-stoichiometry, and grain boundary effect [Pat92].

Figure 4-2 shows that the lattice constants were increased with increasing substrate temperature from 8.156 Å to 8.229 Å for the film grown at 300°C and 700°C, respectively. The increase in lattice constant of $LiMn_2O_4$ with temperature is in agreement with the previous literatures [Chu01, Nag00]. The lattice constant of the film grown at 700°C was slightly smaller than 8.247 Å, which has been reported as a lattice constant of cubic spinel $LiMn_2O_4$ [Cho99]. As mentioned in the chapter 2, in $LiMn_2O_4$ Mn^{3+} and Mn^{4+} occupy the half of total 32 octahedral sites in the spinel. The ionic radius of Mn is dependent on the oxidation state of manganese ion. The ionic radius of Mn^{4+} is 0.53 Å whereas that of Mn^{3+} is 0.58 Å in the low spin state and 0.645 Å in high spin state [Sha69]. The increase of the lattice constant with temperature can be ascribed to the transition of manganese ion from Mn^{4+} to Mn^{3+} in the high spin state. Chung *et al.* confirmed that the oxidation state of transition Mn ion was changed with temperature showing the increase of the amount of Mn^{3+} in high spin state with temperature [Chu01]. Also Figure 4-2 shows the FWHM of (111) from films grown at different substrate temperatures was decreased with increasing temperature indicating the increase of crystallinity with temperature.

Figure 4-3 shows the SEM micrographs of pulsed laser deposited $LiMn_2O_4$ films grown onto stainless steel mesh in oxygen partial pressure $P(O_2)$= 500 mtorr at (a) 400°C, (b) 500°C, and (c) 700°C. The film grown at 400°C has a relatively smooth and dense surface with small grains of fairly homogenous size in the range of 100 nm in length and 50 nm in width (Figure 4-3 (a)). SEM revealed that the grain size of the films was increased with increasing substrate temperature. Figure 4-3 (c) shows several agglomerated grains with size of 450-500 nm in the film grown at 700°C due to the grain growth at high temperature.

TEM was used to confirm the crystal structure of the films as shown in Figure 4-4 for the $LiMn_2O_4$ film grown at 500°C. The bright field image of the film is almost identical to the morphology observed by SEM in which there are elongated grains in size of 80 ~ 150 nm. Selected area electron diffraction was included in the Figure 4-4 (a) showing that a typical ring pattern, which was identified as a randomly oriented polycrystalline $LiMn_2O_4$. Energy Dispersive X-ray Spectroscopy (EDX) of the films also is shown in Figure 4-4 (b). The characteristic X-rays of manganese and oxygen accompanied with carbon and silicon from wafer are shown on the spectrum. It is worthy noting that there was no Li characteristic X-ray due to the detection limit.

XPS was conducted to study the chemical composition and bonding nature of the lithium manganese oxide films. A typical XPS spectrum from a $LiMn_2O_4$ film grown at 300°C is shown in Figure 4-5. The peak of Li 1s core level has a binding energy of 53.5 eV while the peak of O 1s core level has a binding energy of 530.4 eV. The separation between Mn $2p_{3/2}$ and Mn $2p_{1/2}$ was 11.6 eV which is in a good agreement with the literature values [Chi99, Mou92]. The high resolution of each peak was used to determine the relative composition of constituents. However, it should be noted that the composition of Li in the films was not obtained because the overlapping of Li 1s peak with Mn 3p peak, which is located at 49.5 eV, might lead to considerable error in lithium composition determination. Figure 4-6 shows the high resolution of Mn 2p peaks of lithium manganese oxide films grown at 300°C, 500°C, and 700°C. The Mn $2p_{3/2}$ peak was deconvoluted with three Gaussian peaks, which are shown as letter A, B, and C in Figure 4-6. The peaks at 641 ~ 641.3 eV and 642.2 ~ 642.8 eV can be assigned to Mn^{3+} and Mn^{4+}, respectively [DiC89, Eri02]. The peaks at 644.4 ~ 645 eV may represent either a higher oxidation state of manganese or peak related to impurities. By comparing the ratio of Mn^{3+} to Mn^{4+}, the average oxidation state of Mn was determined. As the substrate temperature was increased the amount of Mn^{3+} was also increased, which is in a good accordance with the results obtained in the lattice constant measurement. The calculated average oxidation state of manganese in the films was decreased with increasing temperature from 3.523 ± 0.015 to 3.495 ± 0.023. Also, the relative atomic ratio of O/Mn was decreased with increasing temperature. The high value of O/Mn for film grown at low temperature may result from the phase with oxygen rich ($LiMn_2O_{4+\delta}$) and/or cation deficiency ($Li_{1-\delta}Mn_{2-2\delta}O_4$) of which the oxidation state of Mn would be larger than +3.5 of a stoichiometric spinel $LiMn_2O_4$. The loss of oxygen in the films grown at high temperature has been reported by other research groups [Liu97, Mor98, Sin02].

Electrochemical Characteristics

Cyclic voltammetry of 2.5 ~ 3.5 V region

Cyclic voltammetry can yield thermodynamics as well as kinetic information. Figure 4-7 (a) displays cyclic voltammogram for 0.6 μm $LiMn_2O_4$ thin film grown at 300°C in 500 mtorr of oxygen between 2.5 and 3.5 V at various sweep rates of 0.1 ~ 1.6 mV/s. The 3 V process is characterized by a peak at 2.8 V on discharge and a peak at 3.1 V on charge. The peak on discharge corresponds to the intercalation of lithium into $LiMn_2O_4$ to become $Li_2Mn_2O_2$ with a reduction of the average oxidation state of manganese. When lithium is inserted into the spinel $LiMn_2O_4$ to form $Li_2Mn_2O_4$, it causes a first order transition to a rock salt phase $Li_2Mn_2O_4$ during which the tetrahedrally (8a) coordinated lithium ions are cooperatively displaced into the octahedral sites (16c). The peak on charge is related to the $Li_2Mn_2O_4 \rightarrow LiMn_2O_4$ reaction during which the lithium is extracted from the octahedral sites of the rock salt phase to leave a spinel phase.

The shape of the voltammogram is strongly dependent upon the sweep rate. An increase in sweep rate is correlated with a progressive shift of the anodic peaks to higher potential as well as increase in height. On the contrary, the cathodic peaks are shifted to lower potential and their height is increased as the sweep rate is increased. It also should be noted that the separation (ΔE_p) between anodic (E_{pa}) and cathodic potential peak (E_{pc}) becomes wider with increasing the sweep rate, indicating that the reversibility of the charge/discharge reaction is decreased. The data are presented as psudocapacitances, i.e., current density divided by sweep rate, to more clearly indicate the change in shape with sweep rate in Figure 4-7 (b). The lithium intercalation/deintercalation process is slowed down as the sweep rate gets higher because only surface film participates for high sweep rates whereas a low sweep rate permits cycling in the bulk of the film. It is evident that the highest psudocapacitance was obtained at the lowest sweep rate as shown in Figure 4-7 (b).

Figure 4-8 shows the cyclic voltammograms obtained from the $LiMn_2O_4$ thin films grown at 300 ~ 700°C in 500 mtorr of oxygen between 2.5 and 3.5 V at sweep rates of 0.1 mV/s. Of important features from the CVs are the current peaks (I_{pa} & I_{pc}) and the separation (ΔE_p) between potential peaks (E_{pa} & E_{pc}) on both charge and discharge. Both anodic and cathodic current peaks were increased with increasing temperature up to 500°C and then significantly decreased at higher temperatures. Even though the integrated capacity from the area below the current peak can be estimated, it is not reasonable to compare the relative capacities of all thin film cathodes from only these cyclic voltammograms due to the difference in amount of involved active material.

Anodic potential peaks were slightly shifted to the higher potential as the substrate temperature was increased from 300˚C to 500˚C. Then those of films grown at 600˚C and 700˚C were significantly moved toward higher potential. For cathodic potential peaks the same shift behavior as anodic peaks was taken place but to the lower potential. Accordingly, the separation between anodic and cathodic potential peak became wider as the substrate temperature was increased. The potential separation between anodic and cathodic peaks is theoretically 59/n mV where n is the number of electrons transferred for an ideally reversible reaction in which the electron transfer is relatively fast compared to that of mass transport. The potential peak separation of all samples shown in Figure 4-8 was larger than the theoretical value and increased with increasing temperature. For example, the potential peak separations measured at sweep rate of 0.1 mV/s were 152 mV and 609 mV for the cell with thin film cathode grown at 300˚C and 700˚C, respectively. Since larger separation between two potential peaks is an indication of a nonreversible reaction, the cell with $LiMn_2O_4$ thin film cathode grown at 700˚C showed the least reversible electrochemical reaction among the cells with thin film cathodes grown. Also, it is reasonable to note that the charge transfer occurring at the surface of thin film cathode becomes slow and a predominant step, which determines the rate of whole reaction, for the thin film cathode grown at high temperature especially at 600˚C and 700˚C. The amount of electrons transferred on the thin film cathode grown at higher temperature might be significantly low compared to that of the thin film cathode grown at lower temperature because of the slow charge transfer rate. The measured resistance to the charge transfer at the interface between the thin film cathode and the electrolyte is shown and discussed in the following section in which the alternative current (AC) impedances are represented.

One of the advantages in the study of cyclic voltammetry is the ability to measure the diffusion coefficient of electrochemically active species. In this study, the cyclic voltammetry technique was used to determine the diffusion coefficient of lithium in the Li-Mn-O thin film cathodes. For a reversible system, the current peak is defined by the Randles-Sevcik equation [Ran48, Sev48]:

$$I_p = (2.69 \times 10^5)\, n^{3/2} A C D^{1/2}\, v^{1/2} \tag{4.1}$$

where n is the number of electrons transferred in the reaction, A is the area of the electrode in cm^2, C is the concentration in mol/cm^3, D is the diffusion coefficient in cm^2/s, and v is the sweep rate of the potential in V/s. According to the Randles-Sevcik equation, I_p is proportional to $v^{1/2}$ and a plot of I_p versus $v^{1/2}$ should be a straight line for a reversible system. The slope of the I_p versus $v^{1/2}$ was used to calculate the diffusion coefficient of lithium during the charge and discharge and the results are shown in Figure 4-9 and Table 4-1. The results show that the diffusion coefficient of lithium was increased with increasing substrate temperature from 300°C to 500°C and then decreased at higher temperatures. The values were varied from 2.286×10^{-11} cm^2/s for the film grown at 700°C to 3.033×10^{-9} cm^2/s for the film grown at 500°C. The reported values of diffusion coefficient of Li for $LiMn_2O_4$ in the literatures range from 3.1×10^{-11} cm^2/s to 5×10^{-10} cm^2/s for bulk and 2.5×10^{-11} cm^2/s to 3×10^{-10} cm^2/s for thin films [Guy94, Pis92, Rou97, Str96].

Table 4-1. Parameters measured from the cyclic voltammograms.

Temperature	300°C	400°C	500°C	600°C	700°C
ΔE_P (V) at 0.0001 V/s	0.152	0.177	0.197	0.490	0.609
D_{ch} (cm^2/s)	1.058×10^{-9}	1.059×10^{-9}	3.117×10^{-9}	7.937×10^{-11}	2.172×10^{-11}
D_{disch} (cm^2/s)	7.206×10^{-10}	1.128×10^{-9}	3.033×10^{-9}	5.003×10^{-11}	2.286×10^{-11}

The film grown at 300°C showed the lower diffusion coefficient than those grown at higher temperatures (400 and 500°C) because the poor crystallinity with amorphous phase in part might interrupt the path for the Li diffusion into/from the cathode film. It can also be attributed to the fact that the substrate temperature is not sufficiently high for Li ions to occupy the tetrahedral 8a sites through which Li insertion takes place at 3 V region. The film grown at 700°C had the lowest diffusion coefficient since the agglomerated large grains at the surface of the thin film cathode might only participate in the Li intercalation/deintercalation resulting in slow diffusion. The longer diffusion path due to the grain growth may be ascribed to the extended time for Li to diffuse in and out of the grains. In the case of the $LiMn_2O_4$ thin film cathode grown at 500°C, the aspects that are suspected to restrict the Li diffusion in the films grown at low and high temperatures can be alleviated by having the optimized crystallinity, grain size, and composition, leading to the fast Li diffusion.

Discharge capacity of 2.5 ~ 3.5 V region

Figure 4-10 displays the first discharge curve in the range of 2.5 ~ 3.5 V at 1 C rate of cells with $LiMn_2O_4$ film grown at 300 ~ 700°C in 500 mtorr of oxygen. One of the distinct features from discharge curves is the discharge potential of the each cell. The discharge potential of $LiMn_2O_4$ thin film cathodes grown at 300°C, 400°C, and 500°C was nearly constant at about 2.84 V whereas those for $LiMn_2O_4$ thin film cathodes grown at 600°C and 700°C were much lower than 2.84 V. The potential drop of a cell has been attributed to the overpotential induced by the kinetic limitation and the ohmic drop in the electrolyte. It can be concluded that the voltage drop is mainly ascribed to the radical increase in charge transfer resistance of the films grown at 600°C and 700°C as mentioned in the CV measurements in which the charge transfer resistance were extremely higher than others. The larger the grain size, the higher is the true current density for a given overall current. This might increase most forms of overpotential (polarization) in the charge transfer reaction between the intercalant and intercalation host.

There was a tendency that the initial discharge capacity was increased with increasing substrate temperature from 300°C to 500°C, which exhibited the maximum values among others and then decreased at higher temperature. The cell with $LiMn_2O_4$ thin film cathodes grown at 700°C showed the lowest initial discharge capacity. In $LiMn_2O_4$, the amount of Mn^{3+} has a close relation with the electrochemical properties. During charge and discharge at 3 V, the change of manganese oxidation state occurs as follows:

$$Li^+ + e^- + LiMn^{3+}Mn^{4+}O_4 \leftrightarrow Li_2Mn^{3+}Mn^{3+}O_4 \tag{4.2}$$

Since the discharge capacity of $LiMn_2O_4$ is determined by the amount of Mn^{3+}, the capacity increases with the increase of the amount of Mn^{3+} [Chu01]. It was also reported that lattice constant of $LiMn_2O_4$ is increased with increasing the amount of Mn^{3+} because of the larger Mn^{3+} ionic radius than Mn^{4+}. Thus, it is believed that the discharge capacity of $LiMn_2O_4$ was increased with increasing temperature from 300 to 500°C due to the increased amount of Mn^{3+} with temperature as shown in the lattice constant measurement and XPS results. In addition, the increased crystallinity with temperature may facilitate the intercalation/deintercalation of Li leading to higher capacity. However, $LiMn_2O_4$ thin films grown at 600°C and 700°C showed smaller capacities although they have higher amount of Mn^{3+}. In these films, inhomogeneous distribution of composition and/or agglomerated grain may cause the incomplete electrochemical reaction, leading to a smaller capacity. The high temperature can lead to a higher cell resistance due to the enlarged grains that reduce the contact area between the electrode and electrolyte as well as contact area between grains, resulting in slow electrochemical reaction. Thus, the active material participated in the electrochemical reaction might be limited to only very thin surface area of the thin film. Also, loss of lithium at high temperature due to the high vapor pressure of Li may result in the smaller discharge capacity of grown at 600°C and 700°C [Jul00, Mor98].

Cycling behavior of 2.5 ~ 3.5 V region

Figure 4-11 (a) shows the discharge curves of a Li-ion cell with 0.61 μm thick $LiMn_2O_4$ film grown at 300°C in 500 mtorr of oxygen in the range of 2.5 ~ 3.5 V discharged at 30.8 $\mu A/cm^2$ (1 C rate). The first discharge capacity was about 31.93 $\mu Ah/cm^2 \cdot \mu m$, which is equivalent to about 53.22% of the theoretical value. The discharge capacity was decreased to 78.35% of its initial value after 20 cycles. After 100 cycles, the discharge capacity was decreased to 61.42% of its initial capacity, which corresponds to the 0.3858% reduction in capacity per cycle. Figure 4-11 (b) shows the discharge curves of a Li-ion cell with 0.64 μm thick $LiMn_2O_4$ film grown at 400°C in the range of 2.5 ~ 3.5 V discharged at 32.4 $\mu A/cm^2$ (1 C rate). The first discharge capacity was about 33.48

μAh/cm^2·μm, which is equivalent to about 55.8% of the theoretical value. The discharge capacity was gradually decreased to 85.08% of its initial value after 20 cycles. The discharge capacity after 100th cycle was decreased to 81.95% of its initial capacity, which corresponds to the 0.1805% reduction in capacity per cycle. Figure 4-11 (c) shows the discharge curves of a Li-ion cell with 0.61 μm thick $LiMn_2O_4$ film grown at 500°C in the range of 2.5 ~ 3.5 V discharged at 33.8 μA/cm^2 (1 C rate). The first discharge capacity was about 41.05 μAh/cm^2·μm, which is equivalent to about 68.42% of the theoretical value. The discharge capacity was gradually decreased to 86.41% of its initial value after 20 cycles. After 100th cycle, the discharge capacity was decreased to 75.15% of its initial capacity, which corresponds to the 0.2485% reduction in capacity per cycle. Figure 4-11 (d) shows the discharge curves of a Li-ion cell with 0.52 μm thick $LiMn_2O_4$ film grown at 600°C in the range of 2.5 ~ 3.5 V discharged at 26.2 μA/cm^2 (1 C rate). The first discharge capacity was about 19.93 μAh/cm^2·μm, which is equivalent to about 33.22% of the theoretical value. After10 cycles, the discharge capacity was significantly decreased to 54.81% of its initial capacity. Then, the discharge capacity was gradually decreased to 48.72% of its initial capacity at 100th cycle, which corresponds to the 0.4519% reduction in capacity per cycle. Figure 4-11 (e) shows the discharge curves of a Li-ion cell with 0.51 μm thick $LiMn_2O_4$ film grown at 700°C in the range of 2.5 ~ 3.5 V discharged at 25.7 μA/cm^2 (1 C rate). The first discharge capacity was about 13.95 μAh/cm^2·μm, which is equivalent to about 23.24% of the theoretical value. After 10th cycle, the discharge capacity was severely decreased to 48.72% of its initial capacity. Then, the discharge capacity was gradually decreased to 40.02% of its initial capacity at 100th cycle, which corresponds to the 0.5128% reduction in capacity per cycle. The cycle behaviors and relative capacity of the cell with $LiMn_2O_4$ thin film cathodes grown at 300°C ~ 700°C are shown in Figure 4-12 (a) and (b), respectively.

Several reasons have been proposed to explain the capacity loss in $LiMn_2O_4$. They are: (1) a slow dissolution of the cathode in the charged state is induced by the oxidation of the electrolyte at potential above 4.1 V [Jan96]. This effect is particularly enhanced by the formation of protons during decomposition of solvents such as ethers and the generation of HF from fluorinated salt such as $LiPF_6$ [Jan97]. (2) A slow dissolution in the electrolyte of the cathode in the discharged state takes place according to the disproportionation reaction $2Mn^{3+} \rightarrow Mn^{2+} + Mn^{4+}$. Thackeray *et al.* proposed that this reaction is enhanced by the formation of Li-rich (Mn^{3+} rich) phase at the surface of the electrode [Cho99]. (3) When excess lithium is inserted into the framework during discharge the Jahn-Teller induces a large volume change. These repeated distortions are too severe for the cathode to maintain its structural integrity. This phenomenon is kinetically induced at the surface of the grain where Li-rich phases are formed [Gum94, Tha98]. It is believed that the effect of (1) was minimized because the electrochemical measurements were performed in the range of 2.5 ~ 3.5 V for this 3 V study.

From the cycling behavior of the cells with $LiMn_2O_4$ thin film grown at different temperatures as shown in Figure 4-12 (b), it can be concluded that the capacity retention on cycling was decreased with increasing temperature from 400°C to 700°C except for the case of the cell with thin film cathode grown at 300°C. This tendency was in a good agreement with the previously reported literatures [Liu96, Luc99]. For the thin film cathode grown at 300°C, the small grain of cathode material with a high surface area would be expected to improve the lithium insertion kinetic by reducing the diffusion length within grain. The formation of $Li_2Mn_2O_4$ at the surface of the grain should be then reduced, leading to a lower capacity loss during cycling. However, the capacity retention of $LiMn_2O_4$ film grown at 300°C was inferior to those grown at 400°C and 500°C. This would be consistent with the idea that the dissolution process predominantly governs the capacity loss of $LiMn_2O_4$ film grown at 300°C. $LiMn_2O_4$ is slightly soluble in the electrolyte, hence, a higher surface area would accelerate the dissolution process and induce a faster capacity loss.

As shown in the structural investigation, the content of Mn^{3+} was increased with increasing temperature at which thin film cathodes were grown. The higher content of Mn^{3+}, the more severe Jahn-Teller takes place during cycling because the Li-rich $Li_2Mn_2O_4$ would be more easily formed at the surface of the grain during the discharge. Thus, the cell with cathode film having higher content of Mn^{3+} showed the lower cyclability than the cells having lower content of Mn^{3+}. Especially, for a $LiMn_2O_4$ film grown at 700°C, the loss of oxygen, which was confirmed by XPS, would induce a decrease of oxidation state of Mn and an increase of Mn^{3+} content leading to enhanced the disproportionation reaction and fast capacity loss [Tar94]. When the concentration of Mn^{3+} in the framework drops due to the disproportionation reaction, the dissolution process slows down and capacity retention stabilizes shown in Figure 4-12 (b). One of reasons for the better capacity retention of low-temperature grown cathode film might be the structural factor. The film grown at low temperature may have structural defects, which can offer spaces for a small flexible transition of the lattice during the intercalation/deintercalation process. Thus, the framework may be able to resist the stress, which is generated from repeated cycling leading to a good rechargeability. Also, for a uniform distribution of small grains shown in Figure 4-3 (a) for $LiMn_2O_4$ film grown at 400°C, it is reasonable to assume that all grains have the same composition during discharge. When Jahn-Teller distortion occurs, most grains would experience, to the same extent, the dimensional change caused by a cubic to tetragonal phase transformation. This uniformity of change among all grains might help retain the structural integrity between the grains resulting in the good capacity retention.

AC impedance of 2.5 ~ 3.5 V region

Typical AC impedance spectra at the open-circuit voltage of as-received thin films grown at different temperatures are shown in Figure 4-13 (a). The spectra showed a typical Nyquist plot in which the real and imaginary impedances are drawn as a function of the given frequency. As mentioned in the chapter 2, the semicircle in the high frequency region is due to the charge transfer reaction at the interface of the electrolyte/electrode, and the inclined line in the low frequency region is attributed to Warburg impedance that is associated with lithium diffusion through the electrode [Cho95]. It can be qualitatively concluded that the charge transfer resistance was increased with increasing temperature because the diameter of semicircle in the high frequency region was increased with increasing temperature. Upon repeated cycling, the diameters steadily was increased, indicating that the charge transfer resistance was increased with cycling as shown in Figure 4-13 (b) for the $LiMn_2O_4$ thin film grown at 300°C. For all $LiMn_2O_4$ films grown at 300 ~ 700°C the charge transfer resistance increased with cycling, which could account for most of the high cell polarization that leads to the premature termination of the recharge operation.

In order to estimate the numerical values related to the AC impedance spectra the modified equivalent circuit was used in which the double layer capacitance was replaced with the constant phase element (CPE) shown in Figure 4-14. R_{el} is the electrolyte resistance represented as R_Ω in the chapter 2. The CPE is a non-intuitive circuit element that was discovered in depressed semicircle with the center some distance below the real impedance (Z′) axis. Mathematically, a CPE's impedance is given by

$$1 / Z = Q\,(j\omega)^n \tag{4.3}$$

where Q has the numerical value of the admittance at $\omega = 1$ rad/s. When n=1, Q is the same as capacitance C. The numerical exponent n is defined as $n = 1/(D-1)$ where D is the fractal dimension. For a perfect smooth surface the D is 2 and thus n=1 whereas n=0.5 when D is 3 for a highly contorted surface. For the case of a classical depressed semicircle, the true capacitance C can be calculated by the equation shown below [Hsu01],

$$C = Q\,(\omega_{max})^{n-1} \tag{4.4}$$

The details on fitting of Nyquist plots obtained by the modified equivalent circuit are shown in the Appendix. Calculated values including charge transfer resistance (R_{ct}) and double layer capacitance (C_{dl}) are shown in the Table 4-2 and the change of R_{ct} and C_{dl} with temperature is displayed in Figure 4-15. There was no significant difference in the electrolyte resistance (R_Ω), which was in 5 ~ 15 Ωcm^2 for all films regardless of temperature. R_Ω can be easily determined from the intercept of the semicircle and the abscissa at the high frequency region on the Nyquist plot. One of the important parameters shown in Table 4-2 is the value of the numerical exponent n. The value n of the film grown at 400°C was the highest whereas that of 700°C was the lowest, indicating that the film grown at 400°C has a relatively flat and smooth surface compared to that grown at 700°C. This result agrees well with the morphology observed by SEM shown in Figure 4-3. The double layer capacitance was slightly decreased with increasing temperature up to 500°C and then increased. The charge transfer resistance was increased with increasing temperature as expected from the Nyquist plot shown in Figure 4-13 (a). The increment of R_{ct} with increasing temperature was mainly attributed to the grain growth and agglomeration of grains with temperature. The thin film cathode with smaller grain, thus larger specific surface area contacted with the electrolyte would accommodate more charges at the interface resulting in the lower charge transfer resistance for the thin film cathodes grown at low temperature. The change of R_{ct} with temperature confirmed the result that had been expected from the separation between anodic and cathodic potential peaks in the cyclic voltammetry measurements.

Table 4-2. Parameters calculated from the AC impedance spectra.

Temperature	300°C	400°C	500°C	600°C	700°C
R_{Ω} (Ωcm^2)	14.97 ± 0.10685	5.736 ± 0.31367	7.733 ± 0.29663	6.982 ± 0.25332	8.83 ± 0.26774
$Q(s^n/M\Omega cm^2)$	10.5430 ± 1.0146	6.1239 ± 2.1383	5.4992 ± 1.315	14.164 ±2.6866	14.018 ±1.8036
n	0.8706 ± 0.00991	0.9337 ± 0.03509	0.9005 ±0.02379	0.875 ±0.02083	0.82488 ±0.01393
C_d($\mu F/cm^2$)	3.4122 ± 0.3284	3.7166 ± 1.2977	2.4383 ± 0.5807	7.6757 ± 1.4559	5.6396 ± 0.7256
R_{ct} (Ωcm^2)	36.66 ± 0.6668	69.66 ± 7.2125	66.71 ± 3.0044	310 ± 44.818	395.5 ± 32.36

Rate capability of 2.5 ~ 3.5 V region

The discharge rate capability was conducted at different charge/discharge current densities after 50th cycle and discharge curves for the Li-ion cell with $LiMn_2O_4$ film grown at 300 ~ 700°C in the range of 2.5 ~ 3.5 V are shown in Figure 4-16. It is evident that the average discharge potential of discharge curve was decreased with increasing the discharge current density applied. The voltage of an electrochemical cell unavoidably is decreased with increasing current. This phenomenon can account for ohmic drop in the electrolyte and polarization due to an overpotential induced by the kinetic limitation. Since the ohmic drop $V_{el} = R_{el} \times i$, the voltage drops with increasing the current. The overpotential induced by kinetic limitations of ion insertion or electron transfer at the electrode with high current density would decrease the operating voltage. The polarization contribution to the voltage drop would mainly account for larger voltage drop in the thin film cathodes grown at 600°C and 700°C, which had larger charge transfer resistances than those of films grown at low temperature.

The relative capacity with increasing discharge current density up to 10 C rate is shown in Figure 4-17 for thin film cathodes grown at different temperatures. The films grown at 400°C and 500°C exhibited more than 60% of the 1 C rate capacity at even 10 C rate whereas less than 10% for the film grown at 600°C and 700°C. It should be noted that the rate capability, which represents the ability to charge and discharge at high current required, of the thin film cathodes is strongly dependent upon both the charge transfer at the interface between electrode and electrolyte and the diffusion of Li in the thin film cathodes. The higher diffusion coefficient and the lower R_{ct}, the higher discharge rate capability was obtained for the thin film cathodes grown at low temperature. On the contrary, in case of thin film cathodes grown at high temperature the charge transfer process was believed to become an important factor that determines the rate capability of the cell because of the significantly high R_{ct} by the abnormally large and agglomerated grains.

Cyclic voltammetry of 2.5 ~ 4.5 V region

In order to examine the validity of the thin film cathodes for 4 V region, the electrochemical measurement in the range of 2.5 ~ 4.5 V was performed with the cell with cathodes grown at 300°C and 500°C. Cells with the cathode films grown at higher temperatures were excluded in this experiment due to their poor characteristics at the 3 V region. The cyclic voltammograms for $LiMn_2O_4$ thin films grown at 300°C and 500°C between 2.5 and 4.5 V at a sweep rate of 0.1 mV/s are shown in Figure 4-18 (a) and (b), respectively. The cell was initially charged to 4.5 V before the measurement. The current-voltage traces clearly illustrated the reversibility of thin film cathodes upon intercalation and deintercalation of lithium ions over the voltage range 2.5 to 4.5 V as reported in previous literature [Ros90, Tar91b, Tha83, Tha84]. The two anodic peaks and two cathodic peaks, corresponding to the reversible two-stage process of λ-$MnO_2 \leftrightarrow LiMn_2O_4$, are observed to occur at 4 V region while a pair of anodic-cathodic peak at 3 V region is represented as the reversible reaction $LiMn_2O_4 \leftrightarrow Li_2Mn_2O_4$, which results in the cubic-tetragonal transformation due to the Jahn-Teller distortion. The film grown at 300°C showed a broad and poorly resolved peak at 4 V region, indicating the presence of defects and high disorder due to the poor crystallinity [Mor01, Xia97b]. For both films, the separation between anodic (E_{pa}) and cathodic potential peak (E_{pc}) at 4 V region was much smaller than that at 3 V region, representing the better reversibility at 4 V region.

Cycling behavior of 2.5 ~ 4.5 V region

Discharge curves of the cell with $LiMn_2O_4$ thin film cathodes grown at 300°C and 500°C in the range of 2.5 ~ 4.5 V at a current density of 60 $\mu A/cm^2$ are shown in Figure 4-19(a) and (b), respectively. Film grown at 300°C delivered the initial capacity of 43.4

μAh/cm^2·μm whereas the film grown at 500°C showed the first capacity of 68.83 μAh/cm^2·μm. Capacity at 4 V region as well as capacity at 3 V region were increased with increasing substrate temperature. This might be ascribed to the better crystallinity and less defects of the film grown at 500°C leading to the higher diffusion coefficient of Li into/from the electrode as shown previously. Also, the increased amount of Mn^{3+} in the films grown at 500°C led to the higher capacity at both 3 V and 4 V regions. Capacity loss of the film grown at 300°C was more rapid than that of the film grown at 500°C due to the very poor capacity retention characteristic at 3 V region of the film grown at 300°C. After 100 cycles, the capacities of films grown at 300°C and 500°C were retained about 66.67% and 80.43% of their initial capacities, respectively. The higher capacity retention at 4 V than 3V was obtained for both films that was expected from the separation between anodic and cathodic potential peaks in the CV measurement. The capacity loss in the range of 2.5 ~ 4.5 V was slightly increased compared to that in 3 V region only due to the relatively higher capacity retention of 4 V region. It should be noted that the electrochemical characteristics in the range of 2.5 ~ 4.5 V of $LiMn_2O_4$ films grown were strongly dependent upon those of 3 V region because of the higher capacity and poorer capacity retention of 3 V region than 4 V region.

Summary

Using PLD technique $LiMn_2O_4$ thin films were grown in 500 mtorr of oxygen at 300 ~ 700°C. From the XRD, the crystallinity and grain size of the films were increased with increasing temperature. In addition, the lattice constant of the film was increased with increasing temperature due to the transition of Mn ion from 4+ to 3+, which was confirmed by the relative ratio of Mn^{3+}/Mn^{4+} on Mn $2p_{3/2}$ in XPS. The results shown in

SEM and TEM were in a good agreement with each other in terms of the grain size and crystallinity. Films grown at low temperature showed uniform grains with some extent of defects while films grown at high temperature revealed the large and agglomerated grains with good crystallinity.

There was a tendency that the initial discharge capacity of 3 V region was increased with increasing substrate temperature in the range of 300°C ~ 500°C and then decreased at higher temperatures. The main reason for the increment of the initial discharge capacity was ascribed to the increase of amount of Mn^{3+} and improved crystallinity with temperature leading to facilitated intercalation and deintercalation of lithium. The lower capacity of the thin film cathodes grown at high temperature was attributed to the inhomogeneous electrochemical reaction due to the abnormally agglomerated grains and high contact resistance.

Capacity retention on cycling in the 3 V region was decreased with increasing temperature. For a thin film cathode grown at 300°C the capacity loss was mainly occurred by the dissolution of cathode in the electrolyte due to the large surface area contacted with the electrolyte. As the substrate temperature was increased, the Jahn-Teller distortion became a predominant contribution to the capacity loss. The thin film cathode grown at 700°C lost more than 50% of its initial discharge capacity even before 10 cycles. The films grown at relatively low temperature exhibited the better capacity retention because structural defects and uniform distribution of grains might help to retain the structural integrity upon repeated cycling.

Thin film cathodes with high diffusion coefficient of Li^+ and low charge transfer resistance exhibited the better discharge rate capability. The rate capability is dependent on the charge transfer resistance at the interface between the oxide electrode and the electrolyte as well as the diffusion coefficient of Li^+ the electrode.

The discharge capacity of 3 V was larger than that of 4 V for the films grown at 300°C and 500°C. The discharge capacity of 2.5 ~ 4.5 V was increased with increasing temperature because of increased capacities at both 3 V and 4 V with increasing temperature. The total capacity retention of 2.5 ~ 4.5 V for film grown at 500°C was better than that for grown at 300°C due to the poorer capacity retention at 3 V of the latter. It is concluded that the electrochemical behavior in the range of 2.5 ~ 4.5 V of the thin film cathode is strongly dependent on that of 3 V in terms of the capacity and capacity fade on cycling.

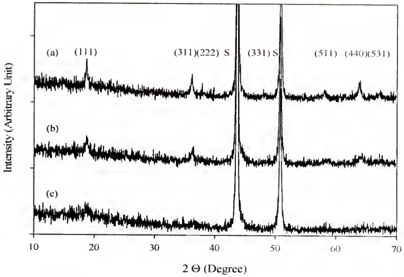

Figure 4-1. XRD of $LiMn_2O_4$ thin films grown in 500 mtorr of O_2 at (a) 700°C, (b) 500°C, and (c) 300°C.

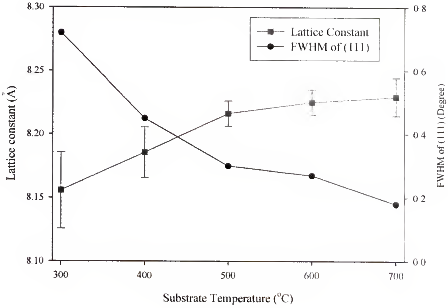

Figure 4-2. Lattice constant (left) and FWHM of (111) peak (right) of $LiMn_2O_4$ thin films grown in 500 mtorr of O_2 as a function of substrate temperature.

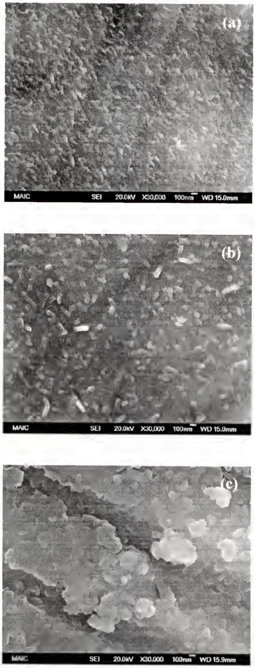
(a)
MAIC SEI 20.0kV X30,000 100nm WD 15.0mm
(b)
MAIC SEI 20.0kV X30,000 100nm WD 15.0mm
(c)
MAIC SEI 20.0kV X30,000 100nm WD 15.9mm

Figure 4-3. SEM micrographs of $LiMn_2O_4$ thin films grown in 500 mtorr of O_2 at (a) 400°C, (b) 500°C, and (c) 700°C.

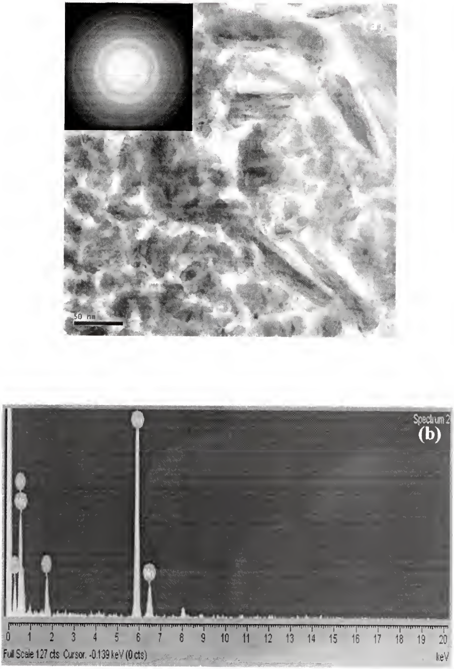

Figure 4-4. TEM of $LiMn_2O_4$ thin films grown in 500 mtorr of O_2 at 500°C: (a) Bright field image with selected area electron diffraction (SAD) and (b) Energy dispersive X-ray spectroscopy (EDX).

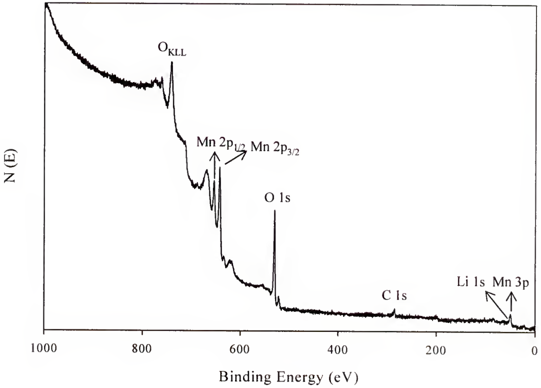

Figure 4-5. XPS survey scan of $LiMn_2O_4$ thin film grown in 500 mtorr of O_2 at 300°C.

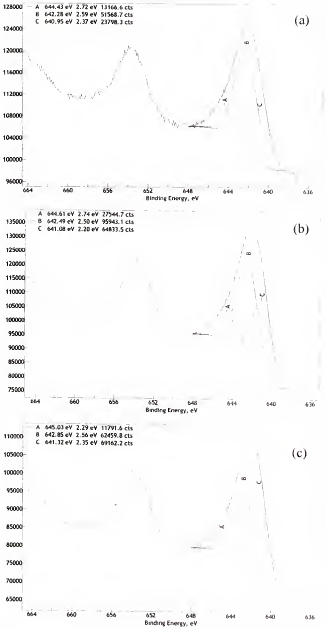

Figure 4-6. High resolution XPS of Mn $2p_{3/2}$ of $LiMn_2O_4$ thin films grown in 500 mtorr of O_2 at (a) 300°C, (b) 500°C, and (c) 700°C.

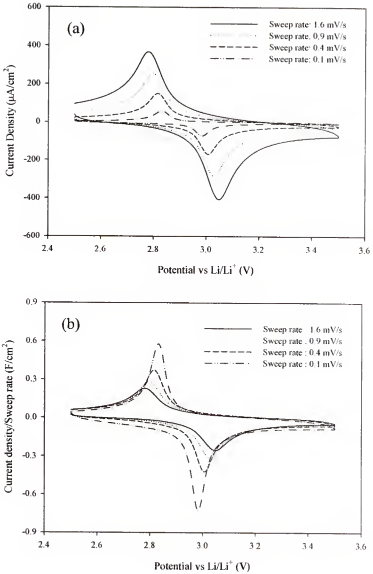

Figure 4-7. Cyclic voltammograms in the range of 2.5 ~ 3.5 V of a $LiMn_2O_4$ thin film grown at 300°C: (a) Normal cyclic voltammograms and (b) Psudocapacitances at different sweep rates.

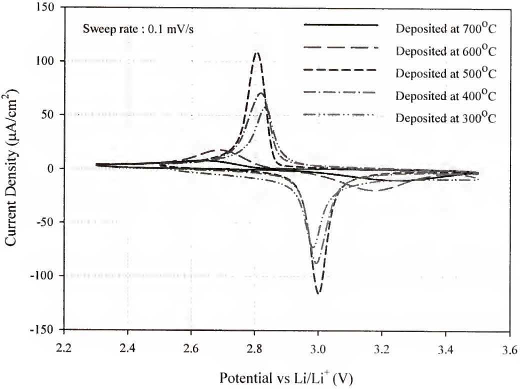

Figure 4-8. Cyclic voltammograms in the range of 2.5 ~ 3.5 V of $LiMn_2O_4$ thin films grown at 300°C, 400°C, 500°C, 600°C, and 700°C. Sweep rate : 0.1 mV/s.

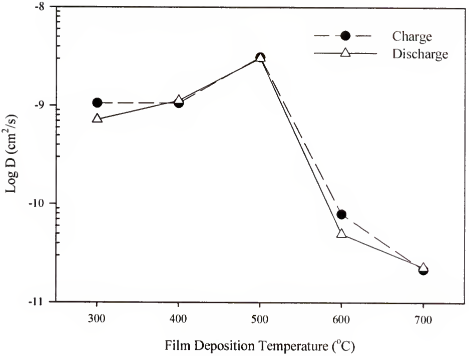

Figure 4-9. Diffusion coefficients of Li^+ in the $LiMn_2O_4$ thin film as a function of substrate temperature.

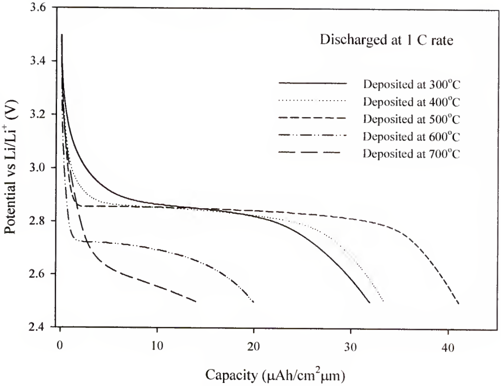

Figure 4-10. The first discharge curves in the range of 2.5 ~ 3.5 V of $LiMn_2O_4$ thin films grown at 300°C, 400°C, 500°C, 600°C, and 700°C. Discharge rate: 1 C rate.

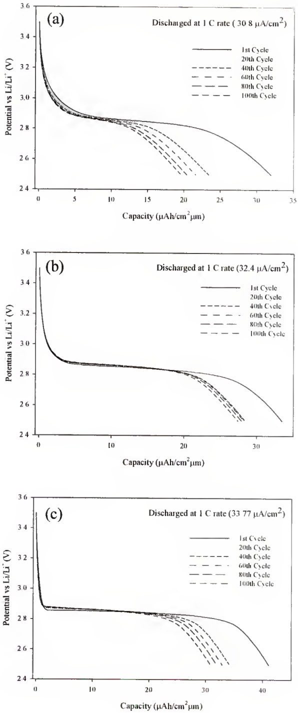

Figure 4-11. Discharge curves in the range of 2.5 ~ 3.5 V of $LiMn_2O_4$ thin films grown at (a) 300°C, (b) 400°C and (c) 500°C.

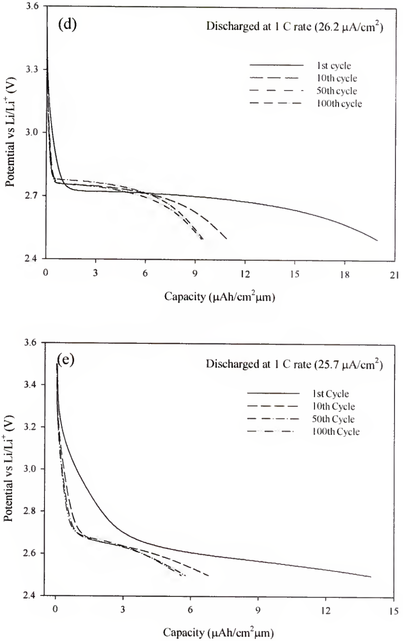

Figure 4-11. Discharge curves in the range of 2.5 ~ 3.5 V of a $LiMn_2O_4$ thin film grown at (d) 600°C and (e) 700°C.

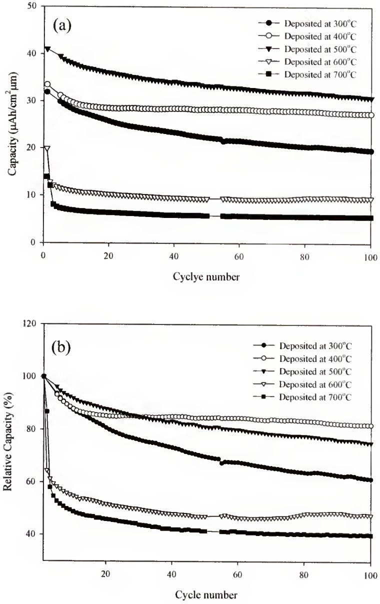

Figure 4-12. Discharge capacity as a function of cycle number in the range of 2.5 ~ 3.5 V of $LiMn_2O_4$ thin films grown at different temperatures: (a) Specific discharge capacity and (b) Relative discharge capacity.

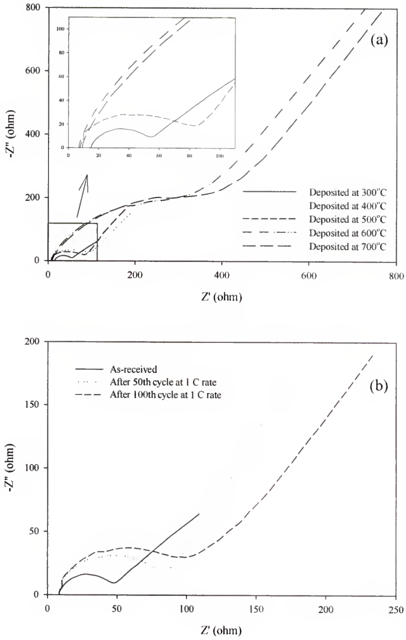

Figure 4-13. AC impedance spectroscopy of $LiMn_2O_4$ thin films: (a) As-received $LiMn_2O_4$ thin films grown at different temperatures and (b) $LiMn_2O_4$ thin film grown at 300°C after cycling.

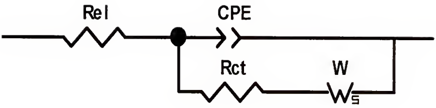

Figure 4-14. Equivalent circuit used for the fitting of the Nyquist plots.

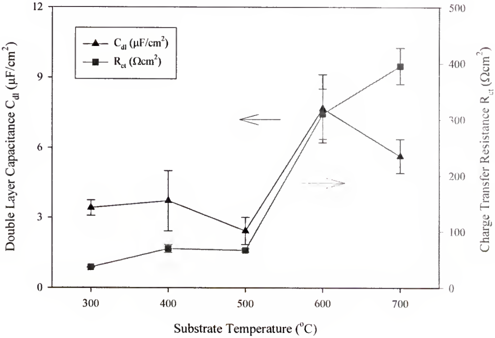

Figure 4-15. Double layer capacitance and charge transfer resistance of $LiMn_2O_4$ thin films grown at different temperatures.

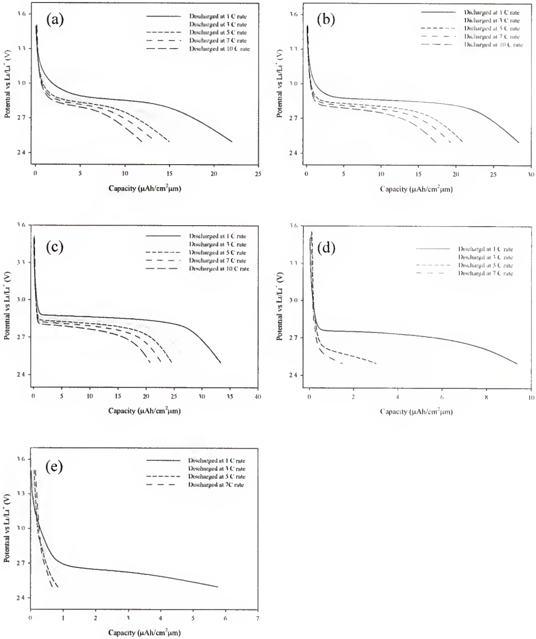

Figure 4-16. Discharge curves at different current densities of $LiMn_2O_4$ thin films grown at (a) 300°C, (b) 400°C, (c) 500, (d) 600°C, and (e) 700°C.

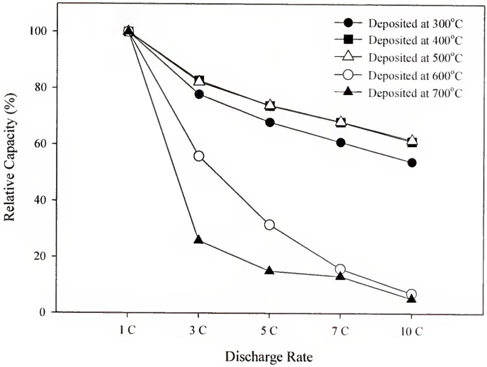

Figure 4-17. Discharge rate capability in the range of 2.5 ~ 3.5 V of $LiMn_2O_4$ thin films grown at different temperatures.

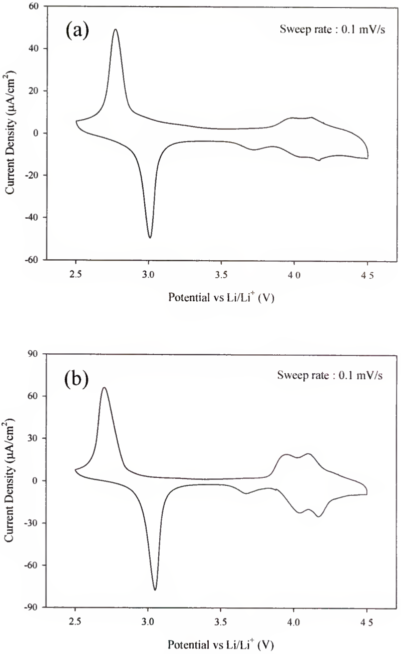

Figure 4-18. Cyclic voltammograms in the range of 2.5 ~ 4.5 V of $LiMn_2O_4$ thin films grown at (a) 300°C and (b) 500°C. Sweep rate: 0.1 mV/s.

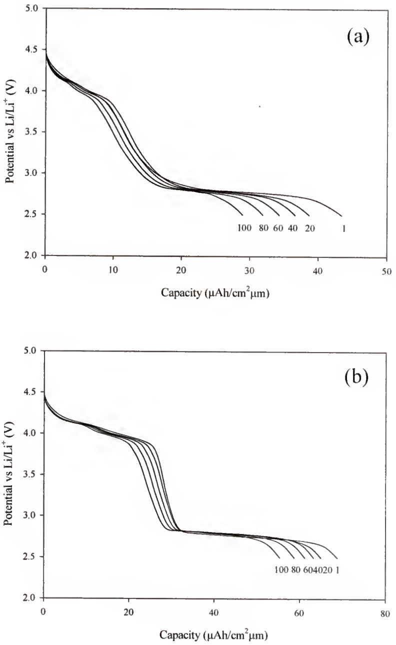

Figure 4-19. Discharge curves in the range of 2.5 ~ 4.5 V of $LiMn_2O_4$ thin films grown (a) 300°C and (b) 500°C. Discharge rate : 60 μA/cm^2.

CHAPTER 5
EFFECT OF ALUMINUM DOPING ON THE ELECTROCHEMICAL CHARACTERISTICS OF LITHIUM MANGANESE OXIDE THIN FILM CATHODES

Introduction

As mentioned earlier, the wide use of spinel $LiMn_2O_4$ as a cathode for the Li-ion batteries has been restricted by its poor rechargeability caused from several possible reasons: (1) dissolution of Mn into the electrolyte [Bly98, Cho99, Kan96, Rob97, Xia98], (2) the onset of Jahn-Teller distortion [Guo96, Sun00, Tha95], (3) decomposition (oxidation) of the electrolyte [Jan96, Xia97a], and (4) structural instability of $LiMn_2O_4$ [Xia96, Xia97a, Xia98]. Numerous attempts have been employed to improve its cycle stability. Among them partial substitution of Mn with other metallic elements such as Co, Ni, and Al has shown to be a very effective way for improving the cycle performance of $LiMn_2O_4$. [Guo96, Tar91a, Woh97]. The lithium intercalation properties of $LiAl_xMn_{2-x}O_4$ have been reported by Le Cras *et al.* [LeC96]. Since aluminum is light in weight, abundant, and relatively inexpensive, Al-substituted lithium manganese oxide spinel is expected to be a cathode material with higher specific energy, lower cost, and less toxicity.

In this experiment, the effect of Aluminum doping on the electrochemical characteristics of lithium manganese oxide thin film cathodes has been studied using the PLD technique.

Experimental

$LiAl_xMn_{2-x}O_4$ (x= 0.1, 0.2, 0.3) powder was synthesized by the melt-impregnation method [Lee01]. A mixture of Li_2CO_3 (Alfa Aesar, 99.999%), MnO_2 (Alfa Aesar, 99.9%), and $Al(NO_3)_3 \cdot 9H_2O$ (Alfa Aesar, 99.999%) with appropriate ratios was immersed in acetone and ball-milled with zirconia media for 1 day. The suspension was dried at 80°C for 24 hours, calcinated at 540°C for 5 hours, and then sintered at 800°C for 12 hours in air. The heating and cooling rates were 10°C/min. The powder was grinded well in the mortar. The as-prepared Al-doped $LiMn_2O_4$ powder of 10 g was first uniaxially pressed with a pressure of 5000 psi resulting in a disk with diameter of 1.25 inch and thickness of 0.25 inch. This fragile pellet was isostatically pressed with 150 MPa for 10 min. The pressed pellet was sintered at 800°C for 24 hours in air. The heating and cooling rates were 10°C/min.

All thin film cathodes in this experiment were grown at 500°C in the 500 mtorr of oxygen. The 500°C has been chosen as an optimum substrate temperature because the $LiMn_2O_4$ thin film cathode grown at this temperature exhibited the best electrochemical properties in terms of initial discharge capacity and rate capability. The structural characterizations and electrochemical measurements were performed as mentioned in the previous chapter.

Results and Discussions

Structural Characterizations

Figure 5-1 shows the X-ray diffractions of $LiAl_xMn_{2-x}O_4$ (x = 0.1, 0.2, 0.3) targets fabricated as mentioned in the experimental procedures. Even though it has been known that the Al replacement for the transition metal site is not easy because of the formation of undesired oxide phases such as Al_2O_3, γ-Al_2O_3, β-$LiAlO_2$ [Ohz95, Zho95], the diffraction patterns of all three target materials showed the characteristics of the cubic spinel phase with the space group of $Fd\bar{3}m$. There was no detectable peak corresponding to other phases as impurities according to the X-ray diffraction. This result confirmed that the melt-impregnation method is one of successful techniques to get a desired phase, especially Al-doped lithium manganese oxide since it allows precursors to be more homogeneously and easily reacted with one another resulting in a pure phase. The lattice constants measured from XRD data were smaller than that of the stoichiometric $LiMn_2O_4$ ($a = 8.247$ Å) and decreased with increasing the amount of Al doped because smaller Al^{3+} (0.535 Å) replaced Mn^{3+} (0.645 Å) in the 16d octahedral sites [Kim03, Myu01]. This feature can be easily seen by shifting of the position of diffraction peaks toward a higher angle with increasing the amount of Al, meaning that the lattice constants linearly were decreased. The lattice constants of $LiAl_{0.1}Mn_{1.9}O_4$, $LiAl_{0.2}Mn_{1.8}O_4$, and $LiAl_{0.3}Mn_{1.7}O_4$ targets were 8.2203, 8.2006, and 8.1814 Å.

X-ray diffraction of $LiAl_xMn_{2-x}O_4$ ($x = 0.1, 0.2, 0.3$) films grown in the oxygen of 500 mtorr at 500°C are shown in Figure 5-2. XRD showed the same characteristics as that of undoped $LiMn_2O_4$ film grown at same conditions showing no other phases as impurities. The lattice constants of the films were smaller than those of corresponding targets, which might be due to the relatively low temperature for the full crystallization of the films. The lattice constants of the films were decreased with increasing the amount of Al because of the replacement of larger Mn^{3+} with smaller Al^{3+}. Figure 5-3 showed the reduction of the lattice constants with increasing the amount of Al for targets and films grown. The lattice constants of $LiAl_{0.1}Mn_{1.9}O_4$, $LiAl_{0.2}Mn_{1.8}O_4$, and $LiAl_{0.3}Mn_{1.7}O_4$ films were 8.1817, 8.1622, and 8.1215 Å.

SEM micrographs of the $LiAl_{0.1}Mn_{1.9}O_4$ and $LiAl_{0.2}Mn_{1.8}O_4$ films are shown in Figure 5-4 (a) and (b), respectively. There was no significant difference in both morphology and grain size as a function of the amount of Al doped. The films show uniform grains in shape and size of 50 ~ 70 nm with some agglomerated grains.

XPS survey spectrum of a $LiAl_{0.3}Mn_{1.7}O_4$ film is shown in Figure 5-5. All peaks on the spectrum correspond to the constituted elements such as Li, Mn, O, and Al. The low binding energy region is enlarged for details in the range of 0 ~ 150 eV showing the peaks of Li 1s, Mn 3s, Mn 3p, O 2s, Al 2s, and Al 2p. The Al 2p peaks have been used to identify the chemical phase of the Al-doped lithium manganese oxide films. There were no obvious peaks at 72.5 eV which represents the metallic aluminum. Instead, there is a peak in the range of 73.8 ~ 74.2 eV assigned as an Al-O bonding in all $LiAl_xMn_{2-x}O_4$ thin film ($x = 0.1, 0.2, 0.3$) [Ahn03, Mou92]. From this result, it can be concluded that aluminum in the films is present as an ion bonded with neighboring oxygen not a simple metallic inclusion. The O 1s binding energy of $LiAl_xMn_{2-x}O_4$ ($x = 0.1, 0.2, 0.3$) thin films are shown in Figure 5-6. It is clear that the O 1s binding energy was slightly increased with increasing the amount of Al doped, which indicates that the Al doping changed the oxidation state of O. From the higher oxidation state of O with Al doping it is reasonable to assume that Al-doped lithium manganese oxide films have stronger bonding between metal and oxygen in the structure than undoped spinel lithium manganese oxide. In addition, the ratio of Mn^{4+} to Mn^{3+} of Al-doped lithium manganese oxide films was higher than that in the undoped spinel, indicating the increase of the average oxidation state of manganese because of decreased amount of Mn^{3+} due to Al^{3+} substitution.

Electrochemical Characteristics

Cyclic voltammetry of 2.5 ~ 3.5 V region

Cyclic voltammetries for the Al-doped lithium manganese oxide films were performed to investigate the basic electrochemical characteristics. The cyclic voltammograms of the $LiAl_xMn_{2-x}O_4$ films (x = 0.1, 0.2, 0.3) showed a pair of distinct anodic and cathodic peaks, which are located around 2.9 V and 2.7 V, respectively, clearly reflect reversible oxidation and reduction reactions corresponding to lithium extraction and insertion. Figure 5-7 shows the CVs for three Al-doped thin film cathodes in the range of 2.5 ~ 3.5 V at the sweep rate of 0.1 mV/s. Both anodic and cathodic potential peaks were shifted to the lower potential when the amount of aluminum was increased.

Discharge capacity of 2.5 ~ 3.5 V region

The initial discharge curves of $LiAl_xMn_{2-x}O_4$ thin films (x = 0.1, 0.2, 0.3) are shown in Figure 5-8 with that of undoped $LiMn_2O_4$ thin film for comparison. Of all cells with Al-doped lithium manganese oxide thin films were discharged in the range of 2.5 ~ 3.5 V at 1 C rate. The initial discharge potential was decreased with increasing the amount of Al substituted. This potential drop with Al doping can be ascribed to the increase of free energy in the system due to the formation of strong Al-O bonding, leading to the stronger total metal-oxygen bonding in the structure. It has been reported that the interaction energy remarkably was increased with Al doping, indicating that the repulsive interaction between lithium positive-positive ions was gradually increased with Al doping content [Myu01].

$LiAl_xMn_{2-x}O_4$ thin film cathodes delivered the initial discharge capacities of 37.22, 33.17, and 27.76 $\mu Ah/cm^2 \cdot \mu m$ for x = 0.1, 0.2, and 0.3, respectively, which are lower than that (41.05 μAh/cm^2·μm) of undoped $LiMn_2O_4$ thin film grown at the same condition. The initial discharge capacities of these cells approximately exhibited a decreasing trend with increasing Al-substitution content in the doped spinels because of a decrease in the amount of extractable Li ion in the spinel. For $LiAl_xMn_{2-x}O_4$, Al^{3+} replaced the place occupied originally by Mn^{3+} and the amount of Mn^{3+} in spinel was reduced by the increasing amount of Al^{3+}. Since Al^{3+} ions cannot be oxidized in this potential range, the amount of removable Li^+ is determined by the amount of Mn^{3+}, and thus, only (1-x) moles of Li^+ can be removed from per mole of $LiAl_xMn_{2-x}O_4$ [Oik99]. During discharging, only a maximum of (1-x) moles of Li^+ can be reinserted into each mole of cathode material.

Cycling behavior of 2.5 ~ 3.5 V region

Figure 5-9 (a) shows the discharge curves of a Li-ion cell with 0.5 μm thick $LiAl_{0.1}Mn_{1.9}O_4$ film cathode grown at 500°C in 500 mtorr of oxygen in the range of 2.5 ~ 3.5 V discharged at 25 μA/cm^2 (1 C rate). The first discharge capacity was about 37.22 μAh/cm^2·μm, which is equivalent to about 62% of the theoretical value of $LiMn_2O_4$. The discharge capacity was decreased to 95.28% of its initial value after 20 cycles. After 100 cycles, the discharge capacity was decreased to 81.3% of its initial capacity, which corresponds to the 0.187% reduction in capacity per cycle. Figure 5-9 (b) shows the discharge curves of a Li-ion cell with $LiAl_{0.2}Mn_{1.8}O_4$ film cathode in the range of 2.5 ~ 3.5 V discharged at 25 μA/cm^2 (1 C rate). $LiAl_{0.2}Mn_{1.8}O_4$ film initially delivered about 33.17 μAh/cm^2·μm, which is equivalent to about 55.3% of the theoretical value of $LiMn_2O_4$. The discharge capacity was gradually decreased to 91.18% of its initial value after 20 cycles. The discharge capacity after 100th cycle was decreased to 82.52% of its initial capacity, which corresponds to the 0.175% reduction in capacity per cycle. Figure 5-8 (c) shows the discharge curves of a Li-ion cell with $LiAl_{0.3}Mn_{1.7}O_4$ film cathode in the range of 2.5 ~ 3.5 V discharged at 25 μA/cm^2 (1 C rate). The first discharge capacity was about 27.76 μAh/cm^2·μm, which is equivalent to about 46.25% of the theoretical value of $LiMn_2O_4$. The discharge capacity was gradually decreased to 97% of its initial value after 20 cycles. The discharge capacity after 100th cycle was decreased to 83.26% of its initial capacity, which corresponds to the 0.167% reduction in capacity per cycle.

The specific discharge capacities and relative capacities of $LiAl_xMn_{2-x}O_4$ thin film (x = 0.1, 0.2, 0.3) cathodes upon cycling are shown in Figure 5-10 (a) and (b). The cycling behavior of undoped $LiMn_2O_4$ thin film grown at the same condition is also shown for comparison. From the results, it can be concluded that the capacity retention on cycling of Al-doped lithium manganese oxide thin film cathodes increased with increasing Al-substitution content in spite of some reduction in the initial discharge capacity, which is in a good agreement with the previous reports for the bulk Al-doped lithium manganese oxide powder [Myu01, Lee01].

For the 3 V region, the onset of Jahn-Teller distortion in deeply discharged $LiMn_2O_4$ electrodes has been known as a major cause of capacity fading on repeated cycling [Gum94, Mas96]. The insertion of Li ions into empty octahedral sites (16c) to $Li_xMn_2O_4$ ($1<x\leq2$) is accompanied by a reduction in the average oxidation state of manganese less than 3.5. The presence of more than half of Jahn-Teller ions (Mn^{3+}) in the host structure introduces a transformation from cubic to tetragonal ($c/a = 1.16$, $\Delta V/V = 6\%$). Upon repeated cycling, this distortion is too severe for the spinel electrode to retain its structural integrity resulting in either deterioration of the electrical contact between the

surface of the insertion material particles or a collapse of spinel framework, thereby rapid capacity loss of the cathode. It has been reported that the onset of Jahn-Teller effect was placed at even x = 1.08 in $Li_xMn_2O_4$ [Tha95]. Our results indicate that the capacity retention on cycling in the range of 2.5 ~ 3.5 V was increased with increasing the amount of Al doped with some sacrifice of the initial discharge capacity. The enhanced rechargeability can be attributed to the increased oxidation state of manganese to higher than 3.5 by the replace of Mn^{3+} with Al^{3+}, which might delay or alleviate the Jahn-Teller effect during the cycling. From the decrease in lattice constant with increase of Al doped shown in Figure 5-3, it was able to deduce that the average oxidation state of manganese would be gradually increased in proportion to the augmentation of Al content, that is, Al^{3+} should replace Mn^{3+} in 16d site in the cubic spinel structure. XPS results also confirmed that relative ratio of Mn^{3+} to Mn^{4+} was decreased with increasing the mount of Al doped, indicating an increase of the average oxidation state of manganese.

AC impedance of 2.5 ~ 3.5 V region

AC impedance spectra at the open-circuit voltage of as-received $LiAl_xMn_{2-x}O_4$ (x = 0, 0.1, 0.2, 0.3) thin film cathodes are shown in Figure 5-11. The spectra showed a typical Nyquist plot in which the real and imaginary impedances are drawn as a function of the given frequency. As mentioned in chapter 2, the semicircle in the high frequency region is due to the charge transfer reaction at the interface of the electrolyte/electrode, and the inclined line in the low frequency region is attributed to Warburg impedance that is associated with lithium diffusion through the electrode [Cho95]. It can be qualitatively concluded that the charge transfer resistance was increased with increasing the amount of aluminum substituted because the diameter of semicircle in the high frequency region was increased with increasing x of $LiAl_xMn_{2-x}O_4$ thin film cathodes.

The details on fitting of the Nyquist plots obtained using the modified equivalent circuit are shown in the Appendix. Calculated values including charge transfer resistance (R_{ct}) and double layer capacitance (C_{dl}) are shown in the Table 5-1 with the calculated diffusion coefficients using the Randles-Sevcik equation from the cyclic voltammetries [Ran48, Sev48].

Table 5-1. Parameters calculated from the AC impedance spectra of $LiAl_xMn_{2-x}O_4$ thin films grown by PLD.

x	0	0.1	0.2	0.3
R_Ω (Ωcm^2)	7.733 ± 0.29663	10.23 ± 0.22034	8.302 ± 0.27188	8.973 ± 0.28154
C_{dl}($\mu F/cm^2$)	2.4383 ± 0.5807	2.4833 ± 0.2852	2.5178 ± 0.3371	2.6823 ± 0.4009
R_{ct} (Ωcm^2)	66.71 ± 3.0044	162.7 ± 5.3333	200.6 ± 9.4482	215.7 ± 18.962
D_{ch} (cm^2/s)	3.177×10^{-9}	2.779×10^{-10}	2.761×10^{-10}	7.59×10^{-10}
D_{disch} (cm^2/s)	3.033×10^{-9}	4.079×10^{-10}	3.519×10^{-10}	1.227×10^{-10}

There was no significant difference in the electrolyte resistance (R_Ω), which was in 7 ~ 10 Ωcm^2 for all films regardless of the amount of Al doped. R_Ω can be easily determined from the intercept of the semicircle and the abscissa at the high frequency region on the Nyquist plot. The double layer capacitance was increased slightly with increasing of Al substituted from 2.4383 $\mu F/cm^2$ to 2.6823 $\mu F/cm^2$ for $x = 0$ and $x = 0.3$ in $LiAl_xMn_{2-x}O_4$, respectively. The charge transfer resistance was increased with increasing Al-substitution content as expected from the Nyquist plot shown in Figure 5-11. The increment of R_{ct} with increasing the amount of aluminum can be mainly attributed to the increase in the repulsive interaction between lithium positive-positive ions at the surface of cathode contacted with the electrolyte because of the stronger total metal-oxygen bonding in the structure by substitution of aluminum. The diffusion coefficients of Li ions in the Al-doped cathodes were one order of magnitude lower than that of undoped spinel cathode and decreased with increasing the amount of aluminum doped. The reduction in diffusion coefficients of Li ions in the Al-doped spinel can be explained by changes in bonding energy between metal and oxygen bonding [Joh97, Myu01]. Since the stronger bonding of Al-O than that of Mn-O can lead to the restricted contraction and/or expansion of the structure, the lithium diffusion through 8a-16c-8a path during intercalation/deintercalation of lithium ions into/from the structure could be affected by the limited crystal lattice contraction, though the structure is stabilized by the Al substitution. Also, some of Al doped occupied at empty 16c, which is a path of Li^+ diffusion, might hinder the Li diffusion leading to lower diffusion coefficients.

Rate capability of 2.5 ~ 3.5 V region

The discharge rate capability was conducted at different charge/discharge current densities after 50th cycle and discharge curves for the Li-ion cells with $LiAl_xMn_{2-x}O_4$ films in the range of 2.5 ~ 3.5 V are shown in Figure 5-12. As explained in chapter 4, it is evident that the average discharge potential of discharge curve was decreased with increasing the discharge current density applied because of the ohmic drop in the electrolyte and polarization due to an overpotential induced by the kinetic limitation. The discharge capacity of a thin film cathode was decreased with increasing current density. The degree of reduction in discharge capacity with increasing current density became greater as the value of x in $LiAl_xMn_{2-x}O_4$ thin films was increased from 0.1 to 0.3 shown in Figure 5-12 (a), (b) and (c).

The relative capacity with increasing discharge current density up to 10 C rate is shown in Figure 5-13. The rate capabilities of all Al-doped films were poorer than that of undoped spinel $LiMn_2O_4$ film. Even at 5 C rate, the Al-doped films delivered less than

60 % of the capacity at 1 C rate whereas the undoped $LiMn_2O_4$ film maintained about 75 %. The capacity at 10 C rate was about 49%, 46%, 30% of the capacity at 1 C rate for x = 0.1, 0.2, and 0.3 in $LiAl_xMn_{2-x}O_4$ film, which is much less than that of undoped $LiMn_2O_4$ film (~ 62%).

It should be noted that the rate capability, which represents the ability to charge and discharge at high current required, of the thin film cathodes is strongly dependent upon both the charge transfer at the interface between electrode and electrolyte and the diffusion of Li^+ in the thin film cathodes. The higher diffusion coefficient and the lower R_{ct}, the higher discharge rate capability was obtained for the thin film cathodes. Therefore, $LiAl_xMn_{2-x}O_4$ (x = 0.1, 0.2, 0.3) thin film cathodes exhibited the lower rate capability than undoped $LiMn_2O_4$ thin film cathodes because both charge transfer resistances and diffusion coefficients were decreased with increasing the amount of Al substituted.

Cyclic voltammetry of 2.5 ~ 4.5 V region

As performed in the previous chapter, the cells with Al doped lithium manganese oxide thin film cathodes were electrochemically characterized in the range of 2.5 ~ 4.5 V to verify the ability of the cathodes for 4 V region. The cyclic voltammetries of Al-doped thin film cathodes scanned at a sweep rate of 0.1 mV/s are shown in Figure 5-14. As shown in the 3 V region measurement, each cathode showed a distinct pair of anodic and cathodic peaks at 2.9 V and 2.7 V, respectively. One interesting feature form the CV of Al-doped lithium manganese oxide cathodes is the 4 V region, which became less pronounced with increasing x in $LiAl_xMn_{2-x}O_4$. There were two sharp peaks in the 4 V region on the cyclic voltammetry of undoped $LiMn_2O_4$ thin film cathode shown in Figure 4-18 (b). The first anodic and cathodic peaks at 3.95 and 4.05 V correspond to Li ion extraction/insertion between $LiMn_2O_4$ and $Li_{0.5}Mn_2O_4$. Furthermore, the second anodic and cathodic peaks at 4.1 and 4.17 V correspond to Li ion extraction/insertion between $Li_{0.5}Mn_2O_4$ and 2λ-MnO_2 [Liu96]. The disappearance of two peaks on 4 V region can be attributed to the difference in ionic radius between Al^{3+} and Mn^{3+}. The substitution of smaller Al^{3+} for Mn^{3+} reduces the crystal lattice constants and increases the bonding of Mn-O as well as the strength of the framework of the intercalation compound. This might induce the insertion/extraction of Li ions at the 4 V region in single-phase without undergoing two-phase reaction between the unstable cubic $Li_{0.5}Mn_2O_4$ and λ-MnO_2 at 4.1 V during the electrochemical cycling.

Discharge capacity and cycling behavior of 2.5 ~ 4.5 V region

The initial discharge curves of $LiAl_xMn_{2-x}O_4$ thin film cathodes are shown in Figure 5-15. Both charge and discharge were conducted at the same 1 C rate. The undoped $LiMn_2O_4$ thin film cathode has two plateaus at 4 V region, which corresponds to the two cubic phases of $Li_{0.5}Mn_2O_4$ and λ-MnO_2 while Al-doped thin film cathodes show no two-plateau at 4 V region as expected from the their cyclic voltammetries. In the 3 V region, the degree of flatness on the discharge curve, which has been known as an indicator of mixture phase of cubic and tetragonal due to the Jahn-Teller distortion, was decreased with increasing the amount of Al doped. This result indicates that the Al^{3+} substitution for Mn^{3+} at 16d sites may help to maintain the structural integrity of cathode on charge/discharge, resulting in a higher resistance to the phase transformation.

The initial discharge capacity of 3 V region out of 2.5 ~ 4.5 V was decreased as the amount of Al was increased, which is in a good accordance with the results from the cycling behavior performed in only 2.5 ~ 3.5 V region. As shown in 3 V region out of 2.5 ~ 4.5 V, the initial discharge capacities at 4 V region out of 2.5 ~ 4.5 V of Al-doped thin film cathodes were less than that of undoped thin film cathode and decreased significantly with increasing the amount of Al substituted. This behavior is ascribed to the decrease in the Mn^{3+} amount available for the oxidation to Mn^{4+} by the substitution of Al^{3+} for Mn^{3+}. At $x = 0.3$, the initial discharge capacity of 4 V out of 2.5 ~ 4.5 V was less than half of that obtained from the undoped spinel cathode. Therefore, the whole discharge capacity of 2.5 ~ 4.5 V was reduced as the amount of Al substituted was increased. The initial discharge capacity of $LiAl_xMn_{2-x}O_4$ thin film cathodes for $x = 0, 0.1, 0.2, 0.3$ in the range of 2.5 ~ 4.5 V was 68.83 $\mu Ah/cm^2 \cdot \mu m$, 57.73 $\mu Ah/cm^2 \cdot \mu m$, 49.54 $\mu Ah/cm^2 \cdot \mu m$, and 38.66 $\mu Ah/cm^2 \cdot \mu m$, respectively.

The discharge curves on cycling of $LiAl_xMn_{2-x}O_4$ thin film cathodes in the range of 2.5 ~ 4.5 V at 1 C rate are shown in Figure 5-16. From the results on discharge behaviors of Al-doped lithium manganese oxide thin film cathodes, it can be concluded that the rechargeability, that is capacity retention on cycling at both 3 V and 4 V regions, was improved with increasing the amount of aluminum substituted with some sacrifice of initial discharge capacity. This behavior can be more clearly seen in Figure 5-17 (a) and (b) in which the specific and relative capacities in the range of 2.5 ~ 4.5 V of the $LiAl_xMn_{2-x}O_4$ thin film cathodes are shown up to 100th cycle. The undoped spinel $LiMn_2O_4$ thin film cathode in the range delivered the highest discharge capacity about 69 $\mu Ah/cm^2 \cdot \mu m$ but exhibited the fastest capacity fade on cycling. On the contrary, $LiAl_{0.3}Mn_{1.7}O_4$ showed the best capacity retention after 100th cycle maintaining about 88 % of its first capacity though it delivered the lowest initial discharge capacity of 38.66 $\mu Ah/cm^2 \cdot \mu m$. The improved rechargeability of $LiAl_xMn_{2-x}O_4$ thin film cathodes in 2.5 ~ 4.5 V is considered to be due to the enhanced capacity retention on both 3 V (2.5 ~ 4.5 V) and 4 V (3.5 ~ 4.5 V) regions. The effects of 3 V behavior on the better capacity retention of $LiAl_xMn_{2-x}O_4$ thin film cathodes in 2.5 ~ 4.5 V were previously mentioned.

In the 4 V region, it has been reported that the capacity fade on cycling is mainly related to two irreversible phenomena; structural change and the relation between the electrode and electrolyte (dissolution) [Lee00, Zha02]. Undoped spinel $LiMn_2O_4$ underwent the structural transition into two unstable cubic phases such as $Li_{0.5}Mn_2O_4$ and λ-MnO_2 during Li ion deintercalation and therefore, the capacity loss of spinel $LiMn_2O_4$ was larger than that of Al-doped cathodes. The voltage profile on the discharge curves of $LiAl_xMn_{2-x}O_4$ thin film cathodes ($x = 0.1, 0.2, 0.3$) in Figure 5-15 showed Li ion intercalation/deintercalation occurred in single-phase because there were no plateaus in the discharge curve unlike that in undoped $LiMn_2O_4$ thin film cathode, which had two potential plateaus at 3.9 and 4.1 V regions. The disappearance of two potential plateaus can be ascribed to the strong repulsive interaction between lithium positive-positive ions in the oxide lattice by the substitution of aluminum. Xia *et al.* reported that capacity loss of $LiMn_2O_4$ between 3.9 and 4.2 V was due to the intercalation/deintercalation of lithium ion proceeding in the unstable two cubic phases, $Li_{0.5}Mn_2O_4$ and λ-MnO_2 at around 4.15 V [Xia95]. According to our results, $LiAl_xMn_{2-x}O_4$ thin film cathodes ($x = 0.1, 0.2, 0.3$) maintained a homogeneous phase during the insertion and extraction of lithium ions in the framework. Such structural stability during the electrochemical cycling can improve the rechargeability (capacity retention) of $LiAl_xMn_{2-x}O_4$. Since the strength of bonding of Al-O is greater than that of Mn-O based on the standard Gibbs energies of formation [Lid95], $LiAl_xMn_{2-x}O_4$ would possess higher structural stability. Therefore, the severe expansion/contraction of the cubic structure with electrochemical lithium insertion/extraction was avoided and the manganese dissolution from the oxide into the electrolyte was suppressed, resulting in improved capacity retention upon cycling.

Summary

$LiAl_xMn_{2-x}O_4$ thin film cathodes have been grown in the oxygen of 500 mtorr at 500°C. XRD showed that there was no impurity phase other than a cubic spinel phase as $LiMn_2O_4$. The lattice constant of the thin film was decreased with increasing the amount of Al doped because the smaller Al^{3+} replaced the larger Mn^{3+} at the octahedral sites in the oxide framework. SEM showed no significant difference in grain size of 50 ~ 70 nm and morphology among the $LiAl_xMn_{2-x}O_4$ (x = 0.1, 0.2, 0.3) thin film cathodes. XPS showed the aluminum is present in the cathode as an ion bonded with neighboring oxygen not a metallic inclusion. In addition, the binding energy of oxygen was increased with increasing the amount of Al-substitution due to the enhanced metal-oxygen bonding.

The initial discharge capacity of $LiAl_xMn_{2-x}O_4$ thin film cathodes in the range of 2.5 ~ 3.5 V was less than that of undoped $LiMn_2O_4$ thin film cathode and decreased with increasing the amount of Al doped because the content of Mn^{3+}, which determines the discharge capacity, was reduced by Al substitution. However, the capacity retention upon cycling in the 3 V region was increased with increasing Al substitution content. It might be due to the increase in the average oxidation state of manganese resulting in the restriction or delay of the Jahn-Teller distortion, which has been known as a major mechanism for capacity fade in the 3 V region.

The charge transfer resistance was increased with increasing Al substitution content since Al doping induces the increment of interaction energy of the cathode due to the increased repulsive interaction between Li positive-positive ions. The diffusion coefficient of Li^+ in the cathode was decreased with increasing the amount of Al substituted. It might be due to the decrease in size of the lattice structure, which hinders the intercalation/deintercalation of Li ions with some degree. Therefore, the rate capability of Al-doped lithium manganese oxide thin film cathode was lower than that of undoped thin film cathode and decreased with increase in the amount of Al doped.

The initial discharge capacity of $LiAl_xMn_{2-x}O_4$ thin film cathodes in the range of 2.5 ~ 4.5 V was less than that of undoped $LiMn_2O_4$ thin film cathode and decreased with increasing the amount of Al doped. The initial discharge capacities at 4 V region out of 2.5 ~ 4.5 V of Al-doped thin film cathodes were less than that of undoped thin film cathode and decreased significantly with increasing the amount of Al substituted because of the decrease in the Mn^{3+} amount available for the oxidation to Mn^{4+} by the substitution of Al^{3+} for Mn^{3+}. However, the capacity retention upon cycling was higher than that of undoped $LiMn_2O_4$ thin film cathode and increased with increasing the amount of Al doped. It is considered that the improved capacity retention of Al-doped $LiMn_2O_4$ thin film cathodes at 4 V region is due to the stronger bonding between aluminum and oxygen in the framework structure leading to the increased structural stability, which can prevent unstable two-phase transition and severe dissolution of manganese into the electrolyte.

In summary, the rechargeability of $LiMn_2O_4$ thin film cathode at both 3 and 4 V regions was enhanced when Al^{3+} was substituted for Mn^{3+} in spite of some sacrifice of the discharge capacity. It is reasonable to note that Al doping suppresses the Jahn-Teller distortion and increases the stability of cathode to maintain the structural integrity during repeated intercalation/deintercalation of lithium, resulting in higher capacity retention.

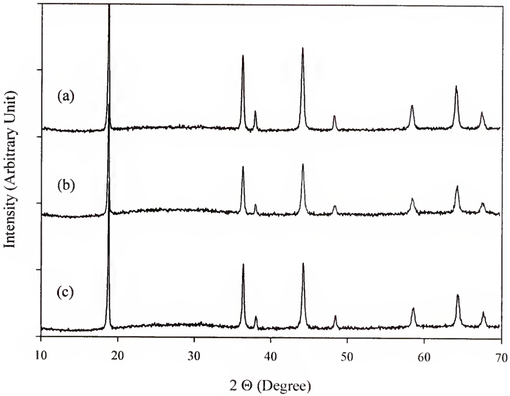

Figure 5-1. XRD of $LiAl_xMn_{2-x}O_4$ targets: (a) x = 0.1, (b) x = 0.2, and (c) x = 0.3.

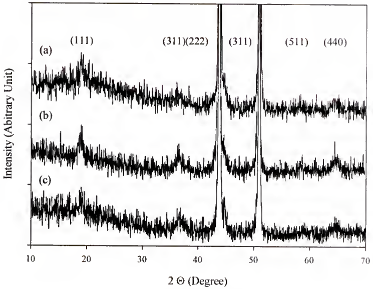

Figure 5-2. XRD of LiAl$_x$Mn$_{2-x}$O$_4$ thin films grown in 500 mtorr of O$_2$ at 500°C: (a) x = 0.1, (b) x = 0.2, and (c) x = 0.3.

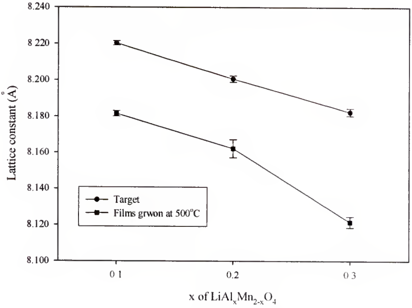

Figure 5-3. Lattice constants of LiAlxMn$_{2-x}$O$_4$ targets and thin films grown in 500 mtorr of O$_2$ at 500°C.

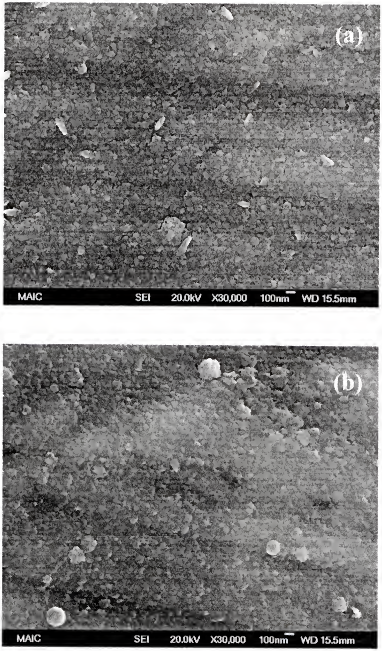

Figure 5-4. SEM micrographs of (a) $LiAl_{0.1}Mn_{1.9}O_4$ and (b) $LiAl_{0.2}Mn_{1.8}O_4$ thin films grown in 500 mtorr of O_2 at 500°C.

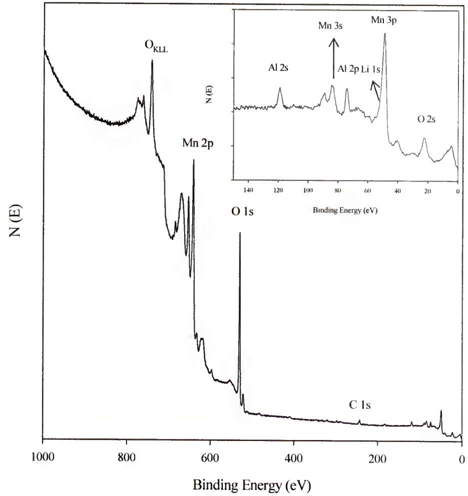

Figure 5-5. XPS survey scan of $LiAl_{0.3}Mn_{1.7}O_4$ thin film grown in 500 mtorr of O_2 at 500°C.

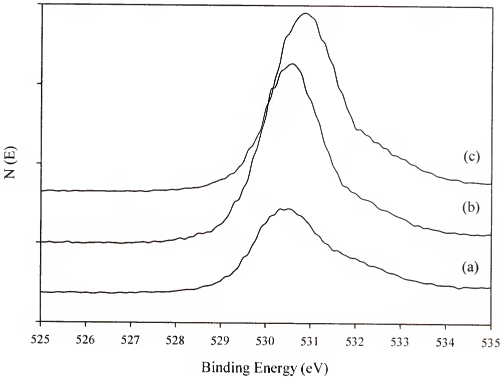

Figure 5-6. O 1s spectra of $LiAl_xMn_{2-x}O_4$ thin film grown in 500 mtorr of O_2 at 500°C: (a) x = 0.1, (b) x = 0.2, and (c) x = 0.3.

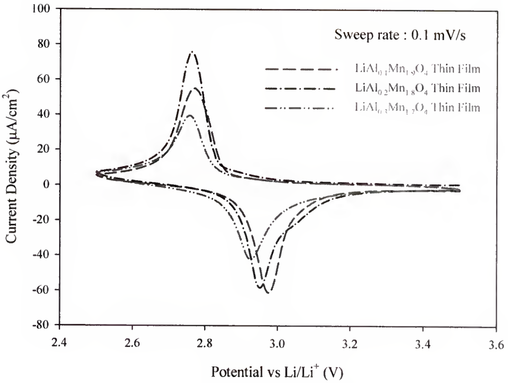

Figure 5-7. Cyclic voltammograms in the range of 2.5 ~ 3.5 V of $LiAl_xMn_{2-x}O_4$ thin films grown in 500 mtorr of O_2 at 500°C.

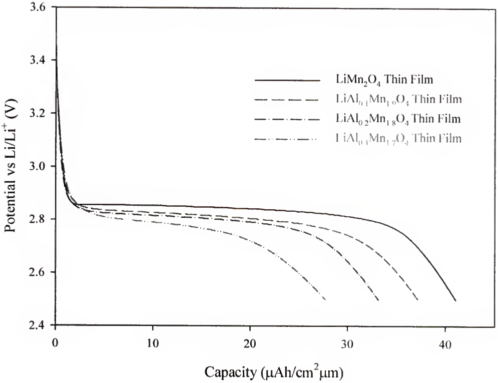

Figure 5-8. The first discharge curves in the range of 2.5 ~ 3.5 V of $LiAl_xMn_{2-x}O_4$ thin films grown in 500 mtorr of O_2 at 500°C.

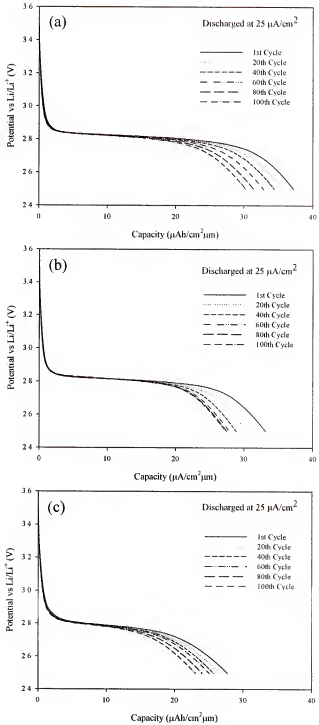

Figure 5-9. Discharge curves in the range of 2.5 ~ 3.5 V of (a) $LiAl_{0.1}Mn_{1.9}O_4$, (b) $LiAl_{0.2}Mn_{1.8}O_4$, and (C) $LiAl_{0.3}Mn_{1.7}O_4$ thin films grown in 500 mtorr of O_2 at 500°C.

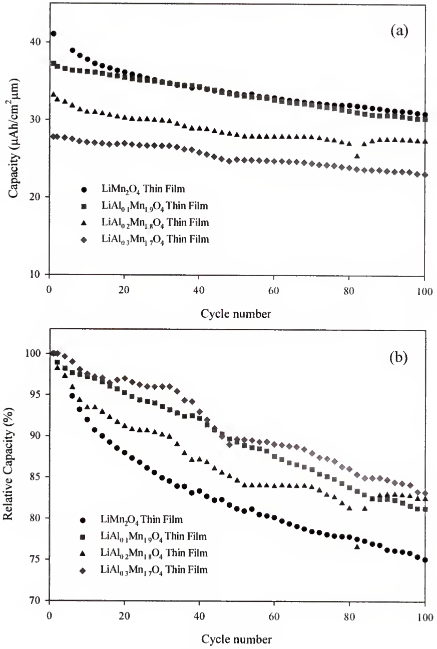

Figure 5-10. Discharge capacity in the range of 2.5 ~ 3.5 V of $LiAl_xMn_{2-x}O_4$ thin films grown in 500 mtorr of O_2 at 500°C: (a) Specific discharge capacity and (b) Relative discharge capacity.

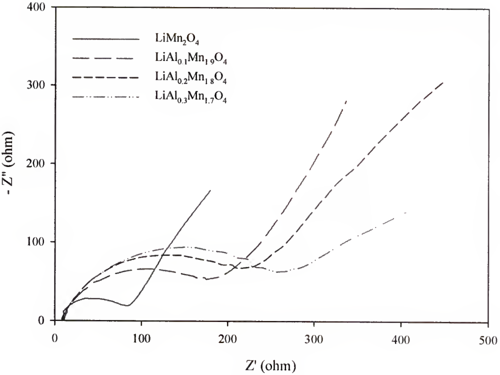

Figure 5-11. AC impedance spectroscopies of $LiAl_xMn_{2-x}O_4$ thin films grown in 500 mtorr of O_2 at 500°C.

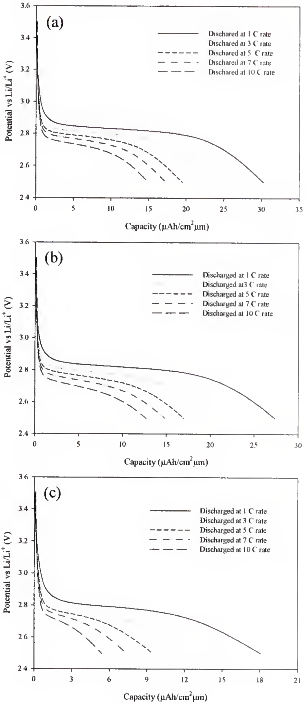

Figure 5-12. Discharge curves at different current densities of (a) $LiAl_{0.1}Mn_{1.9}O_4$, (b) $LiAl_{0.2}Mn_{1.8}O_4$, and (c) $LiAl_{0.3}Mn_{1.7}O_4$ thin films grown in 500 mtorr of O_2 at 500°C.

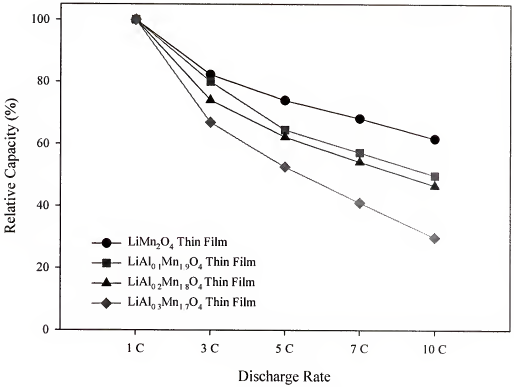

Figure 5-13. Discharge rate capability in the range of 2.5 ~ 3.5 V of $LiAl_xMn_{2-x}O_4$ thin films grown in 500 mtorr of O_2 at 500°C.

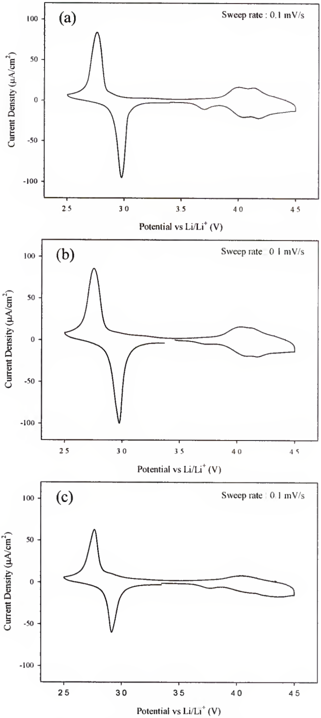

Figure 5-14. Cyclic voltammograms in the range of 2.5 ~ 4.5 V of $LiAl_xMn_{2-x}O_4$ thin films grown in 500 mtorr of O_2 at 500°C: (a) x = 0.1, (b) x = 0.2, and (c) x = 0.3.

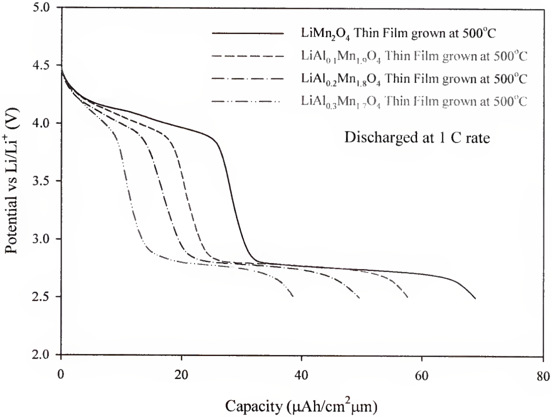

Figure 5-15. The first discharge curves in the range of 2.5 ~ 4.5 V of $LiAl_xMn_{2-x}O_4$ thin films grown in 500 mtorr of O_2 at 500°C. Discharged at 1 C rate.

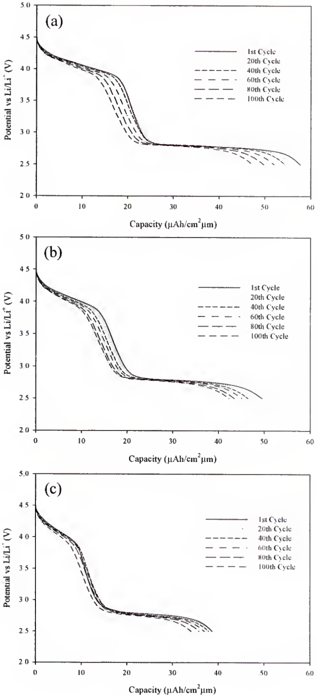

Figure 5-16. Discharge curves in the range of 2.5 ~ 4.5 V of (a) $LiAl_{0.1}Mn_{1.9}O_4$, (b) $LiAl_{0.2}Mn_{1.8}O_4$, and (C) $LiAl_{0.3}Mn_{1.7}O_4$ thin films grown in 500 mtorr of O_2 at 500°C. Discharged at 1 C rate.

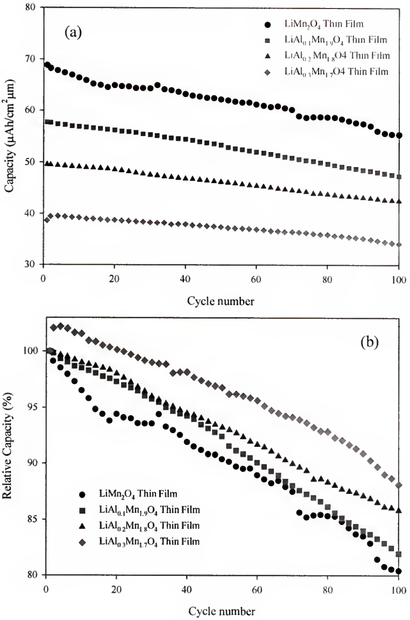

Figure 5-17. Discharge capacity in the range of 2.5 ~ 4.5 V of $LiAl_xMn_{2-x}O_4$ thin films grown in 500 mtorr of O_2 at 500°C: (a) Specific discharge capacity and (b) Relative discharge capacity.

CHAPTER 6
EFFECT OF ULTAR-VIOLET RADIATION ON THE ELECTROCHEMICAL CHARACTERISTICS OF LITHIUM MANGANESE OXIDE THIN FILM CATHODES

Introduction

Jahn-Teller distortion has been known as one of main reasons for the capacity fade on cycling primarily at 3 V and 4 V in a deeply discharged state. Several strategies have been pursued over the years to overcome the difficulties of the spinel $LiMn_2O_4$ cathodes. One important strategy is to develop spinel manganese oxides with a higher oxidation state of manganese because the high oxidation state of manganese can suppress or delay the occurrence of Jahn-Teller distortion upon intercalation/deintercalation. With this perspective, the Li-Mn-O system has been investigated by several research group trying to synthesize the defect (oxygen-rich) spinel lithium manganese oxide, which can be represented as $Li_{1-\delta}Mn_{2-2\delta}O_4$ ($0 \leq \delta \leq 0.11$). Kock *et al.* reported the defect spinel $Li_2Mn_4O_9$ ($\delta = 0.11$) was synthesized at 400°C with lithium and manganese carbonates and confirmed by neutron diffraction as a notation $[Li_{0.89|0.11}]_{8a}[Mn_{1.78|0.11}]_{16d}O_4$ where | represents vacancies [Koc90]. The additional oxygen concentration which created defects on the 8a (tetragonal) and 16d (octahedral) sites gave $Li_2Mn_4O_9$ a significantly great theoretical electrode capacity (213 mAh/g) as discharged to the rock salt composition $Li_5Mn_4O_9$ (3 Li^+ per unit formula) at 3 V region. Defect spinel ($Li_2Mn_4O_{9-\delta}$) containing lithium and manganese vacancies showed much better cyclability (less capacity fade) than stoichiometric spinel electrode at 3 V region due to the increase in the average oxidation state of Mn, resulting in the suppression of the Jahn-Teller distortion [Mas96].

Also $Li_2Mn_4O_{9-\delta}$ with $0.36 < \delta < 0.46$ showed a reversible capacity of about 130 mAh/g in the range of 2 ~ 3.8 V with excellent cyclability [Cho00].

In addition to 3 V region, Xia *et al.* reported that the optimized defect spinels could be reversibly cycled with excellent rechargeability relatively to the spinel $LiMn_2O_4$ at 4 V region at the expense of slight loss of capacity [Xia96c, Xia97b]. They interpreted that the improvement of cyclability in oxygen-rich spinel was attributed to the small unit cell in which a homogenous insertion/extraction could proceed over the entire region. They proposed the optimized Li-Mn-O compositions of spinel to obtain both reasonable capacity and improved rechargeability in the 4 V region.

The use of ultraviolet radiation has been explored as a method of providing a more reactive environment thereby enabling lower temperature processing to be used. Kazor *et al.* reported that the radiation from a low pressure mercury lamp enhanced the low temperature oxidation of Si by up to a factor of 50 [Byo93, Kaz92]. They also proposed that the enhanced oxidation was attributed to the formation of oxygen atoms and ozone, which is known to be stronger oxidizing agent than molecular oxygen, by the photodissociation of UV light. By using this beneficial effect of UV radiation, the ultraviolet-assisted PLD (UVPLD) can dissociate molecular oxygen and form ozone and atomic oxygen, which serve as more reactive gaseous species. It is therefore expected that using *in situ* UV source capable of dissociating oxygen molecules during the PLD process, an even more significant improvement in the quality of the grown layers, especially at low substrate temperatures, could be achieved. It is known that there is typically an oxygen deficiency in the films with respect to the targets even though PLD is an excellent technique for the stoichiometric transfer of the target material to the growing film. Thus, the effort for creating more reactive oxygen species using *in situ* UV radiation would be more effective to increase oxygen concentration in the thin film cathodes, leading to the oxygen-rich spinel.

In this experiment, the defect spinel having vacancies at tetragonal and octahedral sites has been pursued to suppress the effect of Jahn-Teller distortion on the capacity fade on cycling through the increase in the oxidation state of manganese in the thin film cathodes. In addition, the combination of aluminum doping with defect spinel has been examined to enhance the capacity retention with respect to a typical undoped spinel structure.

Experimental

Targets used in this section of experiment were $LiAl_xMn_{2-x}O_4$ (x = 0, 0.1, 0.2, 0.3), which are the same as those used in the previous chapters. Thin film cathodes were grown in the oxygen atmosphere of 500 mtorr at 400°C and 500°C for undoped spinel and 500°C for Al-doped spinel, respectively. All procedures performed were the same as the conventional PLD process except for the UV setup. A pair of low pressure Hg lamps was mounted inside the vacuum chamber and turned on once the desired oxygen pressure and temperature were reached. The structural characterizations and electrochemical measurements were conducted as mentioned in the previous chapters.

Results and Discussions

Structural Characterizations

Figure 6-1 compares X-ray diffraction of $LiMnO_4$ films grown in the oxygen of 500 mtorr at 500°C by UVPLD (a) and conventional PLD (b). The figure shows that the X-ray diffraction peaks are qualitatively similar for both spectra with exception that the peaks in the UVPLD film are much sharper, indicating a higher degree of crystallinity and peaks in the UVPLD film are slightly shifter to the higher angles. The FWHM of the (111) peak grown by PLD was 0.54 while that of UVPLD was 0.42. Also, the peak corresponding to (400) plane was distinguished from the stainless steel substrate in the UVPLD film due to the higher crystallinity and shifting to the higher angle. For the Al-doped thin film cathodes, the XRD of $LiAl_{0.2}Mn_{1.8}O_4$ film grown by UVPLD and PLD in the O_2 of 500 mtorr at 500°C are shown in Figure 6-2 (a) and (b), respectively. There was no detectable peak corresponding to other phases as impurities in both PLD and UVPLD grown Al-doped lithium manganese oxide films. As shown in Figure 6-1, peaks in the $LiAl_{0.2}Mn_{1.8}O_4$ film grown by UVPLD showed a higher crystallinity and were shifted to the higher angles.

The lattice constants calculated from XRD data of $LiAl_xMn_{2-x}O_4$ grown by UVPLD and PLD are shown in Figure 6-3 as a function of x in the films, which are 0, 0.1, 0.2 and 0.3. As the case in the PLD condition reported in the previous chapter, the lattice constants of Al-doped films grown by UVPLD were decreased with increasing of the amount of Al substituted owing to the replacement of larger Mn^{3+} with smaller Al^{3+}. A more interesting feature is the difference in lattice constants of films grown by UVPLD with respect to those of PLD for both undoped and Al-doped thin film cathodes. All films grown by UVPLD exhibited a much smaller lattice constants compared to those of films grown by PLD. For undoped $LiMn_2O_4$ film grown by UVPLD in the O_2 of 500 mtorr at 500°C lattice constant was 8.1672 Å, which is close to the value of oxygen-rich spinel [Tha92]. Due to the similarity of the peaks in XRDs, it is not easily distinguished a defective spinel from the stoichiometric spinel structure. Thus, further confirmation by XPS was required.

SEM micrographs of thin film cathodes grown by UVPLD are shown in Figure 6-4. Undoped $LiMn_2O_4$ film showed a relatively smooth and dense surface with small grains of fairly homogenous size in the range of 150 nm in length and 50 nm in width. $LiAl_xMn_{2-x}O_4$ (x= 0.1, 0.3) films showed uniform grains in shape and size of 50 ~ 70 nm but much less agglomeration than in Al-doped films grown by PLD.

Figure 6-5 shows the high resolution of Mn 2p peaks of undoped and Al-doped lithium manganese oxide films grown by UVPLD at 500°C. The Mn $2p_{3/2}$ peak was deconvoluted with three Gaussian peaks, which are shown as letter A, B, and C. As mention in chapter 4, the peaks at 641 ~ 641.3 eV and 642.2 ~ 642.8 eV can be assigned to Mn^{3+} and Mn^{4+}, respectively [DiC89, Eri02]. The peaks at 644.4 ~ 645 eV may represent either a higher oxidation state of manganese or peak related to impurities. By comparing the ratio of Mn^{3+} to Mn^{4+} the average oxidation state of Mn was determined. When compared with undoped and Al-doped thin film cathodes grown by PLD, the UVPLD films showed a higher content of Mn^{4+}, indicating that the average oxidation state of manganese was increased by the UV radiation. For example, the value n of Mn^{n+} was increased from 3.512 for undoped PLD film to 3.551 for undoped UVPLD film. For $LiAl_{0.1}Mn_{1.9}O_4$ films, the average oxidation state of manganese was increased by UVPLD from 3.517 to 3.624. Also, the relative atomic ratio of O/Mn for UVPLD films was larger than those form the films grown by PLD for both un-doped and Al-doped $LiMn_2O_4$. The ratio of O/Mn was increased from 2.046 for un-doped PLD film to 2.231 for undoped UVPLD film. The content of Mn^{3+} in the Al-doped lithium manganese oxide films grown by UVPLD was significantly decreased by the combination of replacement of Mn^{3+} by Al^{3+} and the more oxygen content by UV radiation. Thus, it can be concluded that UV radiation increased the content of oxygen in the films, leading to a higher oxidation state of manganese to maintain the charge neutrality.

From the smaller lattice constant, more oxygen content, and less content of Mn^{3+}, it is reasonable to note that lithium manganese oxide films grown by UVPLD might be identified as an oxygen-rich spinel($LiMn_2O_{4+\delta}$), which is also known as a defect spinel ($Li_{1-\delta}Mn_{2-2\delta}O_4$) with vacancies on tetragonal (8a) and octahedral (16d) sites. In this chapter, either formula was used to refer the thin film cathodes grown by UVPLD.

Electrochemical Characteristics

Electrochemical behavior of oxygen-rich spinel cathode of 2.5 ~ 3.5 V region

In order to ensure the electrochemical characteristics of oxygen-rich (defect) spinel a thin film cathode was grown by UVPLD in the O_2 of 500 mtorr at 400°C. It has been reported that oxygen-rich (defect) spinel was obtained at 400°C by reaction of Li_2CO_3 and $MnCO_3$ [Koc90, Tha92]. $LiMn_2O_{4+\delta}$ film grown by UVPLD at 400°C even showed a smaller lattice constant, larger average oxidation state of Mn, and larger O/Mn than the film grown by UVPLD at 500°C, indicating that the film grown at 400°C was much close to the oxygen-rich spinel compared with the film grown at higher temperature (500°C).

Figure 6-6 displays cyclic voltammogram for $LiMn_2O_{4+\delta}$ thin film grown by UVPLD at 400°C in 500 mtorr of oxygen between 2.5 and 3.5 V at various sweep rates of 0.1 ~ 1.6 mV/s. The 3 V process characterized by a peak at 2.8 V on discharge and a peak at 3.1 V on charge was obtained. The lithium insertion/extraction reaction appeared to be reversible in this potential range. The shape of the voltammogram was strongly dependent upon the sweep rate. An increase in sweep rate was correlated with a progressive shift of the anodic peaks to higher potential as well as increase in height. On contrary, the cathodic peaks were shifted to lower potential and the height of them was increased as the sweep rate is increased. This behavior is very similar to the results obtained previously for the films grown by PLD.

The discharge curves up to 100th cycle of $LiMn_2O_{4+\delta}$ thin film grown by UVPLD at 400°C is shown in Figure 6-7. Charge/discharge reactions were performed at 1 C rate of current density in the range of 2.5 ~ 3.5 V. The first discharge capacity was about 37.47 $\mu Ah/cm^2 \cdot \mu m$, which is larger than that of the film grown by PLD at the same temperature and oxygen pressure. The discharge capacity was increased until the 10th cycle because the cell might be stabilized during the first several cycles and then gradually decreased. At 100th cycle, the discharge capacity was about 98.11% of its initial capacity, which corresponds to the 0.0189% reduction in capacity per cycle from the initial discharge. $LiMn_2O_{4+\delta}$ thin film grown by UVPLD at 400°C showed 10 times higher rechargeability than the film grown by PLD at 400°C, which was 0.1805% per cycle.

An isothermal phase diagram of the Li-Mn-O is introduced to explain the higher capacity and capacity retention on cycling of oxygen-rich (defect) spinel film grown by UVPLD in Figure 6-8 [Tha92]. Stoichiometric spinel phases lie on the tie line between Mn_3O_4 and $Li_4Mn_5O_{12}$ while phases with a rock salt stoichiometry are located on the tie line between MnO and Li_2MnO_3. Manganese oxide defect spinels are located between Mn_3O_4 and λ-MnO_2 and lithium manganese oxide defect spinels are positioned on the line between $Li_4Mn_5O_{12}$ and λ-MnO_2. The dotted lines represent lithium insertion/extraction between spinel and rock salt stoichiometry. During the lithium insertion into spinel, the cations in the tetrahedral sites are cooperatively displaced by the inserted Li^+ ions into neighboring octahedral sites. Thus, the area I and II represent regions of defect spinel and defect rock salt structure, respectively. When oxygen-rich (defect) spinel $Li_2Mn_4O_9$ ($\delta = 0.5$ in $LiMn_2O_{4+\delta}$ or $\delta = 0.11$ in $Li_{1-\delta}Mn_{2-2\delta}O_4$) is discharged to rock salt $Li_5Mn_4O_9$, the theoretical discharge capacity at 3 V is 213 mAh/g [Koc90], which is much greater than 148 mAh/g for $LiMn_2O_4$ when it is discharged to the rock salt $Li_2Mn_2O_4$. The additional oxygen concentration, which creates defects on the tetrahedral (8a) and octahedral (16d) sites, gives $Li_2Mn_4O_9$ a significantly greater theoretical capacity than $LiMn_2O_4$. However, the utilizable reversible capacity in the range of 2.3 ~ 3.3 V region during cycle is limited to approximately 160 mAh/g because extraction of Li ions inserted during the first discharge requires a charge voltage higher than 4 V to regenerate the defect spinel $Li_2Mn_4O_9$ [Cho00, Tha92]. Therefore, it should be noted that the real initial discharge capacity of the oxygen-rich spinel at 3 V region (2.5 ~ 3.5 V) might have been greater than the initial discharge capacity obtained from the first cycle because the cathodic scan from the open circuit voltage to 2.5 V was firstly performed in the CV measurement even before cycling.

The complete discharge of the oxygen-rich spinel $Li_2Mn_4O_9$ to rock salt $Li_5Mn_4O_9$, in spinel notation can be represented as below;

$$[Li_{0.89}\square_{0.11}]_{8a}[Mn_{1.78}\square_{0.11}]_{16d}O_4 \xrightarrow{1.33\,Li} [Li_2]_{16c}[Mn_{1.78}Li_{0.22}]_{16d}O_4 \qquad (6.1)$$

The cubic symmetry is maintained until approximately 0.88 Li ions are inserted into $[Li_{0.89}\square_{0.11}]_{8a}[Mn_{1.78}\square_{0.11}]_{16d}O_4$. Further insertion of Li ions, which lowers the average oxidation state of manganese below 3.5, induces the Jahn-Teller distortion. In case of spinel $LiMn_2O_4$, it has been reported that the onset of Jahn-Teller effect is placed at even

$x = 0.08$ in $Li_{1+x}Mn_2O_4$ when Li ions are inserted into $LiMn_2O_4$ [Tha95]. In addition, the distortion due to the Jahn-Teller effect is not as pronounced in oxygen-rich (defect) spinel $Li_{2+x}Mn_4O_9$ ($c/a = 1.14$) as it is in $Li_{1+x}Mn_2O_4$ ($c/a = 1.16$) [Tha92].

It can be concluded that the higher discharge capacity of oxygen-rich spinel $LiMn_2O_{4+\delta}$ thin film grown by UVPLD than that of the film grown by PLD is attributed to the increased amount of Li intercalation due to the vacancies at both tetrahedral and octahedral sites. Improved capacity retention on cycling of the oxygen-rich spinel $LiMn_2O_{4+\delta}$ thin film grown by UVPLD with respect to thin film grown by PLD can be accounted by the higher average oxidation state of manganese, which can suppress and delay the onset of the Jahn-Teller distortion.

The discharge rate capability of $LiMn_2O_{4+\delta}$ thin film grown by UVPLD at 400°C was conducted at different charge/discharge current densities up to 10 C rate as shown in Figure 6-9. The films exhibited slightly lower rate capability than that of the film grown by PLD, indicating that it may have a lower diffusion coefficient of Li^+ and higher $R_{ct.}$ The details on diffusion coefficient of Li^+ and charge transfer will be reported later in CV and AC impedance measurements.

Cyclic voltammetry and discharge capacity of 2.5 ~ 3.5 V region

Figure 6-10 shows the cyclic voltammograms of the $LiAl_xMn_{2-x}O_{4+\delta}$ films ($x = 0$, 0.1, 0.2, 0.3) grown by UVPLD. The CVs were measured in the range of 2.5 ~ 3.5 V at the sweep rate of 0.1 mV/s. Each CV showed a pair of distinct anodic and cathodic peaks, which are located around 2.9 V and 2.7 V, respectively. Anodic peak and cathodic peak clearly reflect reversible oxidation and reduction reactions corresponding to lithium extraction and insertion, respectively.

The initial discharge curves of $LiAl_xMn_{2-x}O_{4+\delta}$ thin films (x = 0, 0.1, 0.2, 0.3) grown by UVPLD are shown in Figure 6-11. All cells with thin film cathodes were discharged in the range of 2.5 ~ 3.5 V at 1 C rate. The initial discharge potential was slightly decreased with increasing the amount of Al substituted. This potential drop with Al doping can be ascribed to the increase of free energy in the system due to the formation of strong Al-O bonding, leading to the stronger total metal-oxygen bonding in the structure. $LiAl_xMn_{2-x}O_{4+\delta}$ thin film cathodes delivered the initial discharge capacities of 49.54, 40.94, 36.32, and 30.26 $\mu Ah/cm^2 \cdot \mu m$ for x = 0, 0.1, 0.2, and 0.3. The first discharge capacities of the defect spinel cathodes grown by UVPLD were greater than those of spinel cathodes grown by PLD. Capability of accommodating more Li ions in vacant tetrahedral and octahedral sites in the defect spinel cathodes is found to be responsible for the increase in discharge capacity. The initial discharge capacities of these cells were decreased with increasing Al-substitution content because of a decrease in the amount of extractable Li ion in the spinel. For $LiAl_xMn_{2-x}O_{4+\delta}$ (x > 0), Al^{3+} replaced Mn^{3+} and the amount of Mn^{3+} in spinel was reduced by the increasing amount of Al^{3+}. Since Al^{3+} ions are not capable being oxidized in this potential range, the amount of removable Li^+ is determined by the amount of Mn^{3+} [Oik99].

Cycling behavior of 2.5 ~ 3.5 V region

Figure 6-12 shows the discharge curves of Li-ion cells with undoped and Al-doped defect spinel $LiAl_xMn_{2-x}O_{4+\delta}$ films grown by UVPLD at 500°C in 500 mtorr of oxygen; (a) x = 0, (b) x = 0.1, (c) x = 0.2, and (d) = 0.3. Charge/discharge were measured at 1 C rate in the range of 2.5 ~ 3.5 V. All defect spinel cathodes grown by UVPLD exhibited excellent capacity retention at 3 V region. After 100 cycles, they maintained the capacity about 90% of their initial discharge capacities. The discharge capacity of $LiMn_2O_{4+\delta}$ was decreased to 91.81% of its initial value after 20 cycles. After 100 cycles, this cathode retained about 89.53% of its initial capacity, which corresponds to the 0.1047% reduction in capacity per cycle. $LiAl_{0.1}Mn_{1.9}O_{4+\delta}$ and $LiAl_{0.2}Mn_{1.8}O_{4+\delta}$ maintained their capacity about 90.58 and 92.99% of their initial discharge capacity after 100 cycles. The reduction rates in capacity per cycle were 0.0942 and 0.0701 for $LiAl_{0.1}Mn_{1.9}O_{4+\delta}$ and $LiAl_{0.2}Mn_{1.8}O_{4+\delta}$, respectively. The discharge capacity of $LiAl_{0.3}Mn_{1.7}O_{4+\delta}$ was decreased to 89.58% of its initial value after 20th cycle but gradually increased to even higher than its initial capacity after 100 cycles. This unique behavior might be attributed to a combination effect of highly doped Al and oxygen-rich characteristics. However, the further investigation is needed to define mechanisms responsible for this behavior. The specific discharge capacities and relative capacities of $LiAl_xMn_{2-x}O_{4+\delta}$ thin film cathodes ($x = 0, 0.1, 0.2, 0.3$) grown by UVPLD upon cycling are shown in Figure 6-13 (a) and (b).

From the results of cycling, two important conclusions were drawn: 1) capacity retention of oxygen-rich spinel cathode by UVPLD was much higher than that of spinel cathode by PLD for the undoped and Al-doped lithium manganese oxide thin films. 2) Capacity retention on cycling of Al-doped thin film cathodes grown by UVPLD was increased with increasing Al-substitution content in spite of some reduction in the initial discharge capacity with respect to undoped thin film cathode grown at the same condition.

It has been reported that synthesis of the exact defect spinel of $Li_2Mn_4O_9$ is difficult and $Li_2O_4O_9$ decomposes at higher than 400°C into $LiMn_2O_4$ [Cho00, Xia97b]. However, the reactive oxygen species introduced by UV radiation during the film growth might help produce oxygen-rich spinel, which is not necessarily an exact $Li_2Mn_4O_9$, and increase the stability temperature for oxygen-rich spinel, resulting in a suppression of oxygen loss at even 500°C. Thus, the increased average oxidation state of manganese allows the oxygen-rich spinel to maintain its cubic symmetry to a higher amount of Li without or less Jahn-Teller distortion, leading to the improved capacity retention. For example, the onset of Jahn-Teller distortion occurs as 0.89 Li^+ is inserted into $[Li_{0.89}\square_{0.11}]_{8a}[Mn_{1.78}\square_{0.11}]_{16d}O_4$ while 0.08 Li^+ into $LiMn_2O_4$. For the Al-doped defect spinel films grown by UVPLD, the more enhanced oxidation state of manganese by substitution of Al^{3+} for Mn^{3+} might be responsible for the higher capacity retention relative to undoped defect spinel film grown by UVPLD. From the decrease in lattice constant with increase of Al doped shown in Figure 6-3, it was able to deduce that the average oxidation state of manganese gradually was increased in proportion to the augmentation of Al content for the films grown by UVPLD. XPS results also confirmed that relative ratio of Mn^{3+} to Mn^{4+} was decreased with increasing the mount of Al doped, indicating an increase of the average oxidation state of manganese.

AC impedance of 2.5 ~ 3.5 V region

AC impedance spectra at the open-circuit voltage of as-received $LiAl_xMn_{2-x}O_{4+\delta}$ (x = 0, 0.1, 0.2, 0.3) thin film cathodes grown by UVPLD are shown in Figure 6-14. The spectra showed a typical Nyquist plot in which the real and imaginary impedances are drawn as a function of the given frequency. It can be qualitatively concluded that the charge transfer resistance was increased with increasing amount of aluminum substituted because the diameter of semicircle in the high frequency region was increased with increasing x of $LiAl_xMn_{2-x}O_{4+\delta}$ films grown by UVPLD.

The details on fitting of the Nyquist plots obtained using the modified equivalent circuit are shown in the Appendix. Calculated values including charge transfer resistance (R_{ct}) and double layer capacitance (C_{dl}) are shown in the Table 6-1 with the calculated diffusion coefficients using the Randles-Sevcik equation from the cyclic voltammetries [Ran48, Sev48].

Table 6-1. Parameters calculated from the AC impedance spectra of $LiAl_xMn_{2-x}O_{4+\delta}$ thin films grown by UVPLD.

x	0	0.1	0.2	0.3
R_Ω (Ωcm^2)	8.057 ± 0.26867	8.239 ± 0.27235	6.379 ± 0.30517	6.05 ± 0.29769
C_{dl}($\mu F/cm^2$)	2.6908 ± 0.5734	2.4504 ± 0.5425	2.8413 ± 0.7192	3.1480 ± 0.7790
R_{ct} (Ωcm^2)	70.47 ± 2.8855	79.45 ± 4.8578	88.13 ± 5.4238	102.4 ± 7.3694
D_{ch} (cm^2/s)	7.292×10^{-10}	2.424×10^{-10}	1.555×10^{-10}	6.316×10^{-11}
D_{disch} (cm^2/s)	6.961×10^{-10}	2.852×10^{-10}	1.916×10^{-10}	3.893×10^{-11}

There was no significant difference in the electrolyte resistance (R_Ω), which was in 6 ~ 8 Ωcm^2 for all films regardless of the amount of Al doped. The double layer capacitance was increased slightly with increasing of Al substituted from 2.6908 $\mu F/cm^2$ to 3.148 $\mu F/cm^2$ for x = 0 and x = 0.3 in $LiAl_xMn_{2-x}O_{4+\delta}$, respectively. The charge transfer resistance was increased with increasing Al-substitution content as expected from the Nyquist plot shown in Figure 6-14. The increment of R_{ct} with increasing the amount of aluminum can be mainly attributed to the increase in the repulsive interaction between lithium positive-positive ions at the surface of cathode contacted with the electrolyte because of the stronger total metal-oxygen bonding in the structure by substitution of aluminum. It should be noted that both R_Ω and R_{ct} of defect spinel thin films grown by UVPLD were smaller than those of films grown by PLD for undoped and Al-doped cathodes, indicating that increased vacancies at tetrahedral (8a) and octahedral (16d) sites by UV radiation decreased the interfacial resistance for charge transfer and repulsion between positive Li ions.

The diffusion coefficients of Li ions in the Al-doped defect spinel films were 2 ~ 10 times smaller than that of undoped defect spinel films and decreased with increasing the amount of aluminum doped. Figure 6-15 show the charge transfer resistance and diffusion coefficients of Li^+ as a function of x in $LiAl_xMn_{2-x}O_{4+\delta}$ thin film cathodes grown by UVPLD in 500 mtorr of oxygen at 500°C.The results of the defect spinel films are somewhat similar to that of Al-doped spinel films grown by PLD described in chapter 5. The reduction in diffusion coefficients of Li ions in the Al-doped defect spinel can be explained by changes in bonding energy between metal and oxygen bonding [Joh97, Myu01]. Since the stronger bonding of Al-O than that of Mn-O can lead to the restricted contraction and/or expansion of the structure, the intercalation/deintercalation of lithium ions into/from the structure could be affected by the limited crystal lattice contraction, though the structure was stabilized by the Al substitution. It is worth noting that Li^+ diffusion coefficients of the defect spinel films grown by UVPLD were smaller than those of spinel films grown PLD for both undoped and Al-doped lithium manganese oxide. The diffusion coefficient of Li^+ in the $LiMn_2O_{4+\delta}$ film grown by UVPLD was 6.961×10^{-10} cm^2/s whereas that of $LiMn_2O_4$ film grown by PLD was 3.033×10^{-9} cm^2/s. For aluminum doped spinel, the values of D were 3.893×10^{-11} cm^2/s and 1.227×10^{-10} cm^2/s for $LiAl_{0.1}Mn_{1.9}O_{4+\delta}$ by UVPLD and $LiAl_{0.1}Mn_{1.9}O_4$ by PLD, respectively. Unlike the spinel cathode at 3 V of which Li diffusion path has been know through 8a-16c-8a, the vacant 16d sites are added to the diffusion path of Li^+ in the defect spinel cathode

Some of the Li ions inserted at 16c and 16d sites on the first discharge might be remained during the following charge and partly close the lithium diffusion path, leading to the lower the diffusion coefficient of Li upon repeated cycles. It has been reported that although lithium can be inserted into empty 8a and 16d in the defect spinel during the first discharge, extraction of lithium ions from these sites during the subsequent charge requires much higher charge voltage than 4 V [Cho00, Koc90, Tha92]. Since the cutoff voltage was 3.5 V in this experiment, there must be lithium ions at the 16c and/or 16d sites on the following charge, which might limit the further lithium diffusion for the sequential discharge/charge reactions. Additionally, the much smaller unit cell of the defect spinel cathode might restrict the Li diffusion even though it is beneficial to stabilization of the structure upon cycling with a minimal expansion/contraction.

Rate capability of 2.5 ~ 3.5 V region

The discharge rate capability was conducted at different charge/discharge current densities after 50th cycle and discharge curves for the Li-ion cells with $LiAl_xMn_{2-x}O_{4+\delta}$ films in the range of 2.5 ~ 3.5 V are shown in Figure 6-16. As explained in chapter 4, it is evident that the average discharge potential of discharge curve was decreased with increasing the discharge current density applied because of the ohmic drop in the electrolyte and polarization due to an overpotential induced by the kinetic limitation. The discharge capacity of a thin film cathode was decreased with increasing current density. The degree of reduction in discharge capacity with increasing current density became greater as the value of x in $LiAl_xMn_{2-x}O_{4+\delta}$ thin films was increased from 0 to 0.3 shown in Figure 6-16 (a), (b), (c), and (d).

The relative capacity of defect thin film cathodes with increasing discharge current density up to 10 C rate is shown in Figure 6-17. All Al-doped defect spinel films exhibited the poorer rate capability than undoped defect spinel $LiMn_2O_{4+\delta}$ film. The capacities at 10 C rate were about 41%, 35%, 30% of the capacity at 1 C rate for x = 0.1, 0.2, and 0.3 in $LiAl_xMn_{2-x}O_{4+\delta}$ film, which is much less than that of undoped $LiMn_2O_{4+\delta}$ film (~ 50%).

The rate capability, which represents the ability to charge and discharge at high current required, of the thin film cathodes is strongly dependent upon both the charge transfer at the interface between electrode and electrolyte and the diffusion of Li^+ in the thin film cathodes. The higher diffusion coefficient of Li^+ and the lower R_{ct}, the higher discharge rate capability was obtained. Therefore, undoped defect spinel $LiMn_2O_{4+\delta}$ cathode with higher Li^+ diffusion coefficient and lower R_{ct} exhibited the higher rate capability than Al-doped defect cathodes. In addition, the rate capability of $LiAl_xMn_{2-x}O_{4+\delta}$ became poorer as the amount of aluminum substituted was increased because Li^+ diffusion coefficient was increased and R_{ct} was increased with increasing the amount of Al substituted. It should be noted that all defect spinel cathodes grown by UVPLD showed the lower rate capability than spinel cathodes grown by PLD even though they possessed the lower R_{ct}. It suggests that the diffusion of Li ions in the electrode is a predominant rate-determined step for charge/discharge at high current density because thin film cathodes, grown by PLD, with the higher diffusion coefficients of Li ions showed the higher rate capability than those grown by UVPLD.

Cyclic voltammetry of 2.5 ~ 4.5 V region

As performed in the previous chapter, the cells with defect spinel thin film cathodes grown by UVPLD were electrochemically characterized in the range of 2.5 ~ 4.5 V. The cyclic voltammetries of undoped and Al-doped defect spinel cathodes scanned at a sweep rate of 0.1 mV/s are shown in Figure 6-18. As shown in the 3 V region measurement, each cathode showed a distinct pair of anodic and cathodic peaks at 2.9 V and 2.7 V, respectively, indicating of the intercalation/deintercalation of Li^+ in the 3 V region. However, the two peaks on discharge at 4 V region for undoped and Al-doped defect spinel, which represent the two-phase reaction of $Li_{0.5}Mn_2O_4$ and λ-MnO_2 in undoped $LiMn_2O_4$ thin film cathode shown in Figure 4-18 (b), were disappeared. In addition, two anodic peaks of defect spinels $LiAl_xMn_{2-x}O_{4+\delta}$ were less distinctive compared with those of $LiAl_xMn_{2-x}O_4$ and became less pronounced with increasing the amount of Al doped. This feature suggests that the extraction of Li ions in defect spinels grown by UVPLD at 4 V region is not as readily as in the spinels grown by PLD. The number of extracted Li ions at 4 V region might be limited in the defect spinels, leading to very small capacity at the 4 V region out of 2.5 ~ 4.5 V cycling.

Discharge capacity and cycling behavior of 2.5 ~ 4.5 V region

The first discharge curves of $LiAl_xMn_{2-x}O_{4+\delta}$ (x = 0, 0.1, 0.2, 0.3) thin film cathodes grown by UVPLD are shown in Figure 6-19. Both charge and discharge were conducted at the same 1 C rate. No defect spinel cathodes exhibited two plateaus at 4 V region, which is in agreement with the results from cyclic voltammograms. In the 3 V region, the degree of flatness on the discharge curve was decreased with increasing the amount of Al doped, indicating that the Al^{3+} substitution for Mn^{3+} at 16d sites may help to maintain the structural integrity of cathode on charge/discharge resulting in a higher resistance to the phase transformation.

The initial discharge capacity of the defect spinel cathodes grown by UVPLD in the range of 2.5 ~ 4.5 V was higher than that of spinel cathodes grown by PLD for undoped and Al-doped lithium manganese oxide because of the higher capacity at 3 V region of the defect spinel cathode relative to the spinel cathode. Undoped defect spinel $LiMn_2O_{4+\delta}$ grown by UVPLD delivered about 82.31 $\mu Ah/cm^2 \cdot \mu m$ whereas undoped spinel $LiMn_2O_4$ grown by PLD delivered about 68.83 $\mu Ah/cm^2 \cdot \mu m$.

In defect spinel cathodes, the discharge capacity of 3 V out of 2.5 ~ 4.5 V charge/discharge showed the higher values compared with 3 V discharge capacity obtained from 2.5 ~ 3.5 V charge/discharge only. $LiMn_2O_{4+\delta}$ cathode initially delivered about 49.54 $\mu Ah/cm^2 \cdot \mu m$ during the discharge of 2.5 ~ 3.5 V while 60.95 $\mu Ah/cm^2 \cdot \mu m$ corresponded to the capacity of 2.5 ~ 3.5 V out of 2.5 ~ 4.5 V. It has been know that only fraction of Li ions inserted into the cathode during the first discharge in the range of 2.5 ~ 3.5 V measurement are involved in the following charge and discharge because the higher charge voltage than 3.5 V is required to extract all Li ions inserted [Cho00, Tha92]. Before our charge/discharge cycling measurement, the cathodic scan to 2.5 V for 2.5 ~ 3.5 V and anodic scan to 4.5 V for 2.5 ~ 4.5 V measurements were performed in the cyclic voltammetry. In the 2.5 ~ 3.5 V measurement, some of Li ions inserted into cathodes during the first cathodic scan might be remained and excluded from the following charge/discharge reactions, leading to smaller capacity. However, in the 2.5 ~ 4.5 V measurement, most of Li ions were extracted and contributed to the following charge/discharge reactions, resulting in higher capacity, due to the higher charge voltage

(4.5 V). The initial discharge capacity of 3 V region out of 2.5 ~ 4.5 V was decreased as the amount of Al increased, which is in a good accordance with the results from the cycling behavior performed in only 2.5 ~ 3.5 V region measurement.

The first discharge capacities at 4 V region out of 2.5 ~ 4.5 V of Al-doped defect thin film cathodes were less than that of undoped defect thin film cathode and decreased significantly with increasing the amount of Al substituted. This behavior may be ascribed to the same effect as mentioned for the spinels cathode grown by PLD in the previous chapter, which is a decrease in the Mn^{3+} amount available for the oxidation to Mn^{4+} by the substitution of Al^{3+} for Mn^{3+}. At $x = 0.3$, the initial discharge capacity of 4 V out of 2.5 ~ 4.5 V was close to a quarter of that obtained from the undoped defect spinel cathode. Therefore, the whole discharge capacity in the range of 2.5 ~ 4.5 V was decreased as Al was substituted. The initial discharge capacities of $LiAl_xMn_{2-x}O_{4+\delta}$ thin film cathodes grown by UVPLD in the range of 2.5 ~ 4.5 V for $x = 0, 0.1, 0.2, 0.3$ were 82.31, 65.61, 55.04, and 43.88 $\mu Ah/cm^2 \cdot \mu m$, respectively.

The discharge curves on cycling of $LiAl_xMn_{2-x}O_{4+\delta}$ thin film cathodes grown by UVPLD in the range of 2.5 ~ 4.5 V at 1 C rate are shown in Figure 6-20. From the results, it can be concluded that the capacity retention on cycling in the range of 2.5 ~ 4.5 V was improved for the defect spinel cathodes grown by UVPLD. For the defect spinel cathodes capacity fade on cycling was increased with increasing the amount of aluminum substituted with some sacrifice of initial discharge capacity. This behavior can be more clearly seen in Figure 6-21 (a) and (b) in which the specific and relative capacities of the $LiAl_xMn_{2-x}O_{4+\delta}$ thin film cathodes grown by UVPLD are shown up to 100th cycle. The undoped defect spinel $LiMn_2O_{4+\delta}$ thin film cathode in the range of 2.5 ~ 4.5 V exhibited the fastest capacity fade on cycling even though it delivered the highest discharge capacity. On the contrary, $LiAl_{0.3}Mn_{1.7}O_{4+\delta}$ showed the best capacity retention up to 100th cycle maintaining about 97% of its first capacity with the lowest initial discharge capacity of 43.88 μAh/cm^2·μm.

The improved capacity retention of the defect spinel thin film cathodes grown by UVPLD in the range of 2.5 ~ 4.5 V is attributed to the stabilized structure, resulting from the minimum volume change, suppression and/or delay of Jahn-Teller distortion, and homogeneous phase. For aluminum substitution, the increased bonding strength can be added to an impact on the stabilization of the structure, leading to the better capacity retention.

Summary

$LiAl_xMn_{2-x}O_{4+\delta}$ ($x = 0, 0.1, 0.2, 0.3$ and $\delta > 0$) thin film cathodes have been grown by UVPLD in the oxygen of 500 mtorr at 500°C. From the results of structural characterizations, the thin film cathodes grown with help of UV radiation were defect (oxygen-rich) spinel structure.

The initial discharge capacity of defect spinel $LiAl_xMn_{2-x}O_{4+\delta}$ thin film cathodes in the range of 2.5 ~ 3.5 V was greater than that of spinel $LiAl_xMn_{2-x}O_4$ thin film cathode because the cathode could accommodate more amount of Li^+ on vacant tetrahedral and octahedral sites, which is known as a characteristic of defect (oxygen-rich) spinel at 3 V region. For Al-doped defect spinels the discharge capacity was decreased as the value of x was increased because Al^{3+} reduced the content of Mn^{3+}, which determines the discharge capacity. The capacity retention upon cycling of the defect spinel cathodes in the 3 V region was higher than that of spinel cathode for undoped and Al-doped spinel. It might be due to the increase in the average oxidation state of manganese, resulting in the restriction or delay of the Jahn-Teller distortion, which has been known as a major mechanism for capacity fade in the 3 V region. Increased capacity retention of Al-doped defect spinel is also attributed to the increased average oxidation state of Mn and stronger bonding strength of the metal-oxygen frame structure.

The rate capability of the defect spinel cathodes at 3 V region was lower than that of the spinel cathodes and decreased with increasing the amount of Al substituted because of lower diffusion coefficient of Li ions, resulting from the interruption the path by the increased amount of Li ion itself.

The initial discharge capacity of defect spinel $LiAl_xMn_{2-x}O_{4+\delta}$ thin film cathodes by UVPLD in the range of 2.5 ~ 4.5 V was higher than that of spinel $LiMn_2O_4$ thin film cathodes by PLD and decreased with increasing the amount of Al doped. The capacity retention upon cycling of defect spinel cathodes was greater than that of spinel cathodes and increased with increasing the amount of Al doped. It is considered that the improved capacity retention of defect thin film cathodes at 2.5 ~ 4.5 V region is mainly due to the stabilized structure, suppression and/or delay of Jahn-Teller distortion, and homogeneous phase. For aluminum substitution, the increased structural stability can lead to the better electrochemical reversibility. In summary, the electrochemical properties of the defect spinel thin film cathodes grown by UVPLD in the range of 2.5 ~ 4.5 V were strongly dependent upon those at the 3 V region in terms of discharge capacity and capacity fading behavior.

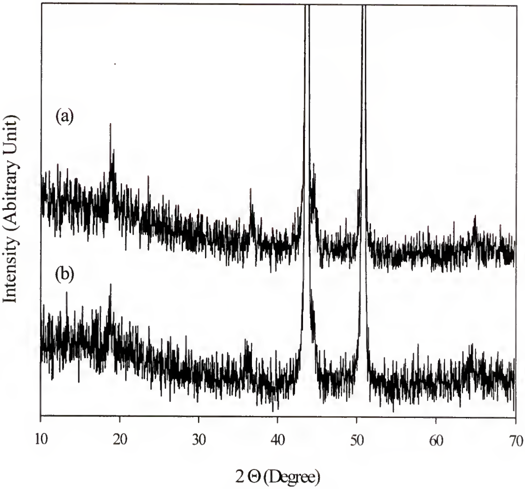

Figure 6-1. XRD of $LiMn_2O_4$ thin films grown in 500 mtorr of O_2 at 500°C by (a) UVPLD and (b) PLD.

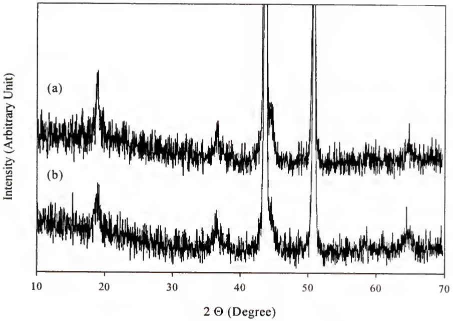

Figure 6-2. XRD of $LiAl_{0.2}Mn_{1.8}O_4$ thin films grown in 500 mtorr of O_2 at 500°C by (a) UVPLD and (b) PLD.

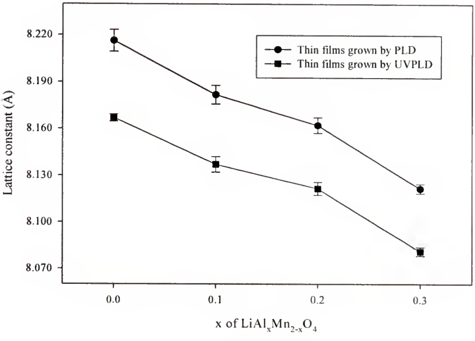

Figure 6-3. Lattice constants of $LiAl_xMn_{2-x}O_4$ thin films grown in 500 mtorr of O_2 at 500°C by PLD and UVPLD.

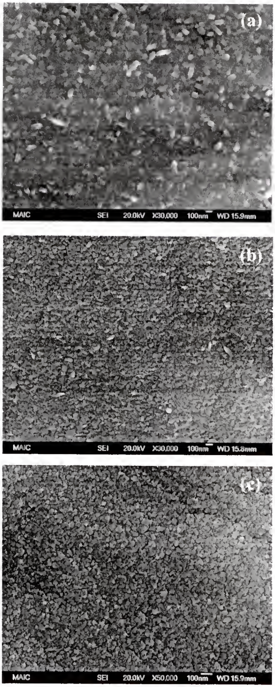
(a)
MAIC SEI 20.0kV X30,000 100nm WD 15.9mm
(b)
MAIC SEI 20.0kV X30,000 100nm WD 15.8mm
(c)
MAIC SEI 20.0kV X50,000 100nm WD 15.9mm

Figure 6-4. SEM micrographs of (a) $LiMn_2O_4$, (b) $LiAl_{0.1}Mn_{1.9}O_4$ and (c) $LiAl_{0.3}Mn_{1.7}O_4$ thin films grown by UVPLD in 500 mtorr of O_2 at 500°C.

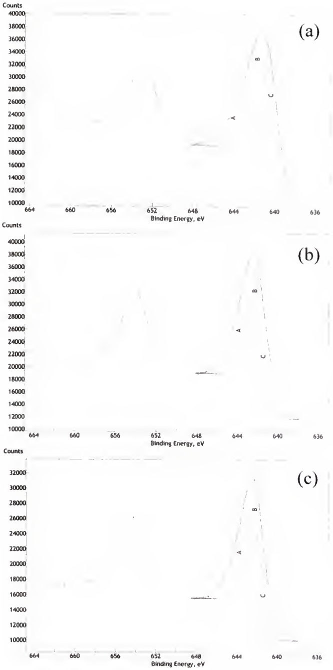

Figure 6-5. High resolution XPS of Mn $2p_{3/2}$ of thin films grown in 500 mtorr of O_2 at 500°C by UVPLD: (a) $LiMn_2O_4$, (b) $LiAl_{0.1}Mn_{1.9}O_4$, and (c) $LiAl_{0.3}Mn_{1.7}O_4$.

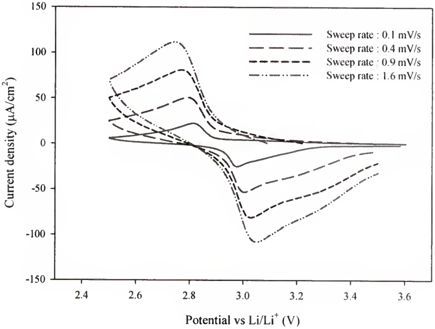

Figure 6-6. Cyclic voltammograms in the range of 2.5 ~ 3.5 V of $LiMn_2O_{4+\delta}$ thin film grown by UVPLD in 500 mtorr of O_2 at 400°C.

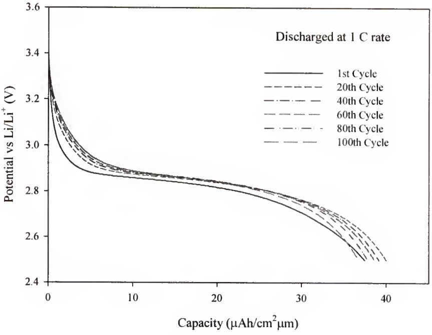

Figure 6-7. Discharge curves in the range of 2.5 ~ 3.5 V of $LiMn_2O_{4+\delta}$ thin film grown by UVPLD in 500 mtorr of O_2 at 400°C.

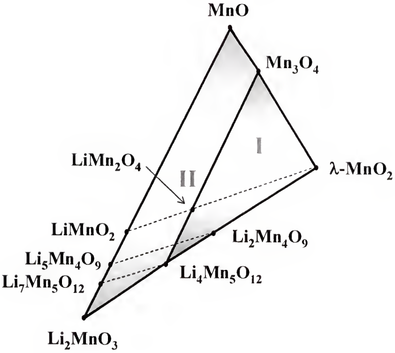

Figure 6-8. An isothermal cross section of the Li-Mn-O phase diagram at 20°C; Area I and II represent regions of defect spinel and defect rock salt phases, respectively [Tha92].

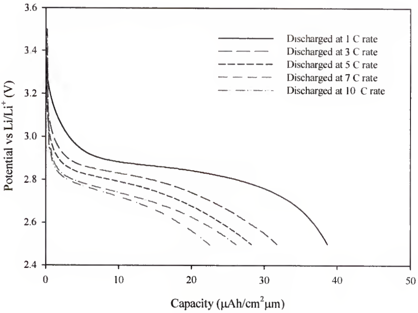

Figure 6-9. Discharge curves at different current densities of $LiMn_2O_{4+\delta}$ thin films grown by UVPLD in 500 mtorr of O_2 at 400°C.

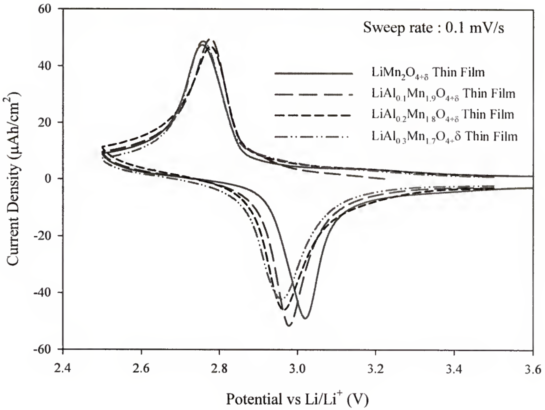

Figure 6-10. Cyclic voltammograms in the range of 2.5 ~ 3.5 V of $LiAl_xMn_{2-x}O_{4+\delta}$ (x = 0, 0.1, 0.2, 0.3) thin films grown by UVPLD in 500 mtorr of O_2 at 500°C.

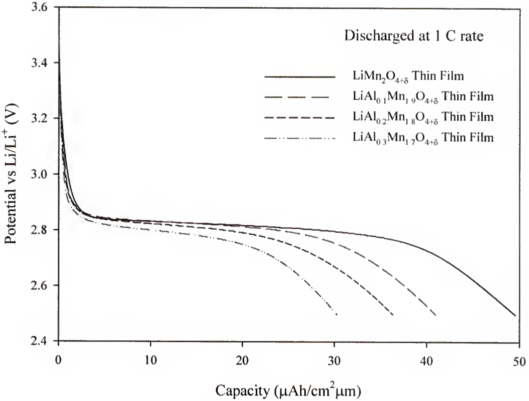

Figure 6-11. The first discharge curves in the range of 2.5 ~ 3.5 V of LiAl$_x$Mn$_{2-x}$O$_{4+\delta}$ thin films grown by UVPLD in 500 mtorr of O_2 at 500°C.

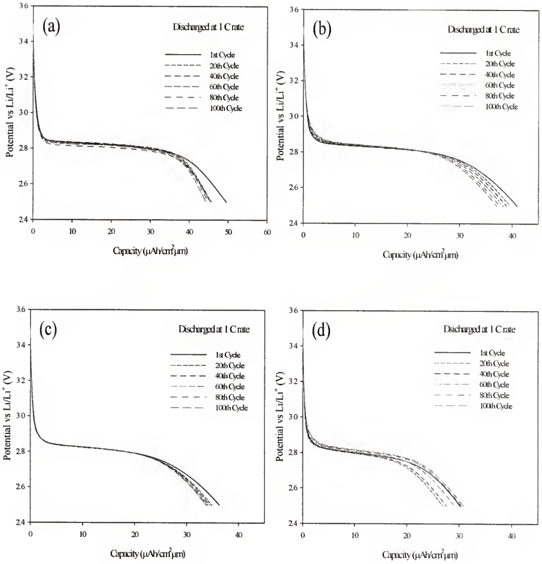

Figure 6-12. Discharge curves in the range of 2.5 ~ 3.5 V of $LiAl_xMn_{2-x}O_{4+\delta}$ thin films grown by UVPLD in 500 mtorr of O2 at 500°C: (a) x = 0, (b) x = 0.1, (c) x = 0.2, and (d) x = 0.3.

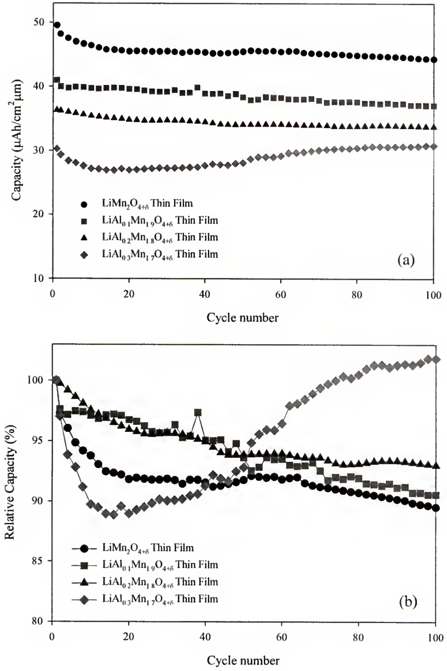

Figure 6-13. Discharge capacity in the range of 2.5 ~ 3.5 V of $LiAl_xMn_{2-x}O_{4+\delta}$ thin films grown by UVPLD in 500 mtorr of O_2 at 500°C: (a) Specific discharge capacity and (b) Relative discharge capacity.

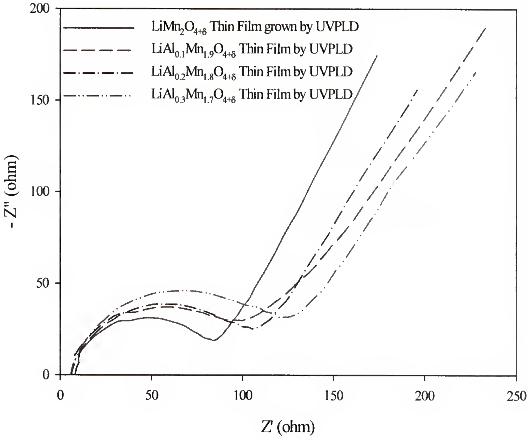

Figure 6-14. AC impedance spectroscopies of LiAl$_x$Mn$_{2-x}$O$_{4+\delta}$ thin films grown by UVPLD in 500 mtorr of O$_2$ at 500°C.

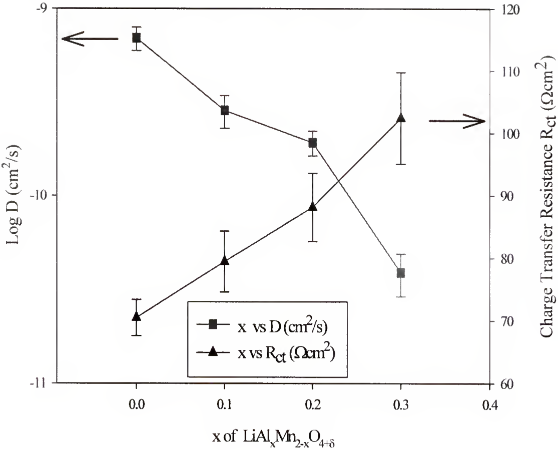

Figure 6-15. Diffusion coefficients of Li on discharge (left) and charge transfer resistances (right) as a function of x in $LiAl_xMn_{2-x}O_{4+\delta}$ thin films grown by UVPLD in 500 mtorr of O_2 at 500°C.

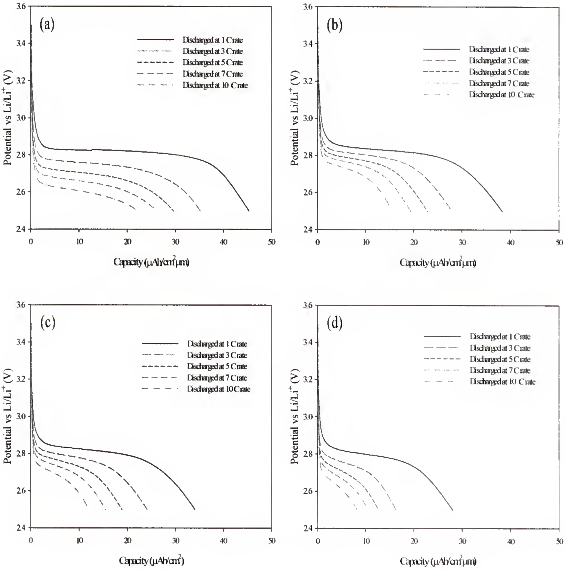

Figure 6-16. Discharge curves at different current densities of $LiAl_xMn_{2-x}O_{4+\delta}$ thin films grown by UVPLD in 500 mtorr of O_2 at 500°C: (a) x = 0, (b) x = 0.1, (c) x = 0.2, and (d) x = 0.3.

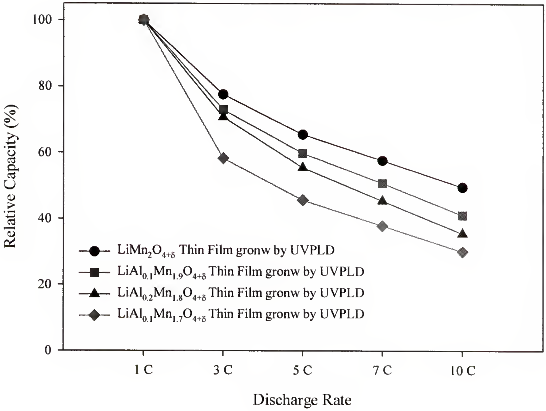

Figure 6-17. Discharge rate capability in the range of 2.5 ~ 3.5 V of LiAl$_x$Mn$_{2-x}$O$_{4+\delta}$ thin films grown by UVPLD in 500 mtorr of O_2 at 500°C.

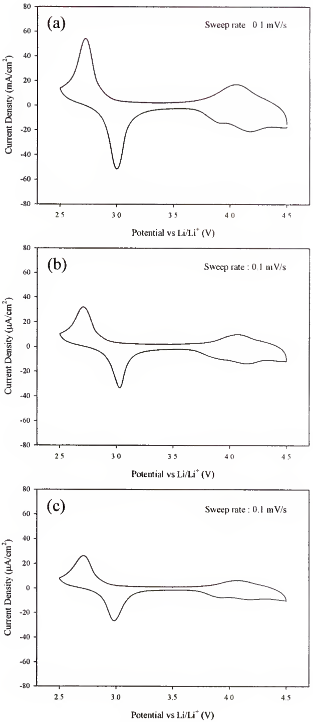

Figure 6-18. Cyclic voltammograms in the range of 2.5 ~ 4.5 V of $LiAl_xMn_{2-x}O_{4+\delta}$ thin films grown by UVPLD in 500 mtorr of O_2 at 500°C: (a) x = 0, (b) x = 0.2, and (c) x = 0.3.

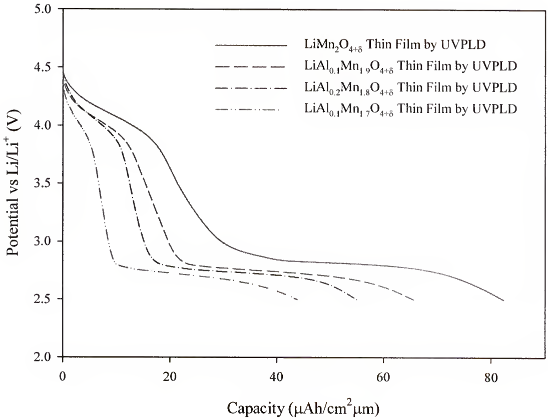

Figure 6-19. The first discharge curves in the range of 2.5 ~ 4.5 V of $LiAl_xMn_{2-x}O_{4+\delta}$ thin films grown by UVPLD in 500 mtorr of O_2 at 500°C.

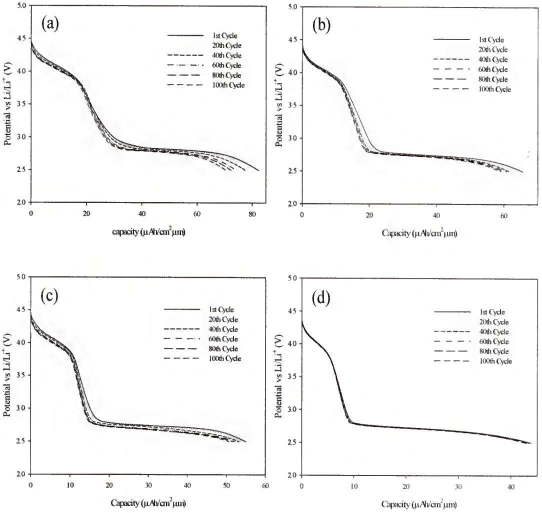

Figure 6-20. Discharge curves in the range of 2.5 ~ 4.5 V of (a) $LiMn_2O_{4+\delta}$, (b) $LiAl_{0.1}Mn_{1.9}O_{4+\delta}$, (c) $LiAl_{0.2}Mn_{1.8}O_{4+\delta}$, and (d) $LiAl_{0.3}Mn_{1.7}O_{4+\delta}$ thin films grown by UVPLD in 500 mtorr of O_2 at 500°C. Discharged at 1 C rate.

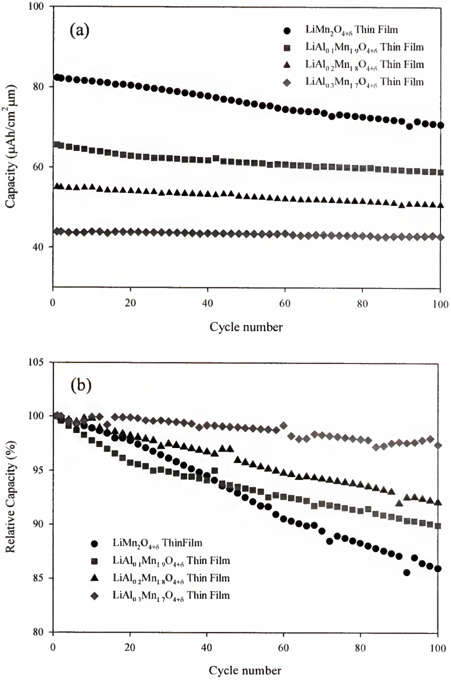

Figure 6-21. Discharge capacity in the range of 2.5 ~ 4.5 V of $LiAl_xMn_{2-x}O_{4+\delta}$ thin films grown by UVPLD in 500 mtorr of O_2 at 500°C: (a) Specific discharge capacity and (b) Relative discharge capacity.

CHAPTER 7
CONCLUSIONS

Using pulsed laser deposition technique the electrochemical properties of $LiMn_2O_4$ thin film cathode have been investigated as a function of growth temperature, aluminum substitution, and UV radiation.

The initial discharge capacity of 3 V region was increased with increasing substrate temperature in the range of 300°C ~ 500°C and then decreased at higher temperatures. The main reason for the increment of the initial discharge capacity was ascribed to the increase of amount of Mn^{3+} and improved crystallinity with temperature leading to facilitated intercalation and deintercalation of lithium. The inhomogeneous electrochemical reaction due to the abnormally agglomerated grains and high contact resistance was responsible for the lower capacity of the thin film cathodes grown at high temperatures.

Capacity retention on cycling in the 3 V region was decreased with increasing temperature. Jahn-Teller distortion became a predominant contribution to the capacity loss with increasing temperature. The films grown at relatively low temperature exhibited the better capacity retention because structural defects and uniform distribution of grains might help to retain the structural integrity upon repeated cycling.

Thin film cathodes with high diffusion coefficient of Li^+ and low charge transfer resistance exhibited the better discharge rate capability. The highest rate capability was obtained from the thin film cathode grown at 500°C, which exhibited the highest diffusion coefficient of Li^+ and lowest R_{ct}.

The discharge capacity of 3 V was larger than that of 4 V for the films grown at 300°C and 500°C. The discharge capacity of 2.5 ~ 4.5 V was increased with increasing temperature because of increased capacities at both 3 V and 4 V with increasing temperature. The total capacity retention of 2.5 ~ 4.5 V for film grown at 500°C was better than that for grown at 300°C due to the poorer capacity retention at 3 V of the latter.

$LiAl_xMn_{2-x}O_4$ ($x = 0.1, 0.2, 0.3$) thin film cathodes showed that there was no impurity phase other than a cubic spinel phase as $LiMn_2O_4$.

The initial discharge capacity of $LiAl_xMn_{2-x}O_4$ thin film cathodes in the range of 2.5 ~ 3.5 V was less than that of undoped $LiMn_2O_4$ thin film cathode and decreased with increasing the amount of Al doped because the content of Mn^{3+}, which determines the discharge capacity, was reduced by Al substitution. However, the capacity retention upon cycling in the 3 V region was increased with increasing Al substitution content. It was ascribed to the increase in the average oxidation state of manganese resulting in the restriction or delay of Jahn-Teller distortion.

The charge transfer resistance was increased with increasing Al substitution content since Al doping induces the increment of interaction energy of the cathode. The diffusion coefficient of Li^+ in the cathode was decreased with increasing the amount of Al substituted. Therefore, the rate capability of Al-doped lithium manganese oxide thin film cathode was lower than that of undoped thin film cathode and decreased with increase in the amount of Al doped.

The initial discharge capacity of $LiAl_xMn_{2-x}O_4$ thin film cathodes in the range of 2.5 ~ 4.5 V was less than that of undoped $LiMn_2O_4$ thin film cathode and decreased with increasing the amount of Al doped. The initial discharge capacities at 4 V region out of 2.5 ~ 4.5 V of Al-doped thin film cathodes were less than that of undoped thin film cathode and decreased significantly with increasing the amount of Al substituted because of the decrease in the Mn^{3+} amount available for the oxidation to Mn^{4+} by the substitution of Al^{3+} for Mn^{3+}. However, the capacity retention upon cycling was higher than that of undoped $LiMn_2O_4$ thin film cathode and increased with increasing the amount of Al doped. It is considered that the improved capacity retention of Al-doped $LiMn_2O_4$ thin film cathodes at 4 V region is due to the stronger bonding between aluminum and oxygen in the framework structure leading to the increased structural stability, which can prevent unstable two-phase transition and severe dissolution of manganese into the electrolyte. The rechargeability of $LiMn_2O_4$ thin film cathode at both 3 and 4 V regions was enhanced when Al^{3+} was substituted for Mn^{3+} in spite of some sacrifice of the discharge capacity. It is reasonable to note that Al doping suppresses the Jahn-Teller distortion and increases the stability of cathode to maintain the structural integrity during repeated intercalation/deintercalation of lithium, resulting in higher capacity retention.

$LiAl_xMn_{2-x}O_{4+\delta}$ ($x = 0, 0.1, 0.2, 0.3$ and $\delta > 0$) thin film cathodes have been grown by UVPLD in the oxygen of 500 mtorr at 500°C. From the results of structural characterizations, the thin film cathodes grown with help of UV radiation were defect (oxygen-rich) spinel structure.

The initial discharge capacity of defect spinel $LiAl_xMn_{2-x}O_{4+\delta}$ thin film cathodes in the range of 2.5 ~ 3.5 V was greater than that of spinel $LiAl_xMn_{2-x}O_4$ thin film cathode because the cathode could accommodate more amount of Li^+ on vacant tetrahedral and octahedral sites. For Al-doped defect spinels the discharge capacity was decreased as the amount of aluminum doped was increased because Al^{3+} reduced the content of Mn^{3+}, which determines the discharge capacity. The capacity retention upon cycling of the defect spinel cathodes in the 3 V region was higher than that of spinel cathode for undoped and Al-doped spinel. The increase in the average oxidation state of manganese resulted in the restriction or delay of the Jahn-Teller distortion. The higher capacity retention of Al-doped defect spinels than undoped defect spinel is also attributed to the increased average oxidation state of Mn and stronger bonding strength of the metal-oxygen frame structure.

The rate capability of the defect spinel cathodes at 3 V region was lower than that of the spinel cathodes and decreased with increasing the amount of Al substituted because of lower diffusion coefficient of Li ions, resulting from the interruption the path by the increased amount of Li ion itself.

The initial discharge capacity of defect spinel $LiAl_xMn_{2-x}O_{4+\delta}$ in the range of 2.5 ~ 4.5 V was higher than that of spinel $LiMn_2O_4$ and decreased with increasing the amount of Al doped. The capacity retention upon cycling of defect spinel cathodes was greater than that of spinel cathodes and increased with increasing the amount of Al doped. It is considered that the improved capacity retention of defect spinel at 2.5 ~ 4.5 V region is mainly due to the stabilized structure, suppression and/or delay of Jahn-Teller distortion, and homogeneous phase. For aluminum substitution, the increased structural stability can lead to the better electrochemical reversibility.

APPENDIX
FITTING OF THE AC IMPEDANCE

In this Appendix, the fitting of alternative current impedance spectroscopy obtained from each cell has been included. The equivalent circuit based on the Rundles circuit, the fitted data, and curve are shown together.

(1) $LiMn_2O_4$ grown at 300°C in the oxygen of 500 mtorr

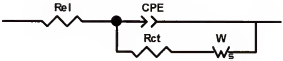

Element	Freedom	Value	Error	Error %
Rel	Free(+)	14.97	0.10685	0.71376
CPE-T	Free(+)	1.0543E-5	1.0146E-6	9.6234
CPE-P	Free(+)	0.87057	0.0099122	1.1386
Rct	Free(+)	36.66	0.66677	1.8188
W-R	Free(+)	335.9	313.59	93.358
W-T	Free(+)	1.533	2.7441	179
W-P	Free(+)	0.53589	0.011083	2.0681

Chi-Squared:	0.00045023
Weighted Sum of Squares:	0.013957
Data File:	~Clipboard
Circuit Model File:	C:\Program Files\SAI_Demo\ZModels\AppendixC LI
Mode:	Run Fitting / All Data Points (1 - 19)
Maximum Iterations:	100
Optimization Iterations:	0
Type of Fitting:	Complex
Type of Weighting:	Calc-Modulus

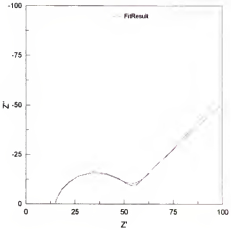

Figure A-1. Fitting of AC Impedance of $LiMn_2O_4$ thin film grown at 300°C in the oxygen 500 mtorr.

(2) $LiMn_2O_4$ grown at 400°C in the oxygen of 500 mtorr

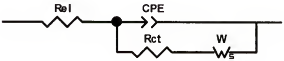

Element	Freedom	Value	Error	Error %
Rel	Free(+)	5.736	0.31367	5.4684
CPE-T	Free(+)	6.1239E-6	2.1383E-6	34.917
CPE-P	Free(+)	0.9337	0.035092	3.7584
Rct	Free(+)	69.66	7.2125	10.354
W-R	Free(+)	349.8	190.24	54.385
W-T	Free(+)	0.45671	0.40349	88.347
W-P	Free(+)	0.52258	0.056898	10.888

Chi-Squared: 0.02025
Weighted Sum of Squares: 0.62776

Data File: ~Clipboard
Circuit Model File: C:\Program Files\SAI_Demo\ZModels\AppendixC C
Mode: Run Fitting / All Data Points (1 - 19)
Maximum Iterations: 100
Optimization Iterations: 0
Type of Fitting: Complex
Type of Weighting: Calc-Modulus

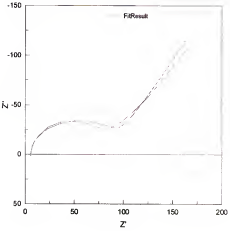

Figure A-2. Fitting of AC Impedance of $LiMn_2O_4$ thin film grown at 400°C in the oxygen 500 mtorr.

(3) $LiMn_2O_4$ grown at 500°C in the oxygen of 500 mtorr

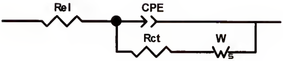

Element	Freedom	Value	Error	Error %
Rel	Free(+)	7.733	0.29663	3.8359
CPE-T	Free(+)	5.4992E-6	1.315E-6	23.913
CPE-P	Free(+)	0.90054	0.023791	2.6419
Rct	Free(+)	66.71	3.0044	4.5037
W-R	Free(+)	286.7	55.212	19.258
W-T	Free(+)	0.31879	0.08105	25.424
W-P	Free(+)	0.59393	0.028422	4.7854

Chi-Squared:	0.0080954
Weighted Sum of Squares:	0.25096
Data File:	~Clipboard
Circuit Model File:	C:\Program Files\SAI_Demo\ZModels\AppendixC C
Mode:	Run Fitting / All Data Points (1 - 19)
Maximum Iterations:	100
Optimization Iterations:	0
Type of Fitting:	Complex
Type of Weighting:	Calc-Modulus

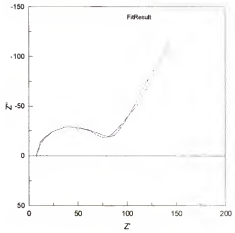

Figure A-3. Fitting of AC Impedance of $LiMn_2O_4$ thin film grown at 500°C in the oxygen 500 mtorr.

(4) $LiMn_2O_4$ grown at 600°C in the oxygen of 500 mtorr

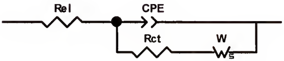

Element	Freedom	Value	Error	Error %
Rel	Free(+)	6.982	0.26895	3.852
CPE-T	Free(+)	1.4164E-5	2.6866E-6	18.968
CPE-P	Free(+)	0.875	0.020833	2.3809
Rct	Free(+)	310.3	44.818	14.443
W-R	Free(+)	1673	520.22	31.095
W-T	Free(+)	0.36719	0.15678	42.697
W-P	Free(+)	0.5826	0.050259	8.6267

Chi-Squared: 0.011527
Weighted Sum of Squares: 0.35734

Data File: ~Clipboard
Circuit Model File: C:\Program Files\SAI_Demo\ZModels\AppendixC C
Mode: Run Fitting / All Data Points (1 - 19)
Maximum Iterations: 100
Optimization Iterations: 0
Type of Fitting: Complex
Type of Weighting: Calc-Modulus

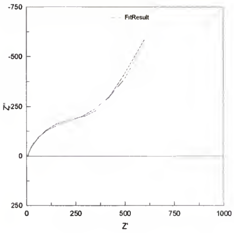

Figure A-4. Fitting of AC Impedance of LiMn$_2$O$_4$ thin film grown at 600°C in the oxygen 500 mtorr.

(5) LiMn$_2$O$_4$ grown at 700°C in the oxygen of 500 mtorr

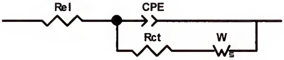

Element	Freedom	Value	Error	Error %
Rel	Free(+)	8.83	0.26774	3.0322
CPE-T	Free(+)	1.4018E-5	1.8036E-6	12.866
CPE-P	Free(+)	0.82488	0.01393	1.6887
Rct	Free(+)	395.5	32.36	8.182
W-R	Free(+)	1753	326.19	18.608
W-T	Free(+)	0.32795	0.078445	23.92
W-P	Free(+)	0.60607	0.032382	5.3429

Chi-Squared:	0.0050397
Weighted Sum of Squares:	0.15623
Data File:	~Clipboard
Circuit Model File:	C:\Program Files\SAI_Demo\ZModels\AppendixC C
Mode:	Run Fitting / All Data Points (1 - 19)
Maximum Iterations:	100
Optimization Iterations:	0
Type of Fitting:	Complex
Type of Weighting:	Calc-Modulus

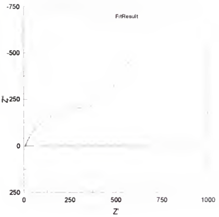

Figure A-5. Fitting of AC Impedance of $LiMn_2O_4$ thin film grown at 700°C in the oxygen 500 mtorr.

(6) $LiAl_{0.1}Mn_{1.9}O_4$ grown at 500°C in the oxygen of 500 mtorr

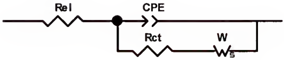

Element	Freedom	Value	Error	Error %
Rel	Free(+)	10.23	0.22034	2.1539
CPE-T	Free(+)	9.1545E-6	9.7369E-7	10.636
CPE-P	Free(+)	0.82425	0.010862	1.3178
Rct	Free(+)	162.7	5.3333	3.278
W-R	Free(+)	617.4	115.63	18.729
W-T	Free(+)	0.44124	0.11128	25.22
W-P	Free(+)	0.57393	0.025519	4.4464

Chi-Squared: 0.0019958
Weighted Sum of Squares: 0.061871

Data File: ~Clipboard
Circuit Model File: C:\Program Files\SAI_Demo\ZModels\AppendixC C
Mode: Run Fitting / All Data Points (1 - 19)
Maximum Iterations: 100
Optimization Iterations: 0
Type of Fitting: Complex
Type of Weighting: Calc-Modulus

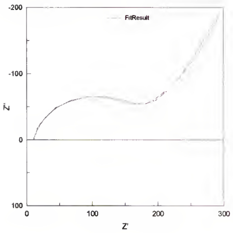

Figure A-6. Fitting of AC Impedance of $LiAl_{0.1}Mn_{1.9}O_4$ thin film grown at 500°C in the oxygen 500 mtorr.

(7) $LiAl_{0.2}Mn_{1.8}O_4$ grown at 500°C in the oxygen of 500 mtorr

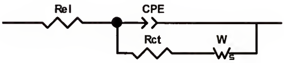

Element	Freedom	Value	Error	Error %
Rel	Free(+)	8.302	0.27188	3.2749
CPE-T	Free(+)	8.9202E-6	1.1942E-6	13.388
CPE-P	Free(+)	0.82505	0.013575	1.6454
Rct	Free(+)	200.6	9.4482	4.71
W-R	Free(+)	580	115.04	19.834
W-T	Free(+)	0.33519	0.10246	30.568
W-P	Free(+)	0.55269	0.029531	5.3431

Chi-Squared: 0.0039417
Weighted Sum of Squares: 0.12219

Data File: ~Clipboard
Circuit Model File: C:\Program Files\SAI_Demo\ZModels\AppendixC C
Mode: Run Fitting / All Data Points (1 - 19)
Maximum Iterations: 100
Optimization Iterations: 0
Type of Fitting: Complex
Type of Weighting: Calc-Modulus

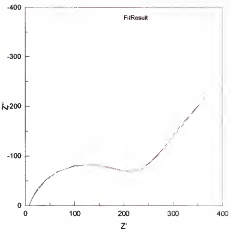

Figure A-7. Fitting of AC Impedance of $LiAl_{0.2}Mn_{1.8}O_4$ thin film grown at 500°C in the oxygen 500 mtorr.

(8) $LiAl_{0.3}Mn_{1.7}O_4$ grown at 500°C in the oxygen of 500 mtorr

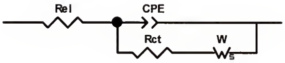

Element	Freedom	Value	Error	Error %
Rel	Free(+)	8.973	0.28154	3.1376
CPE-T	Free(+)	9.475E-6	1.416E-6	14.945
CPE-P	Free(+)	0.81954	0.014979	1.8277
Rct	Free(+)	215.7	18.962	8.7909
W-R	Free(+)	432.1	303.73	70.292
W-T	Free(+)	0.7855	1.3574	172.81
W-P	Free(+)	0.40203	0.063403	15.771

Chi-Squared:	0.0039959
Weighted Sum of Squares:	0.12387

Data File:	~Clipboard
Circuit Model File:	C:\Program Files\SAI_Demo\ZModels\AppendixC C
Mode:	Run Fitting / All Data Points (1 - 19)
Maximum Iterations:	100
Optimization Iterations:	0
Type of Fitting:	Complex
Type of Weighting:	Calc-Modulus

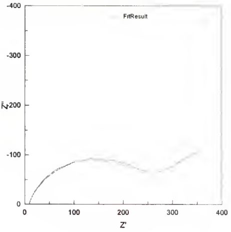

Figure A-8. Fitting of AC Impedance of $LiAl_{0.3}Mn_{1.7}O_4$ thin film grown at 500°C in the oxygen 500 mtorr.

(9) $LiMn_2O_{4+\delta}$ grown by UVPLD at 500°C in the oxygen of 500 mtorr

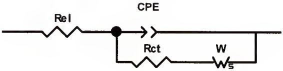

Element	Freedom	Value	Error	Error %
Rel	Free(+)	8.057	0.26867	3.3346
Cct-T	Free(+)	5.7969E-6	1.2353E-6	21.31
Cct-P	Free(+)	0.90669	0.021488	2.3699
Rct	Free(+)	70.47	2.8855	4.0947
W-R	Free(+)	324.4	59.477	18.334
W-T	Free(+)	0.34132	0.074656	21.873
W-P	Free(+)	0.61753	0.028892	4.6786

Chi-Squared:	0.007008
Weighted Sum of Squares:	0.21725
Data File:	~Clipboard
Circuit Model File:	C:\Program Files\SAI_Demo\ZModels\AppendixC Cc
Mode:	Run Fitting / All Data Points (1 - 19)
Maximum Iterations:	100
Optimization Iterations:	0
Type of Fitting:	Complex
Type of Weighting:	Calc-Modulus

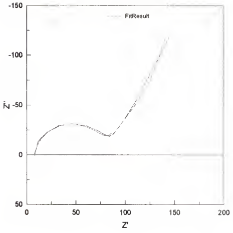

Figure A-9. Fitting of AC Impedance of $LiMn_2O_{4+\delta}$ thin film grown by UVPLD at 500°C in the oxygen 500 mtorr.

(10) $LiAl_{0.1}Mn_{1.9}O_{4+\delta}$ grown by UVPLD at 500°C in the oxygen of 500 mtorr

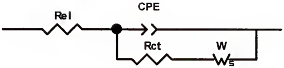

Element	Freedom	Value	Error	Error %
Rel	Free(+)	8.239	0.27235	3.3056
Cct-T	Free(+)	5.3557E-6	1.1856E-6	22.137
Cct-P	Free(+)	0.90291	0.021956	2.4317
Rct	Free(+)	79.45	4.8578	6.1143
W-R	Free(+)	464.8	172.73	37.162
W-T	Free(+)	0.53437	0.32192	60.243
W-P	Free(+)	0.51907	0.03361	6.475

Chi-Squared: 0.0058929
Weighted Sum of Squares: 0.18268

Data File: ~Clipboard
Circuit Model File: C:\Program Files\SAI_Demo\ZModels\AppendixC C
Mode: Run Fitting / All Data Points (1 - 19)
Maximum Iterations: 100
Optimization Iterations: 0
Type of Fitting: Complex
Type of Weighting: Calc-Modulus

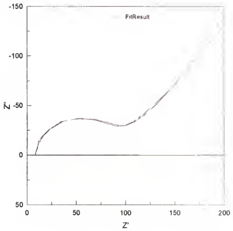

Figure A-10. Fitting of AC Impedance of $LiAl_{0.1}Mn_{1.9}O_{4+\delta}$ thin film grown by UVPLD at 500°C in the oxygen 500 mtorr.

(11) $LiAl_{0.2}Mn_{1.8}O_{4+\delta}$ grown by UVPLD at 500°C in the oxygen of 500 mtorr

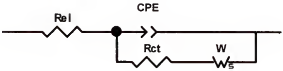

Element	Freedom	Value	Error	Error %
Rel	Free(+)	6.379	0.30517	4.784
Cct-T	Free(+)	6.4635E-6	1.6361E-6	25.313
Cct-P	Free(+)	0.89588	0.025351	2.8297
Rct	Free(+)	88.13	5.4238	6.1543
W-R	Free(+)	306.4	115.39	37.66
W-T	Free(+)	0.3884	0.20494	52.765
W-P	Free(+)	0.56777	0.04904	8.6373

Chi-Squared:	0.012647
Weighted Sum of Squares:	0.39207

Data File:	~Clipboard
Circuit Model File:	C:\Program Files\SAI_Demo\ZModels\AppendixC C
Mode:	Run Fitting / All Data Points (1 - 19)
Maximum Iterations:	100
Optimization Iterations:	0
Type of Fitting:	Complex
Type of Weighting:	Calc-Modulus

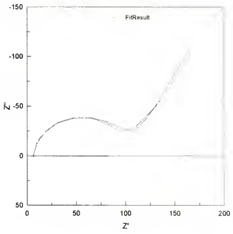

Figure A-11. Fitting of AC Impedance of $LiAl_{0.2}Mn_{1.8}O_{4+\delta}$ thin film grown by UVPLD at 500˚C in the oxygen 500 mtorr.

(12) $LiAl_{0.3}Mn_{1.7}O_{4+\delta}$ grown by UVPLD at 500˚C in the oxygen of 500 mtorr

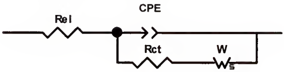

Element	Freedom	Value	Error	Error %
Rel	Free(+)	6.05	0.29769	4.9205
Cct-T	Free(+)	6.7235E-6	1.6637E-6	24.745
Cct-P	Free(+)	0.89982	0.024979	2.776
Rct	Free(+)	102.4	7.3694	7.1967
W-R	Free(+)	339.4	153.08	45.103
W-T	Free(+)	0.41239	0.282	68.382
W-P	Free(+)	0.54494	0.054668	10.032

Chi-Squared:	0.013721
Weighted Sum of Squares:	0.42534

Data File:	~Clipboard
Circuit Model File:	C:\Program Files\SAI_Demo\ZModels\AppendixC C
Mode:	Run Fitting / All Data Points (1 - 19)
Maximum Iterations:	100
Optimization Iterations:	0
Type of Fitting:	Complex
Type of Weighting:	Calc-Modulus

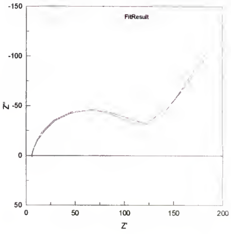

Figure A-12. Fitting of AC Impedance of $LiAl_{0.3}Mn_{1.7}O_{4+\delta}$ thin film grown by UVPLD at 500°C in the oxygen 500 mtorr.

LIST OF REFERENCES

Ahn03 Ahn, H. and Whitten, J. E., *J. Appl. Phys.,* 93, 3384 (2003).

Amm97 Ammundsen, B., Roziere, J., and Islam, M. S., *J. Phys. Chem.*, B101, 8156 (1997).

Ant98 Antonini, A., Bellitto, C., Pasquali, M., and Pistoia, G., *J. Electrochem. Soc.*, 145, 2726 (1998).

Arp88 Arpe, H. J. (eds.), *Ullmann's Encyclopedia of Industrial Chemistry* (5th Edition), John-Wiley & Sons, New York, NY (1988).

Aur91 Aurbach, D. and Gofer, Y., *J. Electrochem. Soc.*, 138, 3529 (1991).

Aur95 Aurbach, D., Zaban, A., Schlectaer, A., Ein-Eli, Y., Zenigard, E., and Markowsky, B., *J. Electrochem. Soc.*, 142, 2873 (1995).

Bar93 Barboux, P., Shokoohi, F. K., and Tarascon, J. M., *U.S Patent,* 1993 5211933.

Bar01 Bard, A. J. and Faulkner, L. R., *Electrochemical Methods; Fundamentals and Applications,* Ch. 8, John Wiley & Sons, New York (2001).

Bat93 Bates, J. B., Gruzalski, G. R., Dudney, N. J., and Hart, F. X., *Solid State Technology*, 36, 59 (1993).

BjÖ02 Björk, H., *Cooperative Lithium-ion Insertion Mechanisms in Cathode Materials for Battery Apllications*, p.12, Fyris-Tryck AB, Uppsala, Sweden (2002).

Bly98 Blyr, A., Sigala, C., Amatucci, G., Guyomard, D., Chabre, Y., and Tarascon, J. M., *J. Electrochem. Soc.*, 145, 194 (1998).

Bre93 Brett, C. M. A. and Brett, A. M. O., *Electrochemistry; Principles, Methods, and Application,* Ch. 11, Oxford University Press, Oxford (1993).

Bro99a Broad, R. J., *Interface*, 8, 3 (1999).

Bro99b Broussely, M., Biensan, P., and Simon, B., *Electrochimica Acta*, 45, 3 (1999).

Bro02 Broadhead, J. and Kuo, H. C., *Handbook of Batteries* (Eds. by Linden, D., and Reddy, T. B.), Ch. 2, McGraw Hill, New York, NY (2002).

Byo93 Boyd, I. W., Craciun, V., and Kazor, A., *Jpn. J. Appl. Phys.,* 32, 6141 (1993).

Che94 Cheung, T. T., *Pulsed Laser Deposition of Thin Films* (Eds. by Chrisey, D. B., and Hubler, G. K.), Ch. 1, John Wiley & Sons, New York, NY (1994).

Chi99 Chitra, S., Kalyani, P., Mohan. T., Gangadharan, R., Yebka, B., Castro-Garcia, S., Massot, M., Julien, C., and Eddrief, M., *J. Electroceramics,* 3:4, 433 (1999).

Cho98 Cho, K. G., Kumar, D., Holloway, P. H., and Singh, R. K., *Appl. Phys. Lett.,* 73 (21), 3058 (1998).

Cho95 Choi, Y. M. and Pyunn, S. I., *Solid State Ionics,* 99, 173 (1995).

Cho99 Cho, J. and Thackeray, M. M., *J. Electrochem. Soc.,* 146, 3577 (1999).

Cho00 Choi, S. and Manthiram, A., *J. Electrochem. Soc.*, 147, 1623 (2000).

Chu01 Chung, H. –T., Myung, S. –T., Cho, T. –H., and Son, J. –T., *J. Power Sources*, 97-98, 454 (2001).

Cra99a Craciun, V., Perriere, J., Bassim, N., Singh, R. K., Craciun, D., and Spear, J., *Appl. Phys. A,* 69, S531 (1999).

Cra99b Craciun, V., Howard, J., Lambers, E. S., Singh, R. K., Craciun, D., and Perriere, J., *Appl. Phys. A,* 69, S535 (1999).

Dea92 Dean, J. A., *Lange's Handbook of Chemistry* (4th Edition), 4.12-4.38, McGraw Hill, New York, NY (1992).

DiC89 Di Castro, V. and Polzonetti, *J. Electron Spectrosc. Relat. Phenom.,* 48, 117 (1989).

Dud99 Dudney, N. J., Bates, J. B., Zhur, R. A., Young, S., Robertson, J. D., Jun, H. P., and Hackney, S. A., *J. Electrochem. Soc.*, 146, 2455 (1999).

Dul96 Duley, W. W., *UV Lasers: Effects and Applications in Materials Science*, p. 407, Cambridge University Press, London (1996).

Dur90 Duraud, J. P., Jollet, F., Thromat, N., Gautier, M., Maire, P., le Gressus, C., and Dartyge, E., *J. Am. Ceram. Soc.,* 73, 2467 (1990).

Ehr02 Ehrlich, G. M., *Handbook of Batteries* (Eds. by Linden, D., and Reddy, T. B.), Ch. 35, McGraw-Hill, New York, NY (2002).

Ell95 Elliott, D. J., *Ultraviolet Laser Technology and Applications,* p. 69, Academic Press, San Diego, CA (1995).

Eri02 Eriksson, T., Gustafsson, T., and Thomas, J. O., *Electrochem. Solid State Letts.*, 5, A35(2002).

Gao96 Gao, Y. and Dahn, J. R., *Solid State Ionics*, 84, 33 (1996).

Goo98 Goodenough, J. B., *Lithium Ion Batteries* (Eds. by Wakihara, M. and Yamamoto, O.), p.1, John-Wiley & Sons, New York, NY (1998).

Goo02 Goodenough, J. B., *Advanced in Lithium-ion Batteries* (Eds. by van Schalkwijk, W. A. and Scrosati, B.), p.144, Kluwer Academic/Plenum Publishers, New York, NY (2002).

Gum94 Gummow, R. J., de Kock, A., and Thackeray, M. M., *Solid State Ionic*, 69, 59 (1994).

Guo96 Guohua, L., Ikuta, H., Uchida, T., and Wakihara, M., *J. Electrochem. Soc.*, 143, 178 (1996).

Guy94 Guyomard, D. and Tarascon, J. M., *Solid State Ionic*, 69, 222 (1994).

Hsu01 Hsu, C. S. and Mansfeld, F., *Corrosion,* 57, 747 (2001).

Hun81 Hunter, J. C., *J. Solid State Chem.,* 39, 142 (1981).

Hwa95 Hwang, K. H., Lee, S. H., and Joo, S. K., *J. Power Sources*, 54, 224 (1995).

Hwa01 Hwang, B. J., Santhanam, R., Liu, D. G., and Tsai, Y. W., *J. Power Sources*, 102, 326 (2001).

Ing96 Ingo, G. M. and Marletta, G., *Nucl. Instrum. Methods B,* 116, 440 (1996).

Jai96 Jaing, Z. and Abraham, K. M., *J. Electrochem. Soc.*, 143, 1591 (1996).

Jan96 Jang, D. H., Shin, Y. J., and Oh, S. M., *J. Electrochem. Soc.*, 143, 2204 (1996).

Jan97 Jang, D. H. and Oh, S. M., *J. Electrochem. Soc.*, 144, 3342 (1997).

Jan00 Jang, S. W., Lee, H. Y., Shi, K. C., Lee, S. M., Lee, J. K., Lee, S. J., Baik, H. K., and Rhee, D. S., *J. Power Sources*, 88, 274 (2000).

Joh97 Johnson, B. J., Doughty, D. H., Voigt, J. A., and Boyle, T. J., *J. Power Sources*, 68, 634 (1997).

Jon99 Jones, S. L., Kumar, D., Cho, K. G., Singh, R. K., and Holloway, P. H., *Displays,* 19, 151 (1999).

Jul00 Julien, C., Haro-Poniatowski, E., Camacho-Lopez, M. A., Escobar-Alarcon, L., and Jimenez-Jarquin, J., *Materials Sci. & Eng.* B72, 36 (2000).

Kan96 Kanoh, H., Feng, Q., Hirotsu, T., and Ooi, K., *J. Electrochem. Soc.*, 143, 2610 (1996).

Kan01 Kang, S. H., Goodenough, J. B., and Rabenberg, L. K., *Electrochem. Solid State Letts.*, 4, 5 (2001).

Kaz92 Kazor, A. and Boyd, I. W., *Appl. Surf. Sci.,* 54, 460 (1992).

Kim03 Kim, K. W., Lee, S. W., Han, K. S., Chung, H. J., and Woo, S. I., *Electrochimica Acta,* 48, 4223 (2003).

Kom02 Komaba, S., Oikawa, K., Myung, S. T., Kumagai, N., and Kamiyama, T., *Solid State Ionics,* 149, 47 (2002).

Koc90 Kock, A. de., Rossouw, M. H., Picciotto, L. A. de., and Thackeray, M. M., *Mat. Res. Bull.*, 25, 657 (1990).

Koe95 Koetschau, I., Richard, M. N., Dahn, J. R., Soupart, J. B., and Rousche, J. C., *J. Electrochem. Soc.*, 142, 9 (1995).

LeC96 Le Cras, F., Bolch, D., Anne, M., and Strobel, P., *Solid State Ionics,* 89, 203 (1996).

Lee98 Lee, D. G., Ph. D. Dissertation, University of Florida, Gainesville, FL (1998).

Lee00 Lee, K. K. and Kim, K. B., *J. Electrochem. Soc.*, 147, 1709 (2000).

Lee01 Lee, Y. S. and Yoshio, M., *Electrochem. Solid State Letts.*, 4, A85 (2001).

Lid95 Lide, D. R., *Handbook of Chemistry and Physics* (76th Edition), Ch. 5, CRC Press, London (1995).

Lin95 Linden, D., (eds.), *Handbook of Batteries and Fuel Cells*, Ch. 1, McGraw Hill, New York, NY (1995).

Lin02 Linden, D., *Handbook of Batteries* (Eds. by Linden, D. and Reddy, T. B.), Ch. 1, McGraw Hill, New York, NY (2002).

Liu96 Liu, W., Kowal, K., and Farrington, G. C., *J. Electrochem. Soc.*, 143, 3590 (1996).

Liu97 Liu, W., Ph. D. Dissertation, University of Pennsylvania, Philadelphia, PA (1997).

Liu99 Liu, P., Zhang, J. G., Turner, J. A., Tracy, C. E., and Benson, D. K., *J. Electrochem. Soc.*, 146, 2001 (1999).

Low96 Lowndes, D. H.,Geohegan, D. B., Puretzky, A. A., Norton, D. P., and Rouleau, C. M., *Science,* 273, 898 (1996).

Low98 Lowndes, D. H., *Experimental Methods in Physics Sciences,* 30, 475 (1998).

Luc99 Lucas, P., Ph. D. Dissertation, Arizona State University, Tempe, AZ (1999).

Mac91 Macklin, W. J., Neat, R. J., and Powell, R.J., *J. Power Sources*, 34, 121 (1991).

Man95 Manev, R., Momchilv, A., Nassalevska, A., and Sato, A., *J. Power Sources*, 54, 323 (1995).

Mas96 Masquelier, C., Tabuchi, M., Ado, K., Kanno, R., Kobayashi, Y., Maki, Y., Nakamura, O., and Goodenough, J. B., *J. Sold State Chemistry*, 123, 255 (1996).

Mat01 Matsuo, M. Kostecki, R., and McLarnon, F., *J. Electrochem. Soc.*, 148, A687 (2001).

Miz80 Mizushima, Jones, K., Wiseman, P. J., P. J., and Goodenough, J. B., *Mat. Res. Bull.*, 15, 783 (1980).

Mor97 Mori, S., Asahina, H., Suzuki, H., Yonei, A., and Yokoto, K., *J. Power Sources*, 68, 59 (1997).

Mor98 Morcrette, M., Barboux, P., Perriere, J., and Brousse. T., *Solid State Ionics*, 112, 249 (1998).

Mor01 Morcrette, M., Barboux, P., Perriere, J., Brousse, T., Traverse, A., and Boilot, J. P., *Solid State Ionics*, 138, 213 (2001).

Mou92 Moulder, J. F., Stickle, W. F., Sobol, P. E., and Bomben, K. D., *Handbook of X-ray Photoelectron Spectroscopy,* (Eds. by Chastain. J. and King, Jr. R. C.) p. 25, Physical Electronics, Inc., Eden Prairie, MN (1992).

Myu00 Myung, S. T., Chung, H. T., Komaba, S., Kumagai, N., and Gu, H. B., *J. Power Sources*, 90, 103 (2000).

Myu01 Myung, S. T., Komaba, S., and Kumagai, N., *J. Electrochem. Soc.*, 148, A482 (2001).

Nag90 Naguara, T. and Tazawa, T., *Progr. Batteries Solar Cells*, 9, 20 (1990).

Nag00 Naghash, A. R. and Lee, J. Y., *J. Power Sources*, 85, 284 (2000).

Nis01 Nishi, Y., *J. Power Sources*, 100, 101 (2001).

Ohz95 Ohzuku, T., Ueda, A., and Kouguchi, M., *J. Electrochem. Soc.*, 142, 4033 (1995).

Oik99 Oikawa, K., Kamiyama, T., Izumi, F., Nakazato, D., Ikuta, H., and Wakihara, M., *J. Solid State Chem.,* 146, 322 (1999).

Par99 Park, Y. S., Lee, S. H., Lee, B. I., and Joo, S. K., *Electrochem. Solid State Letts.*, 2, 58 (1999).

Par00a Park, Y. J., Kim, J. G., Kim, M. K., Kim, H. G., Chung, H. T., and Park, Y., *J. Power Sources*, 87, 69 (2000).

Par00b Park, Y. J., Kim, J. G., Kim, M. K., Chung, H. T., and Kim, H. G., *Solid State Ionics*, 130, 203 (2000).

Pat92 Pathak, A., Mukhopadhyay, D., K., and Pramanik, P., *Mater. Res. Bull.,* 27, 155 (1992)

Pis92 Pistoia, G., Li, L., and Wang, G., *Electrochemica Acta,* 37, 63 (1992).

Pyu97 Pyun, S. I., Choi, Y. M., and Jeng, I. D., *J. Power Sources*, 68, 593 (1997).

Ran48 Randles, J. E. B., *Trans. Faraday Soc.,* 44,327 (1948).

Rob97 Robertson, A. D., Lu, S. H., and Howard, W. F., Jr., *J. Electrochem. Soc.*, 144, 3505 (1997).

Ros90 Rossow, M. H., de Kock, A., de Picciotto, L. A., and Thackeray, M. M., *Mat. Res. Bull.*, 25, 173 (1990).

Rou97 Rougier, A., Striebel, K. A., Wen, S. J., and Cairns, E. J., *J. Electrochem. Soc.*, 145, 2975 (1997).

Sad01 Sand, H. J. S., *Phil. Mag.,* 1, 45 (1901)

Sev48 Sevcik, A., *Coll. Czech. Chem. Comm.,* 13, 349 (1948).

Sha69 Shannon, R. D. and Prewitt, C., *Acta Cryst.,* B25, 925 (1969).

Sho91 Shokoohi, F. K., Tarascon, J. M., and Wilens, J., *Appl. Phys. Lett.*, 59, 1260 (1991).

Sin98 Singh, R. K. and Kumar, D., *Mat. Sci. and Engr. Reports: A review Journal,* 113 (1998).

Sin02 Singh, D., Ph. D. Dissertation, Swiss Federal Institute of Technology, Lausanne, Switzerland (2002).

Sit85 Sitting, M. and Pohanish, R. P., *Handbook of Toxic Chemicals and Carcinogens* (2nd Edition), Noyes Publications, Park Ridge, NY (1985).

Sri99 Srivastava, A., Craciun, V., Howard, J. M., and Singh. R. K., *Appl. Phys. Lett.,* 75 (19), 3002 (1999).

Str96 Striebel, K. A., Deng, C. Z., Wen, S. J., and Cairns, E. J., *J. Electrochem. Soc.*, 143, 1821 (1996).

Sun00 Sun, Y., Jeon, Y., and Lee, H. J., *Electrochem. Solid State Letts.*, 3, 7 (2000).

Tar91a Tarascon, J. M., Wang, E., Shokoohi, F. K., McKinnon, W. R., Colson, S., *J. Electrochem. Soc.*, 138, 2859 (1991).

Tar91b Tarascon, J. M. and Guyomard, D., *J. Electrochem. Soc.*, 138, 2864 (1991).

Tar94 Tarascon, J. M., McKinnon, W. R., Coowar, F., Bowmer, T. N., Amatucci, G., and Guyomard, D., *ibid.,* 141, 1421 (1994).

Tar95 Tarascon, J. M., Coowar, F., Amatucci, G., Shokoohi, F. K., and Guyomard, D., *J. Power Sources*, 54, 103 (1995).

TFB01 Thin Film Batteries at Oak Ridge National Laboratory http://ssd.ornl.gov/Program/BatteryWeb/CrossSection.html (2001).

Tha83 Thackeray, M. M., David, W. I. F., Bruce, P. G., and Goodenough, J. B., *Mat. Res. Bull.*, 18, 461 (1983).

Tha84 Thackeray, M. M., Johnson, P. J., de Piccitto L. A., and Goodenough, J. B., *Mat. Res. Bull.* , 19, 179 (1984).

Tha92 Thackeray, M. M., de Kock, A., Rossouw, M. H., Liles, D.C., Bittihn, R., and Hoge, D., *J. Electrochem Soc.*, 139, 363 (1992).

Tha95 Thackeray, M. M., *J. Electrochem. Soc.*, 142, 2558 (1995).

Tha98 Thackeray, M. M., Shao-Horn, Y., Kahaian, A. J., Kepler, K. D., Skinner, E., Vaughey, J. T., and Hackney, S. A., *Electrochem. Solid State Letts.*, 1,7 (1998).

Tho85 Thomas, M. G. S. R., David, W. I. F., and Goodenough, J. B., *Mat. Res. Bull.*, 20, 1137 (1985).

Woh97 Wohlfahrt-Mehrens, M., Butz, A., Oesten, R., and Huggins, R. A., *Proc. Electrochem. Soc.*, 97-18, 192 (1997).

Wen96 Wen, S. J., Richardson, T. J., Ma, L., Striebel, K. A., Ross, Jr., P. N., and Cairns, E. J., *J. Electrochem. Soc.*, 143, L136 (1996).

Xia95 Xia, Y., Noguchi, H., and Yoshio, M., *J. Solid State Chem.,* 119, 216 (1995).

Xia96a Xia, Y., Zhou, Y., and Yoshio, M., *J. Electrochem. Soc.*, 143, 825 (1996).

Xia96b Xia, Y. and Yoshio, M., *ibid.*, 127, 856 (1996).

Xia96c Xia, Y. and Yoshio, M., *J. Power Sources*, 63, 97 (1996).

Xia97a Xia, Y., Zhou, Y., and Yoshio, M., *J. Electrochem. Soc.*, 144, 2593 (1997).

Xia97b Xia, Y., Zhou, Y., and Yoshio, M., *J. Electrochem. Soc.*, 144, 4186 (1997).

Xia98 Xia, Y., Hideshima, Y., Kumada, N., Nagano, M., and Yoshio, M., *J. Power sources*, 74, 24 (1998).

Xia00 Xia, Y., Kumada, N., and Yoshio, M., *J. Power Sources*, 90, 135 (2000).

Yam95 Yamada, A., Miura, K., Hinokuma, K., and Tanaka, M., *J. Electrochem. Soc.,*142, 2149 (1995).

Zha97a Zhang, Y. C., Tagawa, H., Asakura, S., Mizusaki, J., and Narita, H., *J. Electrochem. Soc.,* 144, 275 (1997).

Zha97b Zhang, Y. C., Tagawa, H., Asakura, S., Mizusaki, J., and Narita, H., *Solid State Ionics,* 100, 4345 (1997).

Zha02 Zhang, S. S., Xu. K, and Jow, T. R. *Electrochem. Solid State Letts.*, 5, A92 (2002).

Zho95 Zhong, Q. and Sachen, U., *J. Power Sources*, 54, 323 (1995).

BIOGRAPHICAL SKETCH

Won-Seok Kim was born in Seoul, Korea, on February 13, 1972. He received a Bachelor of Engineering degree in materials science and engineering at Kang Won National University in February 1996. In January of 1997, he joined the Department of Materials Science and Engineering at the University of Tennessee, Knoxville, and completed his Master of Science in August 1999. Since the fall of 1999, he has been studying for his Ph.D. in the field of materials science and engineering at the University of Florida, Gainesville. His interest is synthesis and characterization of thin films for various applications. He plans to pursue his career in R&D for battery materials after completion of his doctoral degree.

I certify that I have read this study and that in my opinion it conforms to acceptable standards of scholarly presentation and is fully adequate, in scope and quality, as a dissertation for the degree of Doctor of Philosophy.

Rajiv K. Singh, Chairman
Professor of Materials Science and
Engineering

I certify that I have read this study and that in my opinion it conforms to acceptable standards of scholarly presentation and is fully adequate, in scope and quality, as a dissertation for the degree of Doctor of Philosophy.

Cammy R. Abernathy
Professor of Materials Science and
Engineering

I certify that I have read this study and that in my opinion it conforms to acceptable standards of scholarly presentation and is fully adequate, in scope and quality, as a dissertation for the degree of Doctor of Philosophy.

David P. Norton
Professor of Materials Science and
Engineering

I certify that I have read this study and that in my opinion it conforms to acceptable standards of scholarly presentation and is fully adequate, in scope and quality, as a dissertation for the degree of Doctor of Philosophy.

Stephen J. Pearton
Professor of Materials Science and
Engineering

I certify that I have read this study and that in my opinion it conforms to acceptable standards of scholarly presentation and is fully adequate, in scope and quality, as a dissertation for the degree of Doctor of Philosophy.

Dinesh O. Shah

Dinesh O. Shah
Professor of Chemical Engineering

This dissertation was submitted to the Graduate Faculty of the College of Engineering and to the Graduate School and was accepted as partial fulfillment of the requirements for the degree of Doctor of Philosophy.

August 2004

Pramod Khargonekar

Pramod P. Khargonekar
Dean, College of Engineering

Kenneth J. Gerhardt
Interim Dean, Graduate School